Développement de cellules solaires à base de films minces CZTSSe

Giovanni Altamura

UNIVERSITÉ DE GRENOBLE

THÈSE

Pour obtenir le grade de

DOCTEUR DE L'UNIVERSITÉ DE GRENOBLE

Spécialité : **Physique des matériaux**

Présentée par

Giovanni ALTAMURA

Thèse dirigée par **Henri MARIETTE** et
codirigée par **Louis GRENET** et **Simon PERRAUD**

préparée au sein du **CEA INAC, Equipe Nanophysique et Semiconducteurs (NPSC)**
dans **l'École Doctorale de Physique, UJF**

Développement de cellules solaires à base de films minces $Cu_2ZnSn(S,Se)_4$

Thèse soutenue publiquement le **2 Septembre 2014**
devant le jury composé de :

M. Daniel BELLET
Professeur à Grenoble-INP, présidente du jury
M. Daniel LINCOT
Professeur à Chimie-ParisTech, rapporteur
M. Jean-Yves CHANE-CHING
Chercheur à l'université Paul Sabatier Toulouse, rapporteur
M. Louis GRENET
Ingénieur de Recherche au CEA Liten, encadrant
M. Simon PERRAUD
Ingénieur de Recherche au CEA Liten, co-encadrant
M. Henri MARIETTE
Professeur à l'Université Joseph Fourier, directeur de thèse

Université Joseph Fourier / Université Pierre Mendès France /
Université Stendhal / Université de Savoie / Grenoble INP

A mamma, papà,

Tony, Maurizio

e Annarita

“**Tänka fritt är stort, men**

Tänka rätt är större”

Thomas Thorild (1759-1808)

“To think freely is great, to think correctly is greater”

Acknowledgements

First, I would like to thank all members of the examining committee of this PhD thesis.
Thank you to Daniel Lincot and Jean-Yves Chane-Ching for agreeing to evaluate my work.
Thank you to Daniel Bellet for agreeing to serve as president of the panel.

I still remember when in July 2011, sitting at my desk in my old office in Paris, I decided to move to Grenoble and start my PhD at CEA: now I can say that it has been the best decision I have ever made in my entire life! For that I would like to thank faithfully three persons: my thesis director Henri Mariette, and my two co-supervisors Louis Grenet and Simon Perraud. Thank you Henri for being a real teacher for me, I learned from you that most of the times things (in Physics) are not like they could appear: that there are more and more explanations and viewpoints to address the conclusions of an experiment, and that going deeply in the understanding of what I am doing is always the best solution. Thank you Louis for being by my side every time I needed: it has been very important for me to have the possibility to count on you and have your support in the development of my ideas. You taught me how to start and how to conclude an experiment, how to write a scientific paper, how to prepare an oral presentation, how to evaluate things around me the way they are evolving. Thank you Simon for being for me the main example of: scrupulousness, accuracy and organization in a workgroup and especially in my daily work. I etched in my head your phrase: *"Giovanni, il faut que tu sois en peu plus rigoureux!"* I promise you I will always be. You three will always be my mentors and source of inspiration!

Thank you to Emmanuelle Rouvière for welcoming me into the great family of LITEN, et for giving me the chance to express myself in this environment.
A big thank you to the photovoltaic team at LITEN: you have been part of my daily work and it has been a pleasure to spend these three years with all of you. Thank you Fred for receiving me in your Barnave domain, for sharing with me your knowledge, enthusiasm and…of course beers. Thank you Nico to teach me how to watch one step ahead, and that a patent is always around the corner when an idea pops out of the head. Thank to David, Charles and Raphael: I do not know if the right way to thank all of you does really exist! You have been the best glue between the "daily work in the office" and the "nightly work outside the office", I hope that our friendship will last forever and I wish you guys all the best in your future! Thank you Mathieu and Jérôme to be part of these three years even when you left the office, you taught me a lot on the French street language and costumes. Thank you Hélène and Cécile for giving the feminine touch to the environment, and for everything we have shared together. Thank you Pascale and Fabrice for being always open

to discussions and confrontation on different themes of my work. Thank you Seb, Christine, Sévak, Pauline, Dario, Chloé, Karol and Jesus for being active part at the right moment of this experience, it is also because of you that my PhD has come to an end.

I would like also to address a big thank you to MY team at INAC: in particular the continuous exchange with you of ideas and prospective has been fundamental for the success of my PhD project. A big thank to Hervé Boukari and Yoann Cure for the discussions and debates on kesterite technology. Thank you Joël Bleuse for the passion demonstrated me about optics and to how important it is in my project. Thank you to Catherine Bougerol for helping me whenever I needed you during the thesis. Thank you to Régis André for being a colleague always open and curious about my work. Thank you to Sirona Valdueza-Felip, Luca Radaelli, Anna Markhatova, Lionel Gérard, Gilles Nogues, Yann Genuist, Didier Boilot and Bruno Daudin for let me be part of your project and at the same time be part of mine. A big thank to all the other PhD students at NPSC, I wish all the best for you as well.

A big thank you is for Sergio Bernardi and Patrick Chapon for the relationship we have created in these three years: I am sure about the fact that our collaboration will not stop now.

I cannot forget all my friends that although outside my PhD environment, they are, without a doubt, the best I could even imagine. Thank you for all you have done in these three years fellas! Thank you Riccardo for everything we shared together: I should write other 150 pages to explain the weight of your influence in these years. Thank you to my "sunshine friends": Chiara, Giada, Vera, Johnny, Marco, Clio, Carlo, Lorenzo, Eric, Caroline, Simeon, Ramona, Lia, Stefano. The moments we spent together are etched in my heart and are something that even the time cannot erase! Thank you Alice for being such a joy and delight: I promise not to stop being such a good godfather. Another big thank you is directed towards my dear friends back in Italy (Vita, Angelo, Vito, Francesco Z, Aura, Danilo, Giuseppe, Francesco D, Piero, Laura, Nunzio, Gianluca and all the others) for always supporting me although we meet twice per year since nine years now. You are my oldest friends and I will always love you.

Thank you to my Parents and my Siblings for being the universe in which my world exists. You always say that we are not perfect but the love you show me everyday overtakes the perfection!

Thank you to all those I have forgotten...I sincerely beg you to forgive me.

Résumé

L'objectif principal de cette thèse consiste à déterminer (et expliquer) les relations entre les conditions de synthèse des couches minces de $Cu_2ZnSn(Se,S)_4$ (CZTSSe), leurs propriétés physiques et les performances des dispositifs photovoltaïques. Le mécanisme de formation du matériau est étudié en fonction des conditions de croissance. Le CZTSSe est synthétisé par un procédé en deux étapes, où une première étape de dépôt des précurseurs sous vide est suivie d'une seconde étape de recuit sous atmosphère de sélénium. Différents ordres d'empilement des précurseurs sont étudiés afin de comprendre la séquence de réactions qui, à partir de leur dépôt, conduit à la couche finale de CZTSSe. Le résultat de cette étude montre que le matériau final obtenu après un recuit à haute température (570°C) et de longue durée (30 min) est indépendant de l'ordre de dépôt des précurseurs, mais que les étapes intermédiaires de formation du matériau sont fortement influencées par les positions respectives des couches de cuivre et d'étain.

Les possibles implications bénéfiques de l'incorporation de sodium dans le CZTSSe sont également étudiées. Ce travail est réalisé en synthétisant la couche de CZTSSe sur différents substrats contenant diffèrents taux de sodium: de cette manière, pendant la synthèse, le sodium migre du substrat vers l'absorbeur. Après quantification du Na dans le CZTSSe juste après la croissance, le matériau est caractérisé afin d'évaluer sa qualité. Ensuite il est employé dans une cellule solaire complète pour vérifier ses propriétés photovoltaïques. Les résultats montrent que, comme dans le cas de la technologie CIGS, le sodium est bénéfique pour le CZTSSe, permettant l'augmentation de la tension à circuit ouvert et le rendement des cellules.

Le molybdène est le contact arrière le plus utilisé pour les cellules solaires à base de CZTSSe. Cependant, il a été suggéré récemment que le Mo n'est pas stable à l'interface avec le CZTSSe. En outre, aucune étude expérimentale n'a été effectuée à ce jour pour tester si les cellules solaires construites sur un autre contact arrière pourraient présenter de meilleures propriétés photovoltaïques. Ainsi, divers métaux (Au, W, Pd, Pt et Ni) sont déposés sur le Mo et testés comme contacts arrières dans les cellules solaires à base de CZTSSe. Il est démontré qu'il est possible de synthétiser des couches minces de CZTSSe de qualité quand le tungstène, l'or et le platine sont employé comme contacts arrière. Il est observé que les contacts en W et Au permettent d'augmenter le courant photogénéré, mais aussi que le Mo reste le meilleur contact arrière du point de vue du rendement de conversion photovoltaïque.

Les effets de la variation du rapport [S]/([S]+[Se]) sur les performances des cellules solaires à base de CZTSSe sont étudiés. Cette étude est effectuée par simulations des cellules solaires à base de CZTSSe, avec un ratio variable des éléments chalcogènes dans

l’absorbeur, en ayant pour objectif la détermination de la composition optimale de l’absorbeur. Les simulations conduisent à un rendement de 16,5% (avec une tension en circuit ouvert de 0,56 V, courant de court-circuit de 37,0 mA/cm^2 et un facteur de forme de 79,0%) lorsque la teneur en soufre est diminué linéairement à partir du contact arrière en direction de la couche tampon. Sur la base de ces résultats, nous proposons que l'ingénierie de bande interdite avec une variation du taux [S]/([S]+[Se]) dans l'absorbeur soit un moyen efficace qui permet d'augmenter les performances des cellules solaires à base CZTSSe sans nécessiter de changer la qualité même de l'absorbeur.

Scientific Production

Journal Papers

- G. Altamura, C. Roger, L. Grenet, J. Bleuse, H. Fournier, S. Perraud and H. Mariette, *"Influence of sodium-containing substrates on Kesterite CZTSSe thin films based solar cells"*, **MRS Proceedings / Volume 1538 / 2013.**
- S. Valdueza-Felip, A. Mukhtarova, Q. Pan, G. Altamura, L. Grenet, C. Durand, C. Bougerol, D. Peyrade, F. González-Posada, J. Eymery, E. Monroy, *"Photovoltaic Response of InGaN/GaN Multiple-Quantum Well Solar Cells"*, **Jpn. J. Appl. Phys. 52 (2013) 08JH05.**
- G. Altamura, L. Grenet C. Bougerol, E. Robin, D. Kohen, H. Fournier, A. Brioude, S. Perraud and H. Mariette, *"Cu2ZnSn(S1-xSex)4 Thin Films for Photovoltaic Applications: Influence of the Precursor Stacking Order on the Selenization Process"*, **Journal of Alloys and Compounds 588 (2014), 310-315**
- G. Altamura, L. Grenet, C. Roger, F. Roux, V. Reita, R. Fillon, H. Fournier, S. Perraud and H. Mariette, *"Alternative back contacts in kesterite Cu2ZnSn(S1-xSex)4 thin film solar cells"*, **J. Renewable Sustainable Energy 6 , 011401 (2014)**
- G. Altamura, L. Grenet, R. Fillon, S. Perraud and H. Mariette, *"Influence of [S]/([S]+[Se]) ratio in kesterite Cu2ZnSn(S,Se)4 solar cells: a numerical simulation approach"*, **manuscript in preparation.**
- L. Grenet, R. Fillon, G. Altamura, H.Fournier, F. Emieux, P Faucherand, S. Perraud, "*Analysis of photovoltaic properties of Cu2ZnSn(S,Se)4-based solar cells"*, **Solar Energy Materials & Solar Cells 126 (2014), 135-142.**
- C. Roger, G. Altamura, F. Emieux, O. Sicardy, F. Roux, R. Fillon, P. Faucherand, N. Karst, H. Fournier, L. Grenet, F. Ducroquet, A. Brioude, S. Perraud, *"Sodium-doped Mo Back Contacts for Cu(In,Ga)Se2 solar cells on Metallic Substrates : Growth, Morphology and Sodium Diffusion"*, **J. Renewable Sustainable Energy 6, 011405 (2014)**

Conferences

- **27th European Photovoltaic Solar Energy Conference and Exhibition** (September 24-28, Frankfurt / Germany), poster presentation.
- **E-MRS 2013 SPRING MEETING** (May 27-31, Strasbourg / France), oral presentation.
- **ICMAT 2013 Material for Advanced Technologies** (30 June - 5 July, Singapore), oral presentation.
- **PVTC 2013 conference** (May 22 - 24, Aix-en-Provence / France), oral presentation.

- **39th IEEE Photovoltaic Specialists Conference** (June 16-21, Tampa / USA), poster presentation.
- **2013 MRS Spring Meeting & Exhibit** (April 1-5, San Francisco / USA), poster presentation.
- **Nanotechnology for Next Generation High Efficiency Photovoltaics Spring International School** (April 1-6, Cargèse / France), poster presentation.
- **SPIE Photonics West** (February 1-7, San Francisco / USA), oral presentation.

Patents

- **E.N.:12 57749**, Authors: L.GRENET, G. ALTAMURA, S. PERRAUD
- **E.N.:13 54696**, Authors: G. ALTAMURA, L.GRENET, S. PERRAUD, F. ROUX
- **E.N.:13 57660**, Authors: L.GRENET, G.ALTAMURA, R. FILLON, S. PERRAUD

Awards and Fellowships

- Best poster award at *PVTC 2013 Conference*, 22-24 May, Aix-en-Provence, France
- Invited Lecture at *IUPAC NMS-IX 2013 Conference*, 17-22 October, Shanghai, China

Table of contents

List of figures

Symbols & Acronyms

Definition	Abbreviation
Thin Film	TF
Photovoltaics	PV
Crystalline Silicon	c-Si
Amorphous Silicon	a-Si
$CuIn_xGa_{1-x}Se_2$	CIGS
$Cu_2ZnSn(S_xSe_{1-x})_4$	CZTSSe
Cu_2ZnSnS_4	CZTS
$Cu_2ZnSnSe_4$	CZTSe
European Photovoltaic Industry Association	EPIA
Air Mass	AM
Valence Band	VB
Conduction Band	CB
Photon Energy	E_{ph}
Bandgap Energy	E_g
Donor concentration	N_D
Acceptor concentration	N_A
Boltzmann constant	k
Temperature	T
Electron concentration	n
Hole concentration	p
Compensation ratio	Δ
Intrinsic carrier concentration	n_i
Space charge region	SCR
Electric field	$\vec{E}$
Current density	J
Applied voltage	V

Dark saturation current	I_0
Ideality factor	n
Dielectric permittivity	ε_0
Saturation velocity	v_s
Time	t
Generation rate	G_n
Recombination rate	R_n
Carrier diffusion length	L
Carrier lifetime	τ
Physical vapor deposition	PVD
Soda lime glass	SLG
Back contact	BC
Chemical bath deposition	CBD
Transparent conductive oxide	TCO
Cadmium Sulphide	CdS
Zinc Oxide	ZnO
Aluminum doped Zinc Oxide	Al:ZnO
Scanning Electron Microscopy	SEM
Energy Dispersive X-ray Spectroscopy	EDS/EDX
X-Ray Diffraction	XRD
Full Width at Half Maximum	FWHM
Glow Discharge Spectroscopy	GDS
Photoluminescence	PL
Current-voltage measurements	I-V
Open circuit voltage	*Voc*
Short circuit current	*Jsc*
Fill Factor	*FF*
Power Conversion Efficiency	*PCE*
Series resistance	*Rs*
Shunt resistance	*Rsh*
External Quantum Efficiency	EQE
Grazing-incidence X-ray diffraction	GIXRD

Borosilicate glass	BS
EAGLE2000 glass	VSS
Secondary Ion Mass Spectrometry	SIMS
Capacitance-voltage measurements	C-V
Transmission electron microscopy	TEM
Charge carrier density	N
Vacuum permittivity	ε
Relative material permittivity	ε_0
Space charge region width	w
Diffusion voltage	V_D
Photogenerated current	J_{ph}
Surface recombination velocity	SRV
Electron effective mass	m_e^*
Hole effective mass	m_h^*
Electron band mobility	μ_e
Hole band mobility	μ_h
Electron affinity	x_e
Effective density of states in conduction band	N_c
Effective density of states in valence band	N_v
Trap density	N_{def}
Capture cross-section	σ
Minority carrier lifetime	τ
Thermal velocity of electrons	v_{th}
Defect distribution	W_G
Chalcogens ratio at the CZTSSe|CdS interface	s
Chalcogens ratio at the Mo|CZTSSe interface	t
Reference current density	J_{oo}
Back surface bandgap	BSG
Surface bandgap gradient	FSG

Chapter 1

Introduction

Outline

1.1 Aim of this study

Due to the decrease of system installation costs and increasing industry experience, photovoltaics (PV) will become an increasingly economically advantageous source of electricity. Around 200 GW in 2020 and 2 TW in 2050 of cumulated PV capacity is predicted to be installed globally [1]. These volumes will have a major impact on PV technologies in terms of resources and production.

Thin-film PV (TFPV) technology has more than 10% of this volume share, expecting to increase in the next ten years [1]. Despite the good results of TFPV and the increasing confidence in this technology, some drawbacks concerning the materials employed are highlighted. Some of the materials investigated are either expensive or toxic: arsenic, cadmium, gallium, germanium, indium, and tellurium. An evaluation of the literature does not picture a clear framework on this subject [2-3]. Nevertheless, despite the differences in the conclusion, the common thought is that a potential risk to TFPV development is due to the scarcity of some elements.

$Cu_2ZnSn(S_xSe_{1-x})_4$ (CZTSSe) material is a promising candidate for low-cost and high-efficiency thin film solar cells. Compared to other technologies CZTSSe offers the advantage of containing no critical chemical elements. This key aspect joined to its optical properties makes possible to foresee a photovoltaic thin film technology scalable at several GW/year [4].

Many groups have focused on elaborating such materials in the past few years, using vacuum [5-6] or non-vacuum techniques [7-8], either one [6] or two-step process [5-8]. The best performances for CZTSSe-based solar cells are obtained at IBM Watson (USA) with a power conversion efficiency of 12.6%. [9]

The research of a trade-off between high performances and low processing cost CZTSSe has recently driven the attention of the scientific community. In order to become very interesting for production at industrial level, CZTSSe solar cell performances must be certainly improved. In this manuscript, different ways to improve CZTSSe solar cells are investigated. The aim of this work is firstly to better understand the CZTSSe thin film synthesis mechanism in a two-step selenization process, and secondly to study the influence of different parameters, as the bandgap of the absorber and the back contact, on the photovoltaic performances of the CZTSSe solar cell.

In the following, a brief description of the structure of this thesis and the main contents is given.

Chapter 2 illustrates the state-of-the-art of CZTSSe thin film technology. Starting from describing the physics of solar cells, an outlook on the different thin film technologies is taken, followed by a detailed description of CZTSSe solar cell background.

Chapter 3 describes the experimental work carried out to fabricate CZTSSe absorbers and the various techniques useful to characterize the material from a physical, morphological, optical and electrical point of view.

In Chapter 4 a study of CZTSSe formation mechanism is reported.

Chapter 5 deals with the influence of sodium in CZTSSe solar cells.

Chapter 6 reports experimentally the effects of different back contacts on the performances of CZTSSe solar cells.

In Chapter 7 the effects of [S]/([S]+[Se]) ratio tuning on CZTSSe based solar cell performances have been studied by solar cell capacitance simulator (SCAPS) to find out the optimum absorber composition.

This work is completed with a summary and a brief outlook for the further improvement of solar cell performance.

1.2 References

[1] A. Jäger-Waldau, Publication Office of the European Union, ISSN: 1018-5593

[2] A. Feltrin, A. Freundlich, Renewable Energy, 33 (2008), pp. 180-185

[3] V.M. Fthenakis, Renewable and Sustainable Energy Reviews, 8 (2004), pp. 303-334

[4] H. Katagiri, K. Jimbo, S. Yamada, T. Kamimura, W.S. Maw, T. Fukano, T. Ito,T. Motohiro, Solar cell without environmental pollution by using CZTS thin films, Proceedings of Photovoltaic Energy Conversion Conference Vol. 3 (2003).

[5] L. Grenet, S. Bernardi, D. Kohen, C. Lepoittevin, S. Noel, N. Karst, A. Brioude, S. Perraud, H. Mariette, Solar Energy Materials and Solar Cells 101 (2012) 11-14.

[6] I. Repins, C. Beall, N. Vora, C. De Hart, D. Kuciauskas, P. Dippo, B. To, J. Mann, W. C. Hsu, A. Goodrich, R. Noufi, Solar Energy Materials and Solar Cells 101 (2012) 154-159.

[7] K. Wang, O. Gunawan, T. Todorov, B. Shin, S. J. Chey, N. A. Bojarczuk, D. Mitzi, S. Guha, Applied Physics Letters, 97 (2010), 143508.

[8] T. Todorov, O. Gunawan, S.J. Chey, T.G. De Monsabert, A. Prabhakar, D.B. Mitzi, Thin Solid Films 519 (2011) 7378-7381.

[9] W. Wang, M. T. Winkler, O. Gunawan, T. Gokmen, T. K. Todorov, Y. Zhu, D. B. Mitzi, Adv. Mater., doi: 10.1002/aenm.201301465

Chapter 2

State-of-the-art

Outline

2.1 Physics of Photovoltaics

2.1.1 The photovoltaic effect

The origin of the word *"photovoltaic"* is made up from the Greek word *phos* (light), and *voltaic* (electrical) from the name of Italian physicist Alessandro Volta. The physical basis for photovoltaics is the *"photovoltaic effect"*. An appropriate definition of the photovoltaic effect is the direct conversion of light into electricity.

The term *"solar cell"* is employed to describe a device, which is able to convert the energy of the sun (light) into electrical energy.

The first observation of the photovoltaic effect (1839) is attributed to the French physicist Edmond Becquerel. He discovered that exposing to light two copper plates immersed in a solution, it is possible to produce a continuous flow of current. After that, an American engineer called Charles Fritts produced the first selenium-based solar cell (1883). However, the efficiency of Fritts's cell was less than 1% which was not enough to justify it as a practical power source due to the cost of gold contacts.

1954 was the beginning of silicon technology for PV. It was discovered at Bell Labs that a silicon p-n junction could convert 6% of the incoming sunlight into electrical energy. In 1958, silicon solar panels were included on the American spacecraft Vanguard I. Hoffmann Electronics increased the efficiency to 14% and soon a market niche for silicon solar cells was discovered (1960). In the following 50 years, the global PV production has reached over 140 MW. The 21th century sees above all the ripeness of the thin film, dye-synthesized, and multijunction solar technology [1].

2.1.2 Current trends in PV technology

Renewable energy as photovoltaics is one of the alternatives to the *"conventional"* energy as nuclear, hydro, and coal. Nuclear has the 15% in world production of electricity. France, Japan, and USA depend on nuclear power plants (75%, 30%, and 19% respectively) in their whole energy resources [2-3]. A lot of countries, like Germany and Japan, are gradually switching to renewable energy as photovoltaics in order to reduce risk factor of nuclear energy. Total energy capacity of the world is 4742 GW in which the share of the solar energy was 37 GW in 2010 (0.78%) [3]. In 2009, the new installation of solar energy was

7.1 GW that was more than doubled in 2010 (17.5 GW). The top 10 companies such as Q-cells, Sharp, Suntech, Keyocera, First Solar, Motech, Solar World, Jasolar, Yingli, and Sanyo share the almost totality of the market.

It is possible to design PV power plants of several hundred MW for different applications. Some examples are shown in Figure 1.

Since its emergence thin film photovoltaics (TFPV) take on two difficult challenges: (i) to compete with silicon based PV in terms of power conversion efficiency and manufacturing costs, (ii) to contain only earth-abundant and non-toxic materials without severe degradation in the long term. Moreover as long as crystalline silicon (c-Si) solar PV manufacturing costs decreases, TFPV solar cells will remain in the small minority. In recent years, TFPV technology has experienced rapid growth and achieved significant technological advances, consolidating its place in the solar market. In 2012, TFPV represented approximately 10% of the global PV market (28.4 GW) [4].

From a physical point of view, the advantages of TF solar cells are to have a direct band gap, a high absorption coefficient which allow absorbing the majority of the solar spectrum using only few microns of materials, and reduced sensitivity to recombination at grain boundaries. Moreover, from a technological point of view, they either permit to decrease fabrication costs by exploiting manufacturing actions like roll-to-roll, or permit the usage of flexible substrates, and monolithic interconnections.

In thin film solar cells family, chalcogenide-based solar cells as $Cu(In,Ga)Se_2$, CdTe and $Cu_2ZnSn(S,Se)_4$ are the best candidates potentially reduce manufacturing cost of solar energy. Recently, First Solar Company proclaimed that the current cost of electricity by its CdTe solar panel is 0.70 $/W and aims to develop solar cells at the cost of 0.5 $/W [4].

Figure 1: Examples of solar cell applications: (a) building integration, (b) space, (c) plants, (d) nomad

2.1.3 Solar radiation

Solar radiation is comparable to the one of a black body at 5800 °K [5]. Sunlight passes through the atmosphere, but scattering and absorption processes attenuate it. Solar irradiance spectrum occurs over a wide range of energies (or wavelengths).

The Air Mass (AM) is the path length which light takes through the atmosphere, and is useful to quantify the reduction in the power of light when it is absorbed by the atmosphere. The Air Mass is defined as:

$$AM = \frac{1}{\cos(\theta)} \qquad \text{(eq. 1)}$$

where θ is the angle from the vertical (zenith angle). When the sun is directly perpendicular to Earth surface, AM is 1. The standard spectrum at the Earth's surface is called AM1.5G, (the G stands for *global*): the AM1.5G spectrum (θ = 48.2°) has been normalized to give 1 kW/m^2. This spectrum is the normalized flux used to measure the performance of cells in laboratories. The standard spectrum outside the Earth's atmosphere is called AM0, because

the light does not overcome the atmosphere barrier. This spectrum is typically used to predict the expected performance of cells in space. Both AM0 and AM1.5G spectra are compared in Figure 2.

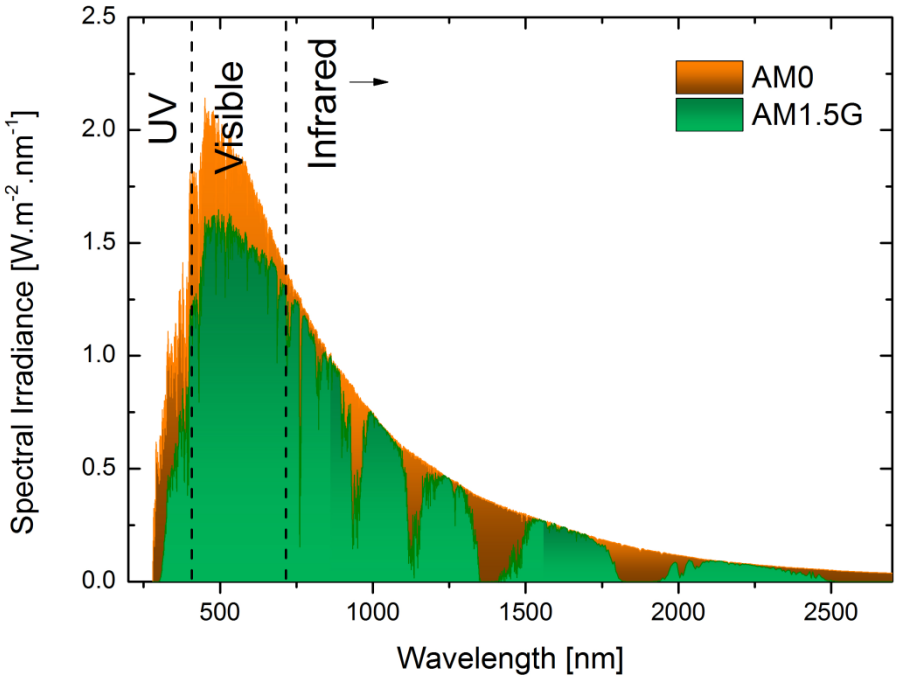

Figure 2: Solar irradiance spectrum above atmosphere and at Earth surface.

2.1.4 Principle

Photovoltaics allow generating electrical power by converting solar radiation. Physics of photovoltaics is based on the optical and electrical properties of semiconductors. When a photon (hv) with energy higher than the bandgap of the semiconductor is absorbed, an electron-hole pair is created. This means that an electron is promoted from the valence band (E_v) to the conduction band (E_c) leaving a hole behind. This pair needs to be separated then by electric field in order to avoid recombination: this field is provided by a p-n junction (see 2.1.5) which is the core of a photovoltaic device. A photon hitting on the surface of a semiconductor could be either reflected from the surface, absorbed in the material or transmitted throughout the material itself. In the case of PV devices, photons which are not absorbed (thus reflected or transmitted) are typically considered as a loss since they do not

generate power. Considering the energy of the photon and the bandgap of the semiconductor it is possible to establish if a photon is absorbed or transmitted:

- $E_{ph} < E_G$: photons with energy E_{ph} less than the band gap E_G are transmitted
- $E_{ph} = E_G$: photons with energy E_{ph} equal than the band gap are absorbed and can create an electron hole pair.
- $E_{ph} > E_G$: photons with energy higher than the band gap are also absorbed. However, for PV applications, part of the energy of these photons is released since electrons quickly thermalize down to the E_c lower energy states.

2.1.5 Physics of p-n junction

In a doped semiconductor the more plentiful carriers are named *"majority carriers"*, while the less abundant carriers are named *"minority carriers"*. Majority carriers are electrons (holes) in n-type semiconductors (p-type semiconductors). Minority carriers are electrons (holes) in p-type semiconductors (n-type semiconductors). At equilibrium, the product of the majority and minority carrier concentration is a constant:

$$n_i^2 = n_0 p_0 \qquad \text{(eq. 2)}$$

where n_i is the intrinsic carrier concentration, n_0 and p_0 are the electron and hole equilibrium carrier concentrations.

When an n-type and a p-type semiconductor are put in contact, a p-n junction is formed between the two materials. This event is the same in the case of homo-junctions or hetero-junctions. Once the two semiconductors are in contact, electrons from the n-region near the junction interface diffuse in the p-region leaving donor atoms electrically unshielded by the majority carriers. In the same way, holes from the p-region near the interface diffuse in the n-region, leaving acceptors unshielded behind. This phenomenon is called *"diffusion"*. The region nearby the p–n interface, common at the two semiconductors, which lost its neutrality and become actively charged, is called the *"space charge region"* (SCR). The rest of the two semiconductors which is not influenced by the metallurgical junction is called *"quasi-neutral region"* (QNR). The consequence of the formation of the SCR is an

electric field ($\vec{E}$) which fights the diffusion for both electrons and holes. $\vec{E}$ will superimpose on the random movement of carriers accelerating holes in the same direction of the field and electron in the opposite. This phenomenon is called *"drift"*. When an equilibrium condition is reached, a potential difference (V_D) is formed across the p-n junction. A schematic of the p-n junction is shown in figure 3.

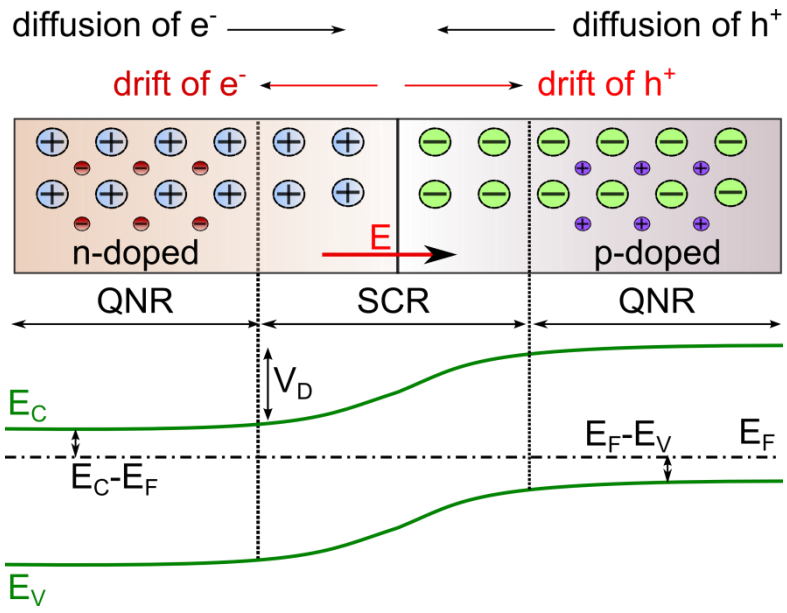

Figure 3: p–n junction in thermal equilibrium with zero-bias voltage applied. Donor atoms (blue particles), acceptor atoms (green particles), electrons (red particles), holes (violet particles).

2.1.6 Current-voltage characteristics of a diode

The metallurgical junction introduced in the previous paragraph is the starting point to build a diode. In fact, the diode is a p-n junction connected to two contacts.

It is possible to describe the diode current-voltage (I-V) characteristics (Figure 4), though the following equation:

$$I(V) = I_0\left(e^{\frac{qV}{nkT}} - 1\right) \qquad \text{(eq. 3)}$$

where I is the net current flowing through the diode, I_0 is the dark saturation current, V is the applied voltage across the diode, n is the diode ideality factor, k is the Boltzmann constant, and T is the temperature.

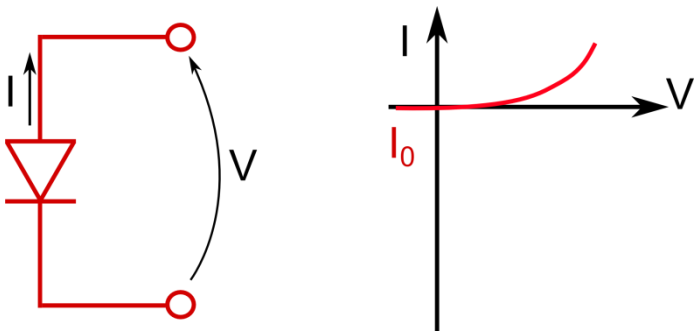

Figure 4: Static I-V characteristics of a diode

I_0 is defined as:

$$I_0 = I_{00}\left(e^{\frac{-E_A}{nkT}} - 1\right) \qquad \text{(eq. 4)}$$

I_0 is the diode saturation current which is activated by the activation energy E_A and is the diode leakage current in the absence of light. E_A is the energy of the dominant recombination mechanism. I_{00} is called "*reference current*" which is only weakly temperature dependent. The n moderates the voltage dependence of the current density [6].

2.1.7 Ideality factor

The ideality factor (n) is typically measured from the slope of the dark I-V characteristics. In ideal solar cell, the ideality factor is as much as possible close to one. Different magnitudes of n indicate that a specific recombination mechanism is dominant. Thus the variation of the ideality factor allows evaluating the type of recombination in solar cells.

2.1.8 Light I-V characteristics

When a solar cell is illuminated under solar spectrum, additional electron-hole pairs are created giving rise to the so-called photogenerated current (I_{ph}) which could be model as a current generator in parallel to the diode (Figure 5). I_{ph} which is given by the product of the carrier generation function *G(z)* and the collection probability $\eta_c(z,V)$:

$$I_{ph}(V) = -qA \int G(z)\eta_c(z,V)dz \qquad \text{(eq. 5)}$$

where q is the elemental charge, and A is the surface of the solar cell. The "collection probability" (ηc) is defined as the probability that a carrier generated by the absorption of a photon in a certain region of the p-n junction is collected. Collection probability is max in the SCR as the electric field effectively separates the electron-hole pairs. In QNR, diffusion is the dominant mechanism. In these areas only carriers generated at a distance from the SCR which is less than the minority carrier diffusion length (Ln,p) can be collected. Ln,p is the average distance a carrier can travel from the point where it is created until it recombines.

Generally, one of the two components of the junction (n or p) is used as a light absorber material in single solar cell. For this reason photovoltaic cells are designed with an absorber layer much thicker than the other layer forming the junction [6].

I_{ph} has the effect of shifting down the I-V characteristics into the fourth quadrant (Figure 5). When a cell is light irradiated, equation 3 (diode law) needs to be modified by adding the photogenerated current, so the output current becomes:

$$I(V) = I_0\left(e^{\frac{qV}{nkT}} - 1\right) - I_{ph}(V) \qquad \text{(eq. 6)}$$

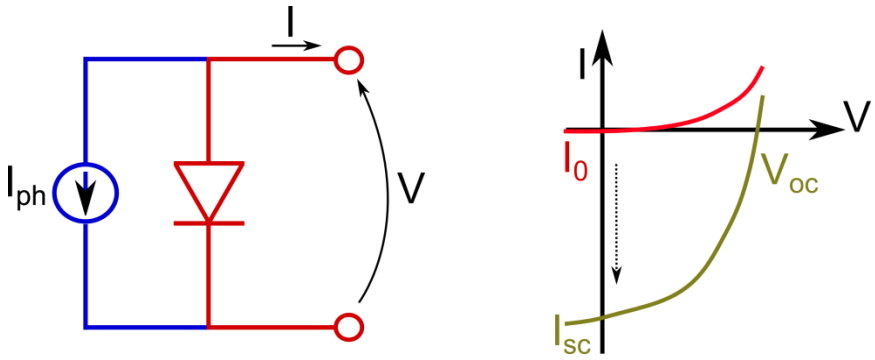

Figure 5: Model and I-V curve of a solar cell under illumination.

2.1.8.1 Short-circuit current

The I_{sc} term in Fig. 5 is named *"short-circuit current"* defined as the current through the solar cell when the terminals are in short circuit (the voltage across the solar cell is zero). It is one of the figures of merit of a solar cell. By definition, I_{sc} is identical to $I_{ph}(0)$. The typical factors influencing I_{sc} are the light intensity, the optical properties of the cell, the thickness of the p-n junction, and the collection probability [6].

2.1.8.2 Open-circuit voltage

Another figure of merit of solar cell is the so-called *"open-circuit voltage"* (V_{oc}): which is the voltage at the output of the cell when no load is connected. In this case the output current is zero ($I=0$), so the V_{oc} can be calculated from equation 6 as:

$$V_{oc} = \frac{nkT}{q} \ln\left(\frac{I_{ph}(V_{oc})}{I_0} + 1\right) \qquad \text{(eq. 7)}$$

From equation 4, V_{oc} can be reformulated as:

$$V_{oc} = \frac{E_A}{q} - \frac{nkT}{q} \ln \frac{I_{00}}{I_{ph}(V_{oc})} \qquad \text{(eq. 8)}$$

Equation 8 shows that V_{oc} depends on both I_{00} and I_{ph}. The variations of I_0 depend on recombination inside the solar cell, thus V_{oc} variations also depend on the amount of recombination in the solar cell.

2.1.8.3 Fill Factor

The fill factor (*FF*) is the third figure of merit introduced in this chapter. It is defined as the ratio between the square drawn by the values of the current (I_{MP}) and voltage (V_{MP}) of the cell resulting in its maximum power point ($P_{MP}=V_{MP}\times I_{MP}$), and the square given by the product $V_{oc}\times I_{sc}$ (Figure 6):

$$FF = \frac{V_{MP}\times I_{MP}}{V_{oc}\times I_{sc}} \qquad \text{(eq. 9)}$$

An ideal solar cell has a *FF* as closer as possible to one. In fact *FF* increases along with V_{MP} and I_{MP} approaching respectively V_{oc} and I_{sc}. To do that, it is mandatory to decrease the losses due to parasitic resistances inside the solar cell (parasitic resistance will be detailed further in the manuscript). Using this concept, it is possible to expose the *FF* as a measure of the losses of a solar cell.

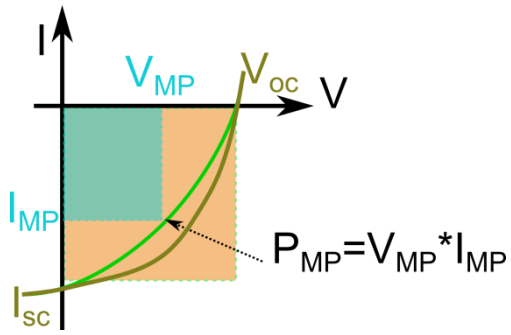

Figure 6: Graph of the FF of the solar cell: the green square is derived from the maximum power point (Vmp, Imp), the yellow square is identified by (V_{oc}, I_{sc})

2.1.8.4 Power Conversion Efficiency

The power conversion efficiency (*PCE*) is the most important figure of merit, which allows comparing solar cells each other. It is defined as the ratio between the generated electrical power (P_{MP}) and the solar energy (P_{IN}) to which the cell is exposed:

$$PCE = \frac{P_{MP}}{P_{IN}} = \frac{V_{oc} \times I_{sc} \times FF}{P_{IN}} \qquad \text{(eq. 9)}$$

PCE depends on different parameters such as the intensity of the incident sunlight, the type of solar spectrum, the working temperature of the solar cell. For this reasons it is important, in order to compare the I-V characteristics of two or more devices, to carefully control the conditions under which *PCE* is measured. Typical measurement setup for terrestrial solar cells is with an AM1.5G spectrum (defined in 2.1.3) at a temperature of 25°C.

2.1.9 Losses in solar cells

Equation 6 is considered for an ideal solar cell since it does not take into account series (R_s) and shunt resistances (R_{sh}) with are present into real solar cells. By incorporating these resistances in the model of Fig. 5 (see Figure 7), what we obtain is equation 10:

$$I(V) = I_0 \left(e^{\frac{q(V - IR_S)}{nkT}} - 1 \right) - I_{ph}(V) - \frac{V - IR_S}{R_{sh}} \qquad \text{(eq. 10)}$$

The effects of these parasitic resistances are, *in primis*, to decrease the *FF* of the cells.

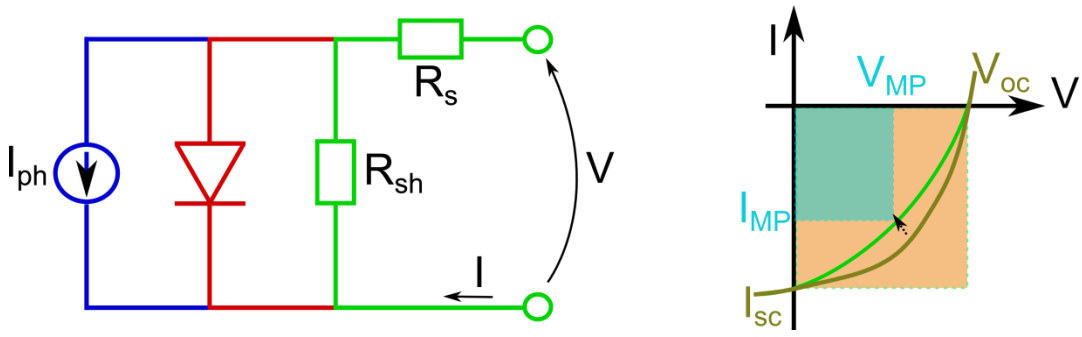

Figure 7: Solar cell model including parasitic resistances.

2.1.9.1 Series Resistance

R_s variation is mainly affected by the resistances of the front and back contacts, and the resistance at the interface of the different layers [6]. High values of R_s may reduce the I_{sc}, contrary to V_{oc} where it has no effect (see Figure 8).

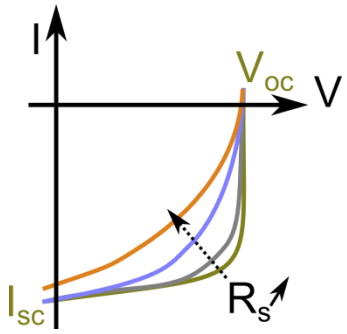

Figure 8: Influence of R_s on photovoltaic characteristics under illumination.

2.1.9.2 Shunt Resistance

R_{sh} is a model of alternative paths (in particular short-circuits) for current. Its variations could be due to a non-perfect interface between the doped regions and the metal contacts, and to recombination in Shockley-Read-Hall (SRH) defects into the QNR. Contrary to R_s, R_{sh} must be as highest as possible in order to prevent lost in V_{oc} (see Figure 9).

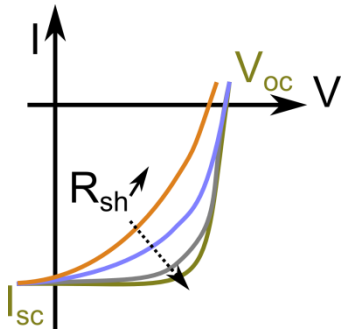

Figure 9: Influence of R_{sh} on photovoltaic characteristics under illumination.

2.2 Solar cell

A solar cell is an opto-electronic device which, by photoelectric effect, directly converts sunlight into electricity. Its aim is to generate electric power. The core of a solar cell is the semiconductor p-n junction (see 2.1.5): once the sunlight is absorbed, an electron-hole pair is created and separated by the junction producing a current flow and a voltage across the contacts. Metal contacts at the edges of the p-n junction allow power dissipation when a load is directly connected (Figure 10).

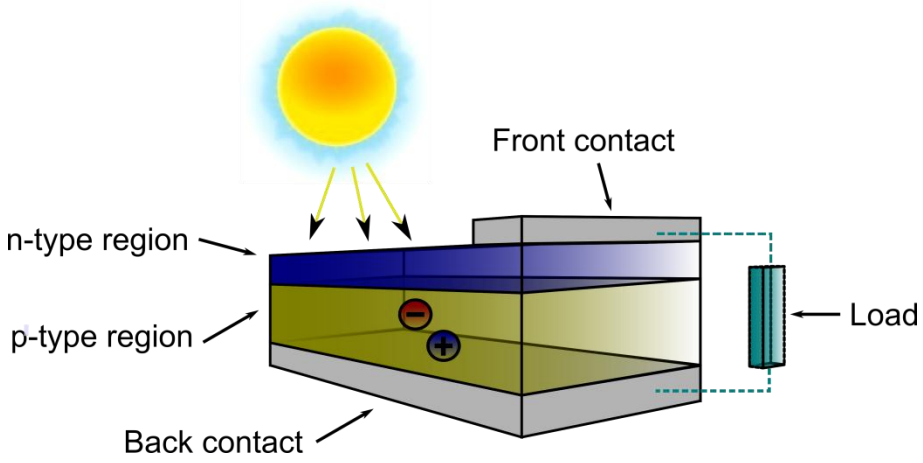

Figure 10: Example of solar cell

2.3 Thin Film Solar cells

2.3.1 Device structure

Two types of configurations called *"substrate"* and *"superstrate"* are possible for thin film solar cell technology (Figure 11). The advantage of using the first configuration is that any type of substrate, transparent or opaque, can be employed since the light is passing through the cell before hitting on the substrate. Relating to this, is the fact that the choice of any substrate, allows using flexible foils (e.g. polymers, stainless steel) for role-to-role manufacturing. In the case of superstrate configuration, the light is hitting on the substrate before being absorbed by the solar cell. The choice of the substrate is imposed by the technology: it must be transparent (e.g. glass) in order to permit the light to be absorbed in the solar cell junction.

The choice of one configuration over the other depends on the type of technology used to build the solar cell.

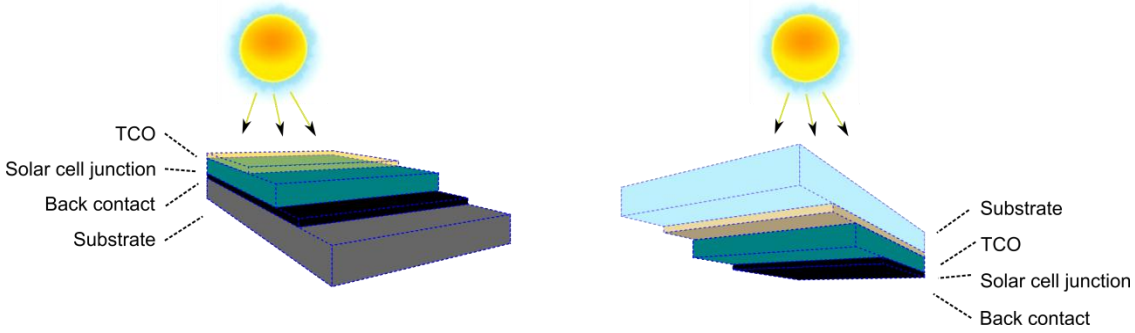

Figure 11: Two possible configurations for thin film solar cells: substrate (left side) and superstrate (right side).

2.3.2 Possible materials

2.3.2.1 Amorphous Silicon (a-Si)

A-Si material became interesting for solar cell applications when the possibility to decrease its defects by hydrogenation was discovered (a-Si:H) [7]. The advantage of a-Si:H are the low cost Si employed, low temperature process. Typical superstrate p-i-n configuration is used [7], although substrate configuration is also employed [8]. In p-i-n structure, the intrinsic layer is of good quality and plays the role of absorber of photons. Record efficiency of 10.1% obtained at Oerlikon Solar Lab [9] with a simple junction, whereas 13.4% is achieved with a a-Si:H/µc-Si:H/µc-Si:H triple-junction [10].

2.3.2.2 Cadmium Tellurate (CdTe)

As for a-Si:H, typical CdTe solar cells are developed in the superstrate configuration: starting from a transparent glass and followed by the successive deposition of TCO, CdS buffer (n-type layer), CdTe absorber (p-type), back contact [7]. CdTe has a number of advantages as its band gap of 1.45 eV and its high absorption coefficient [11] giving a word record of 20.4% power conversion efficiency established by First Solar [11].

2.3.2.3 Cu(In,Ga)Se_2 (CIGS)

CIGS is the thin film technology which nowadays offers the higher efficiency at laboratory level [11]. CIGS has some advantages as its tunable bandgap ranging from pure CIS (1.0 eV) to pure CGS (1.7 eV), high α (10^5 cm^{-1}) [12], and a technology which is mature since more than 20 years. The best result (20.8% by Zentrum fuer Sonnenenergie- und Wasserstoff-Forschung in Germany) has been reached with a CIGS absorber co-evaporated on Mo-coated glass, further incorporated in a heterojunction with CdS, and completed with a ZnO window layer [12].

2.4 $Cu_2ZnSn(S,Se)_4$ Solar cells

2.4.1 Introduction

From a technical point of view, today's commercially available thin film modules suffer from low efficiency like a-Si, shortage of raw material like Te in the case of CdTe, and In in the case of CIGS technology, or materials toxicity like Cd in CdTe technology. In this context, $Cu_2ZnSn(S_xSe_{1-x})_4$ (CZTSSe) appears to be a very attractive and highly potential material applied as a chalcogenide absorber in TF solar cells, regarding the fact that it is made from non-toxic (in the case of a pure sulfur-based compound, with no selenium), earth-abundant and low-cost raw materials, and shows high-efficiency potential for the near future [13].

2.4.2 Material properties

In the last ten years, numerous investigation at theoretical level, have been carried out in order to predict the formation mechanism and the physical properties of CZTSSe compounds. The formation of I_2–II–IV–VI_4 compounds like CZTSSe can be achieved from an II–VI semiconductor by sequential replacement of cations in which the octet rule is respected and the total charge remains neutral (see Figure 12).

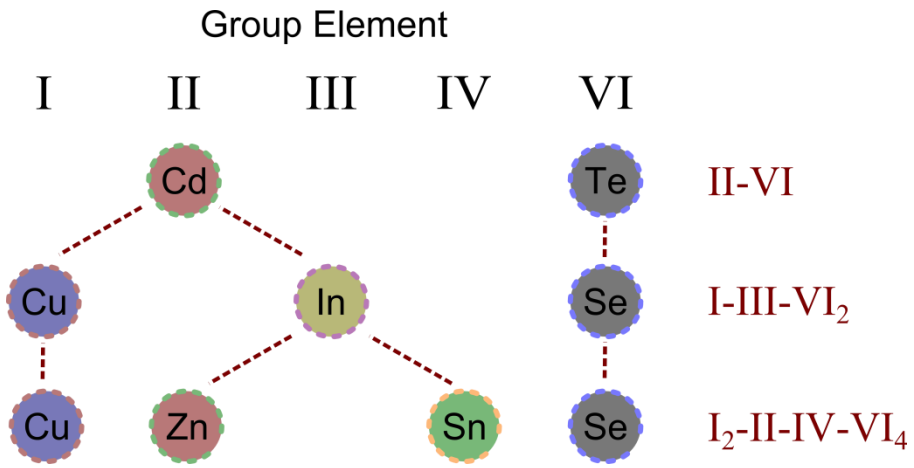

Figure 12: Formation of stoichiometric I_2–II–IV–VI_4 compounds can be achieved by a sequential replacement of cations.

2.4.2.1 CZTSSe crystal structure

Binary compounds like CdTe adopt the cubic zincblende structure in which there are two interpenetrating face-centered cubic crystals [14]. The ternary I–III–VI_2 semiconductor alloys like CIS (in this case a chalcopyrite structure) can be built by replacing the group II atom with two atoms of group I and III [12-15]. Always respecting the octet rule, it is possible to split the ternary I–III–VI_2 compound by replacing two atoms of group III with two atoms respectively from group II and IV, forming a I_2–II–IV–VI_4 semiconductors.

Composition of quaternary compounds in a phase diagram can be rather complex to display. Since each element can in principle be varied independently of the others, we have to be very careful when using terms such as ‘Cu-poor’, ‘Zn-rich’ etc., which are commonly employed to describe CZTSSe films. These terms are intelligible when only one component varies, but when two or more components deviate from stoichiometry, the terminology can be misleading.

The fact that the chalcogens (S, Se) are not an independent variables, allows representing the alloy in a ternary phase diagram. In fact the amount of anions (chalcogens) introduced in the alloy depends on the amount of the cations and their valency: Cu(I), Sn(IV) and Zn(II). In the CZTSSe literature, the ratios of atomic percentages [Cu]/([Zn]+[Sn]) and [Zn]/[Sn] are often used to represent the composition of the cations in the alloy. Both ratios

are equal to one when the material is stoichiometric. However, these ratios are not independent, and therefore do not clearly show the deviations from stoichiometry in a particular case. A ternary phase diagram is the most useful way to summarize compositions in the Cu-Zn-Sn system. An example of a ternary phase diagram is shown in Figure 10.

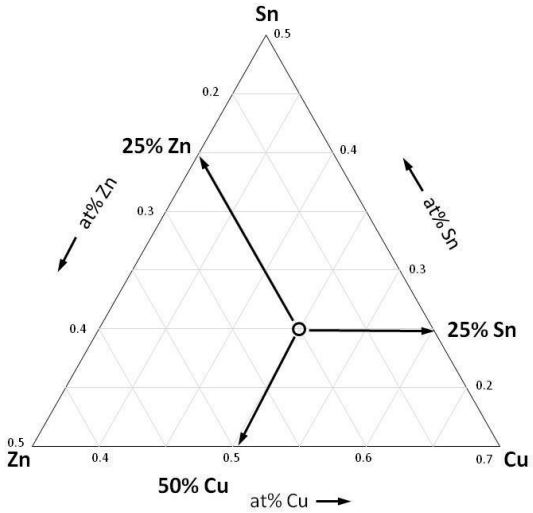

Figure 13: Ternary composition diagram showing the position of stoichiometric CZTSSe [19].

The three sides of the plot each show the atomic percentage of one of the three metal elements. At any point in the diagram, the three values read off the axes will sum to unity. The circle in Figure 13 corresponds to the stoichiometric composition of CZTSSe compound.

A comprehensive analysis of the Cu_2X-ZnX-SnX_2 pseudo-ternary system (where X could be S or Se) was carried out by Olekseyuk *et al* [19], who presented a phase diagram for the system at 400°C (Figure 14). Cu_2ZnSnX_4 as a single phase is present only within a rather narrow range of compositions, which is indicated with an asterisk at the centre of the plot. In all other regions of the phase diagram there are up to two additional secondary phases present, always alongside CZTSSe.

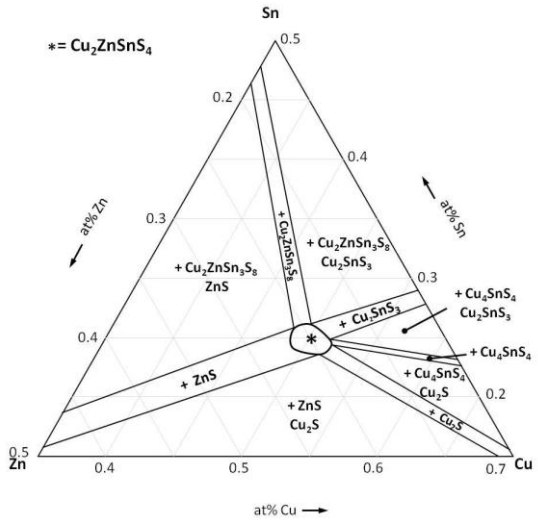

Figure 14: Ternary phase diagram adapted from reference [19], showing the expected secondary phases at 400°C.

Taking the case of pure CZTS represented in Figure 11, there are five two-phase fields, in which one secondary phase will be observed in addition to CZTS. In between these there are five three-phase fields, where the secondary phase from both of the bordering regions will be formed alongside CZTS. Other phases not in this diagram but seen during the formation of CZTS in other reports include Cu_4SnS_6 and SnS_2.

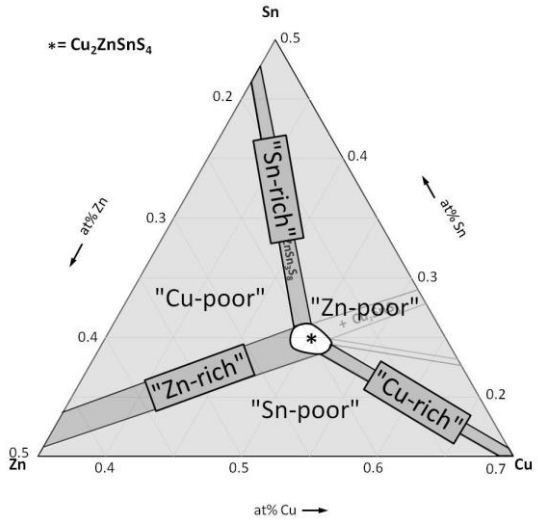

Figure 15: Ternary phase diagram defining the compositional labels used throughout this text.

Aside from the small region of single-phase material, we can usefully define six regions, shown in Figure 15, as “Cu-poor”, “Cu-rich”, “Sn-poor” etc. These are the labels which will be applied to compositions in this report, and by this definition they tell us which secondary phases should be expected to form at that composition (see Table 1).

Composition description	Expected secondary phases
“Cu-poor”	$Cu_2ZnSn_3X_8$ + ZnX
“Sn-rich”	$Cu_2ZnSn_3X_8$
“Zn-poor”	Cu-Sn-S + $Cu_2ZnSn_3X_8$ / Cu2X
“Cu-rich”	Cu_2X
“Sn-poor”	Cu_2X, ZnX
“Zn-rich”	ZnX

Table 1: Definition of composition descriptions used in this report, in terms of the expected secondary phases.

One property of CZTSSe material is the possible shift from its stoichiometric composition leading in particular to Cu-poor compounds. The latter phenomenon originates from the inclination of the hosting crystal to stabilize copper vacancies, in which the charge balance is commonly insured by appropriate substitutions on the cationic sites.

CZTSSe crystallizes in a structure which could be kesterite (space group $I\bar{4}$) [16-18], stannite (space group $I\bar{4}\bar{2}m$) [17]. The stannite structure differs from that of the kesterite by the stacking sequence of the cations layers along the c-axis, i.e. (…–[ZnSn]–[Cu_2]–[ZnSn]–[Cu_2]–…) for stannite versus (…–[CuSn]–[CuZn]–[CuSn]–[CuZn]–…) for kesterite. In the case of kesterite, it is also possible to have a so called *“disordered kesterite”* (space group $I\bar{4}\bar{2}m$, as stannite) in which a random on-site distribution of Cu and Zn (50/50) occurs in the Cu/Zn layer leading to a higher symmetry [20]. Lafond *et al.* report that disordered-kesterite and kesterite models are still open to debate since they are very similar (Figure 14) and almost undistinguishable [21]. The only differences lye in the splitting for symmetry reasons of the 4d position into 2c and 2d positions (Wyckoff notation) going from the $I\bar{4}\bar{2}m$ space group to the $I\bar{4}$space group, and a slight change in the position chalcogens anions.

It is recurring to have kesterite and stannite structure in the material at the same time due to a low energy difference (~3 meV per atom) in which the cations (Cu, Zn, Sn) are fixed, and

the anions (S, Se) are randomly distributed [16-17]. This energy difference could undergo also a bandgap variation of the material of 0.15 eV between kesterite (lower value) and stannite (higher value) [17]. Details about the different crystal structures are shown in Figure 16. Since the kesterite phase is the more likely to have (more stable) for CZTSSe material, only this one will be taken as reference in the rest of the manuscript (Figure 17).

Lafond *et al.* and his group at Nantes University demonstrated: *(i)* a deviation in composition between the surface and the bulk for non-stoichiometric Cu-poor and Cu-rich CZTS using EDX and X-ray photoelectron spectroscopy [22], (ii) the ability of the CZTS phase to tolerate substitutions, i.e. deviations of the Cu_2ZnSnS_4 stoichiometric composition, without collapse of the structure and maintaining the overall charge balance in a proved Cu-deficiency range ([Cu]/[Zn+Sn]) between 0.79–1.14 [22]. Starting from the latter assumption, it is more adequate to reformulate the $Cu_2ZnSn(S_xSe_{1-x})_4$ in $Cu_{2-y-z}Zn_ySn_z(S_{1-x}Se_x)_4$.

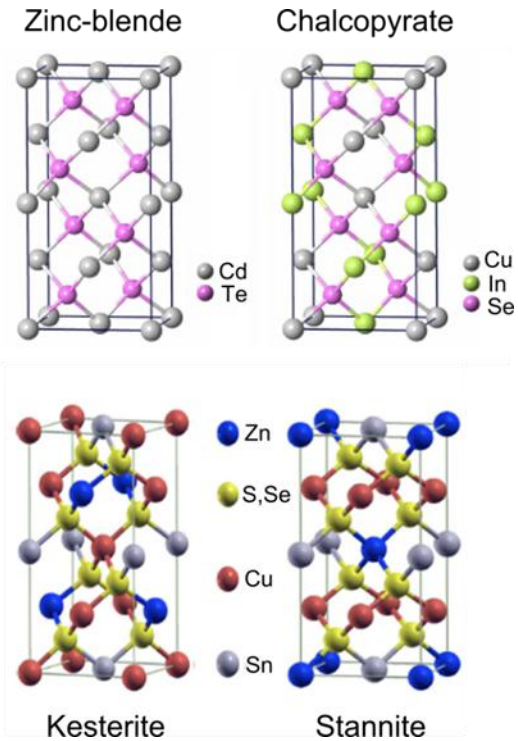

Figure 16: Crystal structure representation of binary, ternary and quaternary compounds.

From an experimental point of view, structural characterization is made principally on CZTSSe monograins. They are synthesized from high-purity powders of CuZnSn-alloy and elemental chalcogens in molten potassium iodide in evacuated quartz ampoules and annealed isothermally at high temperature (around 1000°K) for days (around 4). After the synthesis the flux material was removed by deionised water [23].

Schorr from Free University Berlin confirms by a neutron and X-ray diffraction study [24] that the CZTSSe crystal structure and the cation disorder are in agreement with first-principles calculations. Scragg *et al.* show that it is possible to determine the critical temperature (260 °C) for the transition from ordered to disordered kesterite. The latter is performed by tracking Cu/Zn disorder in CZTSSe with near-resonant Raman spectroscopy [25]. Zillner *et al.* studied the lattice positions of Sn in CZTS nanoparticles and thin films studied by synchrotron X-ray absorption near edge structure (XANES) analysis [26].

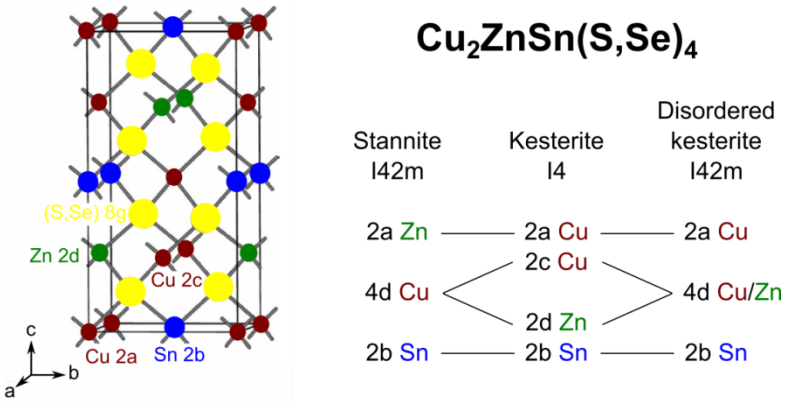

Figure 17: Relationship between the crystallographic positions of cations in stannite, kesterite, and disordered-kesterite structures.

2.4.2.2 CZTSSe bandgap

The chalcogens concentration into CZTSSe alloys gives the possibility to make band engineering to tailor the material properties for a given application, but at the same time, allows having some alloy disorder.

Calculations of the electronic band alignment of $Cu_2ZnSn(S_xSe_{1-x})_4$ alloys by density functional theory (DFT) reveal a direct bandgap monotonically increasing from 1.0 eV

(pure CZTSe) to 1.5 eV (pure CZTS) [16-18] with a small bowing parameter (*b~0.1*) as reported in equation 11.

$$E_G(x) = (1-x)E_G(CZTSe) + xE_G(CZTS) - bx(1-x) \qquad \text{(eq. 11)}$$

Since *b* is small, it is possible to approximate as linear the E_G variations as a function of *x*.

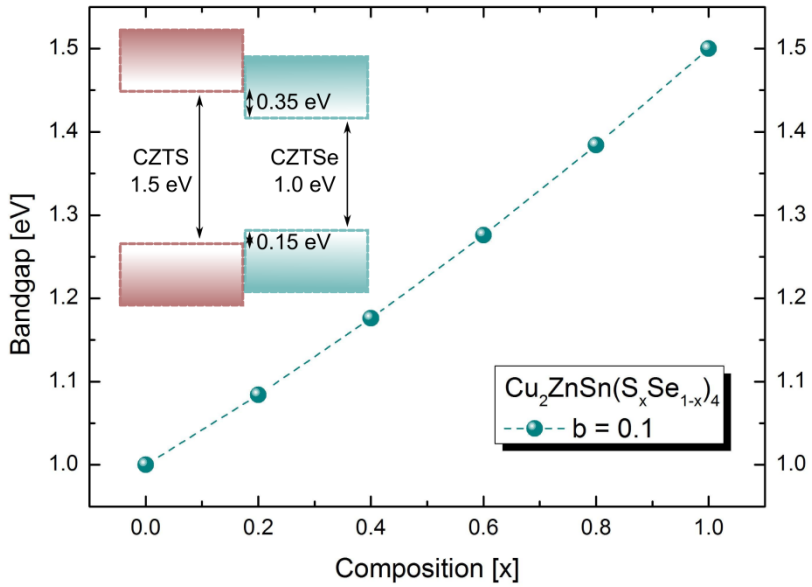

Figure 18: $Cu_2ZnSn(S_xSe_{1-x})_4$ bandgap variation as function of the composition (x). In the inset the Type I band alignment between CZTS and CZTSe

In Figure 18 is noticeable as the band alignment between CZTS and CZTSe is of type I [18, 23], in particular the E_c offset (CBO~0.35 eV) is larger than the E_v offset (VBO~0.15 eV) [18]. This confirms the x variation has more important effects on the E_c rather than E_v.
Direct measurements of the variation of the CZTSSe bandgap between 1.0 and 1.5 eV are performed with different techniques: (i) optical absorption spectra of the CZTSSe powders using UV–vis–NIR spectrometer [27], (ii) electrolyte electroreflectance measurements at room temperature [28]. Both confirm a nearly linear variation of the bandgap along with the variation of chalcogens ratio, with a bowing parameter between 0.08 [27] and 0.19 [28].

2.4.2.3 CZTSSe defects and doping

Due to higher number of constituent atoms compared to binary or ternary compounds, CZTSSe has a wider range of possible defects depending on its growth conditions and variations from stoichiometry [18, 30-32]. Most of them are antisites, vacancies, or interstitials: they can be located shallow or deep in the bandgap, and their concentration depends on their own formation energy [17, 30, 32]. In particular, shallow level defects can influence the minority and majority carrier concentrations thus the conductivity, whereas deep level defects may act as recombination centers for photogenerated electron-hole pairs [6].

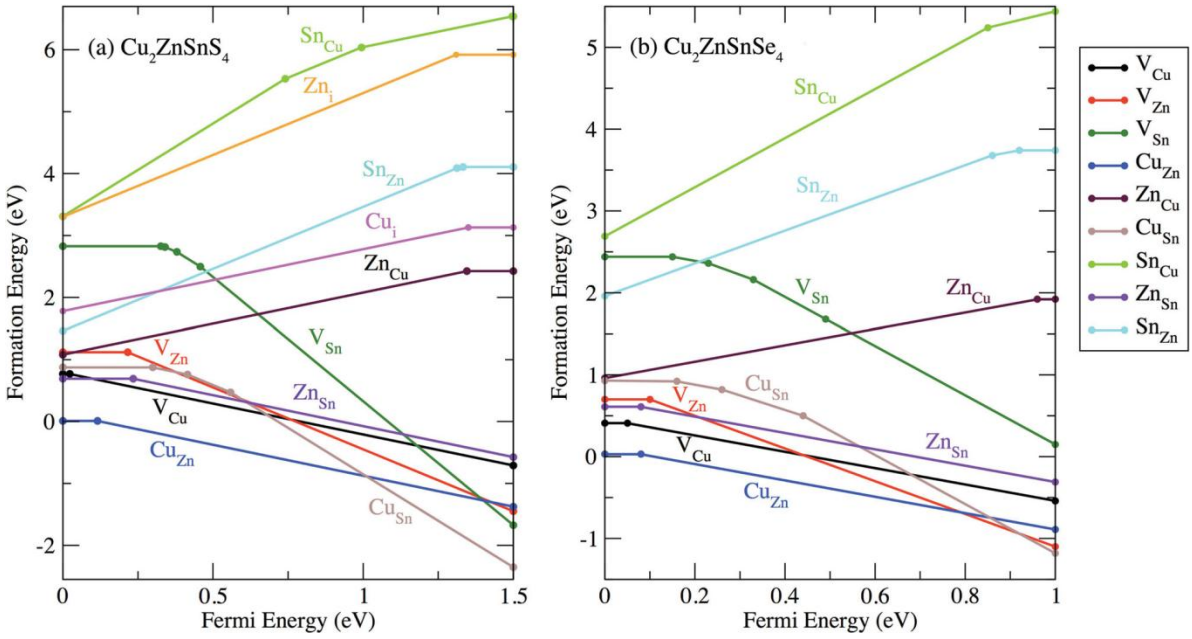

Figure 19: Calculated defect formation energy as a function of the Fermi energy for a Cu-poor and Zn-rich CZTSSe, taken from Ref 14.

The most familiar defects, with their formation energies as function of the position within the bandgap, for pure CZTS and CZTSe are summarized in Figure 19. The two graphs in Figure 19 could explain why the p-type conductivity of CZTSSe is mainly due to the antisite Cu_{Zn}: its formation energy is lower than all the others acceptors defects (V_{Cu}, V_{Zn}, Zn_{Sn}, Cu_{Sn}) although they can be present in the alloy [30-32]. From this analysis it is possible to explain the reason of the higher efficiency for Cu-poor and Zn-rich CZTSSe

solar cells [33-34]: indeed this composition allows the increase of shallow Cu vacancies in spite of Cu_{Zn} antisite. Moreover, the high formation energy of donor defects (Sn_{Cu}, Sn_{Zn}, Zn_{cu}, Cu_i, Zn_i), explains why n-type doping of CZTSSe is very difficult.

The more CZTSSe is non-stoichiometric the more deep levels caused by the intrinsic defects increase [16, 30, 34]: some of them may act as traps for free carriers, which reduces the efficiency of solar-cell devices [15-18, 30-32]. Chen *et al.* presume that charge-compensated defect complexes are easy to form in CZTSSe. They may passivate the deep donor levels improving CZTSSe quality and thus solar cell efficiency [30]. In particular the formation of the $[V_{Cu}^{-} + Zn_{Cu}^{+}]^0$ cluster under Zn-rich and Cu-poor conditions is predicted to be beneficial for CZTSSe solar cell performance; however, the precipitation of a ZnS phase must be avoided [15-18, 30].

2.4.2.4 CZTSSe phase formation: parasitic minor phases

Compare to ternary chalcopyrite compound like CIGS, it is more difficult to achieve a single phase material for quaternary compounds like CZTSSe. Various studies with Raman spectroscopy and X-ray diffraction show that it is very difficult to achieve a homogenous CZTSSe material without spurious minor phases [35-36]. Depending on the Cu, Zn, Sn concentration, and the growth technique employed the type and quantity of minor phases into CZTSSe compounds can vary [36-38].

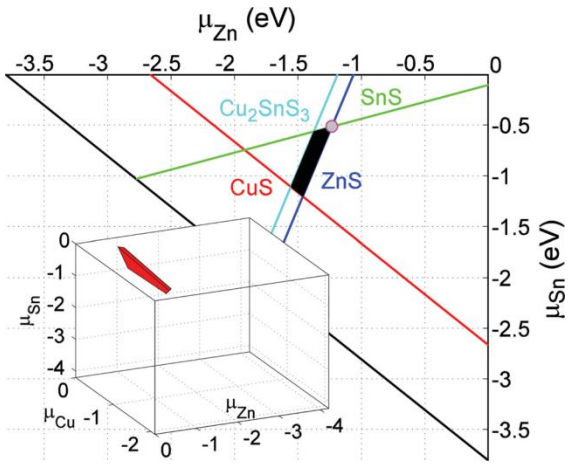

Figure 20: The calculated chemical-potential stability diagram of pure CZTS, taken from Ref 11.

Various studies on this subject have been reported in literature using different calculation methods: the common point is that, single phase CZTS and CZTSe exist only in a very small region of the phase diagram [26, 30-32]. Figure 20 shows, in the case of pure CZTS, a slice (in black) in a given Cu-rich plane, for which the CZTS is stable: outside this area there will be the simultaneous existence of CZTS with one of the other phases like ZnS, CuS, SnS, Cu_2SnS_3 (CTS) [25, 39-40]; this is valid also for pure selenite ZnSe, CuSe, SnSe, Cu_2SnSe_3 (CTSe) [36, 41-42].

Since the best performing CZTSSe solar cells are made with an absorber which is Zn-rich, the control over the Zn-content in CZTSSe alloys is very important: Zn-poor samples lead to CT(S,Se) formation, instead Zn-rich samples lead to Zn(S,Se) [41-42], which is congruent with the narrow line in the Zn-region of figure 20.

2.4.2.5 CZTSSe absorption coefficient

CZTSSe material owns an optical absorption coefficient higher than 10^4 cm^{-1} at wavelengths lower than the band gap measured by absorption spectroscopy [43]. This permits to absorb light with an absorber of very thin thickness (1-2 μm).

2.4.3 Technological $Cu_2ZnSn(S,Se)_4$ synthesis

Different techniques, vacuum or non-vacuum, are employed to synthesize CZTSSe absorber.

2.4.3.1 Vacuum techniques

One-step vacuum processes consist in simultaneously incorporating all the elements. Among these techniques employed for high-quality CZTSSe deposition, co-sputtering [44] and co-evaporation [45] can give good PV performances. Other interesting methods can be pulsed-laser deposition [46]. The so-called two-step process is a technique where the precursors are first incorporated during an ambient temperature process like sputtering or evaporation, followed by an annealing step [47-52]. The chalcogens can be incorporated

into the precursor [36-37] or during the annealing step [35, 40, 48-50]. The annealing step could be a selenization [36-37] or sulphurization process [39-40].

2.4.3.2 Non-vacuum techniques

Non-vacuum deposition methods for CZTSSe synthesis, as well as for other applications, are scalable and low-cost processes with the goal of being attractive for large scale manufacturing. The world record efficiency for CZTSSe solar cell (12.6 %) has been achieved following one of these approaches: the simultaneous use of spin-coating solution and particles of constituents [33]. Other possible methods giving a quite good PV performance CZTSSe could be nanoparticles [53] and electroplating [54]. One weak point of these techniques is, in some cases, the use of toxic and dangerously instable solvents which are hard of recycling as hydrazine.

2.4.4 History of CZTSSe solar cells

The first reported CZTSSe solar cell device was in 1997 by Katagiri *et al.* [55]. They built the first pure CZTS solar cell (0.66% *PCE*) where CZTS absorber is in a heterojunction with CdS buffer, and has Mo and ZnO:Al (AZO) as back and front contacts [55]. The CZTS absorber was prepared by two-step sulphurization process from electrodeposited Cu/Sn/Zn precursors. Always Katagiri set a new *PCE* record of 2.62% [43]: this was the first reported result for two-step sulphurization with vacuum deposited precursors. New records were established when he optimized the sulphurization process (5.4% *PCE*) [55], discovered how to etch remaining metal oxides on the surface of the absorber at the end of the annealing process (6.7% *PCE*) [56]. For analogous selenide CZTSe devices, in 1997 Friedlmeier *et al.* reported on vacuum-fabricated films, obtaining *PCE* of 0.6% [57]. By 2009 the efficiency for CZTSe devices had increased to 3.2% [58]. This record survived till for the first time chalcogens intermixing is introduced in the alloy forming CZTSSe. Mitzi and his group at IBM reported 9.7% *PCE* CZTSSe solar cells by using a hybrid particle-solution approach [59]. The CZTSSe absorber layers for these devices were deposited using two-step approach where precursors are dissolved in hydrazine and spin-coated on Mo-coated glass followed by annealing [59]. In 2010 the group of Agrawal at Perdue

University (USA) introduced for the first time germanium in the alloy forming CZGeTSSe leading to a 8.4% *PCE* [60]. In the two years following (2011-2012), Todorov *et al.* pushed the PCE to 10.1% and 11.1% then still using hybrid particle-solution method [61]. In 2012 Repins *et al.* set a new record for coevaporated CZTSe (9.5%) [62].

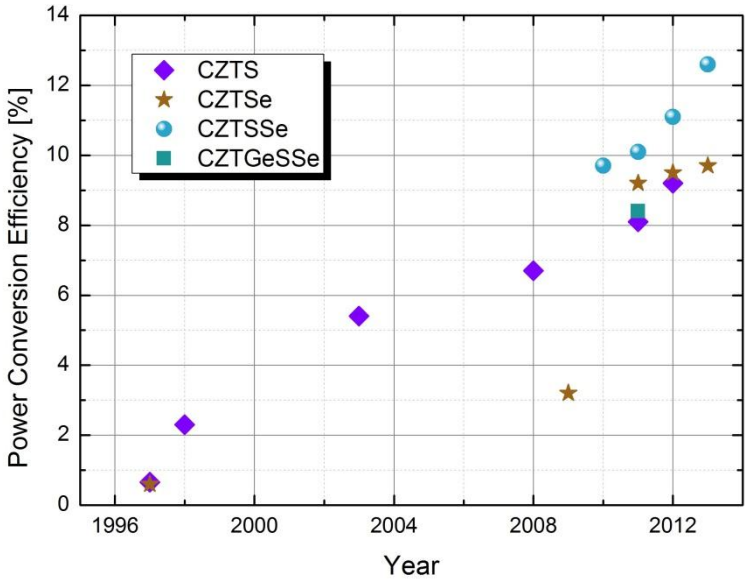

Figure 21: Evolution of the record *PCE* of CZTSSe solar cells as a function of years.

In 2013 Kato *et al.* and Brammertz *et al.* reported the new records for pure CZTS (9.2% using co-sputtering) [63] and CZTSe (9.7% using co-evaporation) [52]. Nowadays the world record efficiency for CZTSSe solar cells is at 12.6% set at IBM Watson [33]. The evolution of the conversion efficiency of CZTSSe solar cells is summarized in Figure 21.

2.5 References

[1] NREL Public Relations (2008-08-13).

[2] Orelin, IEEE Power Energ. Mag. 10 (2012) 4.

[3] H. Altomonte, IEEE Power Energ. Mag. 10 (2012) 94.

[4] Available from: http://www.altenergystocks.com/archives/2012/06/staying_alive_-could_thinfilm_manufacturers_come_out_ahead_in_the_pv_wars_part_2_1.html.

[5] NASA Solar System Exploration – Sun: Facts & Figures retrieved 27 April 2011.

[6] A. Luque, S. Hegedus, Handbook of Photovoltaic Science and Engineering (2011)
[7] A. G. Aberle, Thin Solid Films 517 (2009), pp. 4706–4710
[8] K. H. Kim, S. Kasouit, E. V. Johnson, P. R. i Cabarrocas, Solar Energy Materials and Solar Cells, 119 (2013), pp. 124-128
[9] Benagli S, Borrello D, Vallat-Sauvain E, Meier J, Kroll U, Hötzel J, Spitznagel J, Steinhauser J, Castens L, Djeridane Y. High-efficiency amorphous silicon devices on LPCVD-ZNO TCO prepared in industrial KAI-M R&D reactor. 24th European Photovoltaic Solar Energy Conference, Hamburg, September 2009.
[10] S. Ahn, S. Lee and H. Lee, 27th European Photovoltaic Solar Energy Conference, Frankfurt, 2012.
[11] http://www.pv-tech.org/news/first_solar_surpasses_ges_cdte_cell_efficiency_record
[12] P. Jackson, D. Hariskos, E. Lotter, S. Paetel, R. Wuerz, R. Menner, W. Wischmann, M. Powalla, Progress In Photovoltaics: Research and Applications 19 (2011), pp. 894–897
[13] W. Ki, H. W. Hillhouse, Adv. Energy Mater., 1(2011), pp. 732–735.
[14] M.-O. Ruault, O. Kaitasov, R. Triboulet, J. Crestou, M. Gasgnier, Journal of Crystal Growth, 143 (1994), pp. 40-45
[15] S. Chen, X. G. Gong, PHYSICAL REVIEW B 79 (2009), pp. 165211
[16] A. Walsh, S. Chen, S.-H Wei, X.-G. Gong, Advanced Energy Materials, 2 (2012), pp. 400-409
[17] S. Chen, X. G. Gong, A. Walsh, S. H. Wei, APPLIED PHYSICS LETTERS 94 (2009), pp. 041903
[18] S. Chen, A. Walsh, J. Yang, X. G. Gong, L. Sun, P. X. Yang, J. H. Chu, S. H. Wei, PHYSICAL REVIEW B 83(2011), pp. 125201
[19] I.D. Olekseyuk, I.V. Dudchak, L.V. Piskach, Journal of Alloys and Compounds 368 (2004), pp. 135-143.
[20] M. Y. Valakh, V. M. Dzhagan, I. S. Babichuk, X. Fontane, A. Perez-Rodriquez, S. Schorr, JETP Letters 98 (2013), pp. 255-258
[21] A. Lafond, L. Choubrac, C. Guillot-Deudon, P. Deniard, S. Jobic, Zeitschrift fur Anorganische und Allgemeine Chemie, 638 (2012), pp. 2571-2577.
[22] S. Harel, C. Guillot-Deudon, L. Choubrac, J. Hamon, A. Lafond, Applied Surface Science, 303 (2014), pp. 107-110.

[][23] K. Muska, M. Kask, M. Altosaar, M. Pilvet, M. Grossberg, O. Volobujeva, Energy Procedia 10 (2011), pp. 203
[24] S. Schorr, Solar Energy Materials and Solar Cells, 95 (2011), pp. 1482–1488
[25] J. J. Scragg, L. Choubrac, A. Lafond, T. Ericson, C. Platzer-Björkman, Applied Physics Letters, 104 (2014), pp. 041911
[26] E. Zillner, A. Paul, J. Jutimoosik, S. Chandarak, T. Monnor, S. Rujirawat, R. Yimnirun, X. Z. Lin, A. Ennaoui, T. Dittrich, M. Lux-Steiner, Applied Physics Letters 102 (2013), pp. 221908
[27] J. He, L. Sun, S. Chen,Y. Chen, P.Yang, J. Chu, J. Alloys Compd. 511 (2012), pp. 129
[28] S. Levcenco, D. Dumcenco, Y.P.Wang, Y.S. Huang, C.H. Ho, E. Arushanov, V. Tezlevan, K.K. Tiong, Opt. Mater. 34 (2012), pp. 1362
[29] S. M. Sze, K. K. NG, Physics of semiconductor devices, Wiley 2007
[30] S. Chen, L. Wang, X. G. Gong, A. Walsh, S. H. Wei, Appl. Phys. Lett. 101(2012), pp. 223901
[31] T. Maeda, S. Nakamura, T. Wada, Japanese Journal of Applied Physics, 50 (2011), pp. 04DP07
[32] K. Biswas, S. Lany, and A. Zunger, Appl. Phys. Lett.96 (2010), pp. 201902
[33] W. Wang, M. T. Winkler, O. Gunawan, T. Gokmen, T. K. Todorov, Y. Zhu, D. B. Mitzi, Adv. Mater., doi: 10.1002/aenm.201301465

[34] S. Delbos, EPJ Photovoltaics 3 (2012), pp. 35004
[35] P.A. Fernandes, P.M.P. Salomé, A. F. da Cunha, Journal of Alloys and Compounds 509 (2011), pp. 7600-7606

[36] G. Altamura, L. Grenet, C. Bougerol, E. Robin, D. Kohen, H. Fournier, A. Brioude, S. Perraud, H. Mariette, Journal of Alloys and Compounds 588 (2014), pp. 310–315

[37] L. Grenet, S. Bernardi, D. Kohen, C. Lepoittevin, S. Noel, N. Karst, A. Brioude, S. Perraud, H. Mariette, Solar Energy Materials and Solar Cells 101 (2012), pp. 11-14.

[38] M. Ganchev, J. Iljina, L. Kaupmees, T. Raadik, O. Volobujeva, A. Mere, M. Altosaar, J. Raudoja, E. Mellikov, Thin Solid Films 519 (2011), pp. 7394–7398

[39] J. C. González, P. A. Fernandes, G. M. Ribeiro, A. Abelenda, E. R. Viana, P. M. P. Salomé, A. F. Da Cunha, Solar Energy Materials and Solar Cells, 123 (2014), pp. 58-64
[40] P. A. Fernandes, P. M. P. Salomé, A. F. Sartori, J. Malaquias, A. F. Da Cunha, B. Schubert, G. M. Ribeiro, Solar Energy Materials and Solar Cells, 115 (2013), pp. 157-165
[41] R. Djemour, A. Redinger, M. Mousel, L. Gütay, X. Fontané, V. Izquierdo-Roca, S. Siebentritt, 21 (2013), pp. A695-A703
[42] M. Mousel, A. Redinger, R. Djemour, M. Arasimowicz, N. Valle, P. Dale, S. Siebentritt, Thin Solid Films, 535 (2013), pp. 83-87
[43] H. Katagiri, K. Jimbo, W.S. Maw, K. Oishi, M. Yamazaki, H. Araki, A. Takeuchi, Thin Solid Films, 517 (2009), pp. 2455-2460.

[44] V. Chawla, B. Clemens, Proceedings of the 38th IEEE Photovoltaic Specialists Conference 2012, pp.2990–2992.

[45] A. Redinger , D. M. Berg, P. J. Dale, S. Siebentritt, J. Am. Chem. Soc., 133 (2011), pp. 3320–3323
[46] A.V. Moholkar, S.S. Shinde, G.L. Agawane, S.H. Jo, K.Y. Rajpure, P.S. Patil, C.H. Bhosale, J.H. Kim, Journal of Alloys and Compounds, 544 (2012), pp. 145-151

[47] S. W. Shin, S.M. Pawar, C. Y. Park, Jae Ho Yun, Jong-Ha Moon, Jin Hyeok Kim, Jeong Yong Lee, Solar Energy Materials & Solar Cells, 95 (2011), pp. 3202–3206.
[48] K. Jimbo, R. Kimura, T. Kamimura, S. Yamada, W.S. Maw, H. Araki, K. Oishi, H. Katagiri, Thin Solid Films 515 (2007), pp. 5997.
[49] W. Xinkun, L. Wei, C. Shuying, L. Yunfeng, J. Hongjie, J. Semiconductors 33 (2012), pp. 022002
[50] N. Sakai, H. Hiroi, H. Sugimoto, 37th IEEE PVSC Conference (2011)
[51] A. Redinger, D.M. Berg, P.J. Dale, S. Siebentritt, J. Am. Chem. Soc. 156 (2011)
[52] T. Kato, H. Hiroi, N. Sakai, S. Muraoka, H. Sugimoto, 27th EPSEC, Frankfurt (2012)
[53] H. Xin, H.W. Hillhouse, 8.3% Efficient copper zinc tin sulfoselenide solar cells processed from environmentally benign solvent, in: Proceedings of the 39th IEEE Photovoltaic Specialists Conference, 2013.

[54] S. Ahmed, K.B. Reuter, O. Gunawan, L. Guo, L.T. Romankiw, H. Deligianni, A high efficiency electrodeposited Cu2ZnSnS4 solar cell, Advanced Energy Materials 2 (2012) 253–259.

[55] H. Katagiri, N. Sasaguchi, S. Hando, S. Hoshino, J. Ohashi, T. Yokota, Solar Energy Materials & Solar Cells, 49 (1997), pp. 407-414.

[56] H. Katagiri, K. Jimbo, S. Yamada, T. Kamimura, W.S. Maw, T. Fukano, T. Ito, T. Motohiro, Applied Physics Express, 1 (2008), pp. 041201.

[57] T. M. Friedlmeier, N. Wieser, T. Walter, H. Dittrich, H. W. Schock, Proceedings of the 14th European Photovoltaic Solar Energy Conference (1997), pp.1242–1245.

[58] G. Zoppi, I. Forbes, R. W. Miles, P. J. Dale, J. J. Scragg, L. M. Peter, Prog. Photovolt.: Res.Appl.17(2009), pp. 315–319.

[59] D.B. Mitzi, M. Yuan, W. Liu, A.J. Kellock, S.J. Chey, V. Deline, A.G. Schrott, Advanced Materials, 20 (2008), pp. 3657-3662.

[60] Q. Guo, G.M. Ford, H.W. Hillhouse, R. Agrawal, Proceedings of the 37th IEEE Photovoltaic Specialists Conference, 2011, pp. 003522–003526.

[61] T. Todorov, O. Gunawan, S.J. Chey, T.G. De Monsabert, A. Prabhakar, D.B. Mitzi, Progress towards marketable earth-abundant chalcogenide solar cells, Thin Solid Films 519 (2011) 7378-7381.

[62] I. Repins, C. Beall, N. Vora, C. DeHart, D. Kuciauskas, P. Dippo, B. To, J. Mann, W. C. Hsu, A. Goodrich, R. Noufi, Solar Energy Materials and Solar Cells, 101 (2012), pp. 154-159

[63] G. Brammertz, M. Buffière, S. Oueslati, H. ElAnzeery, K. Messaoud, S. Sahayaraj, C. Köble, M. Meuris, J. Poortmans, Applied Physics Letters, 103 (2013), pp. 163904

Chapter 3

Experimental

Outline

3.1 Fabrication techniques

Two-step processes, in which precursors are vacuum-deposited and then selenized or sulfurized, have attracted a lot of attention not only as a technique suitable for large-scale module production (as for CIGS) [1], but also as one of the methods with the highest potential to yield high cell and module efficiencies [2-3, 4-13]: up to 9.7% power efficiencies have been achieved by IMEC [14].

In the work presented in this manuscript, the CZTSSe absorber has been always obtained by two-step selenization process: firstly a stack of ZnS/Cu/Sn precursors are deposited by physical vapor deposition (PVD), secondly this stack has been annealed under selenium atmosphere in order to achieve the final CZTSSe material. Further details on this technique are listed in this chapter.

3.1.1 Molybdenum back contact

The back contact (BC) employed in the elaboration of the CZTSSe solar cell is a 450 nm layer of molybdenum. It is deposited by DC-sputtering in a Perkin Elmer system at room temperature under 1×10^{-4} Torr argon atmosphere on a 1 mm-thick soda-lime glass (SLG) substrate. During deposition process the sample is rotating in order to increase homogeneity. The choice of Mo as BC for CZTSSe solar cell is an inheritance of CIGS technology [15], where it has been identified as the best performing BC. Mo can react with Se during selenization process to form $MoSe_2$. The $MoSe_2$ is a semiconductor with a gap of 1.41 eV [15] and has the effect, for a specific crystal orientation, of forming an ohmic contact at Mo|absorber interface [15].

3.1.2 Precursor deposition

Starting from a Mo-coated SLG substrate deoxidized for 10 seconds in a 10% NH_3 solution, two different PVD techniques are used to deposit the precursors. First ZnS-layer is deposited via RF-sputtering in a Plassys MP400 system under 1×10^{-3} mbar of Ar at room temperature. Then the metallic layers of Cu and Sn are grown by high vacuum electron-beam evaporation in a Plassys MEB550S deposition chamber at 5×10^{-7} mbar. In both cases, deposition rates are monitored by a quartz balance. These precursor thicknesses have been

chosen to create a Zn-rich and Cu-poor CZTSSe layer as used in most efficient CZTSSe-based solar cells [3]. The stacking order of precursors (Figure 22) could be shifted in order to study the different reaction mechanism during selenization process; this topic will be analyzed in details in chapter 4.

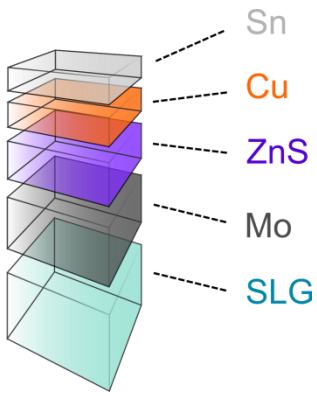

Figure 22: Schematic of the precursor stack prior to selenization process.

3.1.3 Selenization

The selenization of precursors to synthesize CZTSSe material occurs in a tubular furnace under Ar atmosphere. A cross-section of the furnace setup is shown in Figure 23. It is composed of a quartz tube where the inner pressure can be varied by playing on the Argon inlet and the pump. The precursor stack is positioned on the middle of a graphite support (graphite is an inert material): it has a good thermal conductivity and used to provide a low temperature gradient along the thickness of the sample. A thermocouple is integrated in the graphite in order to check the temperature fluctuation during annealing process. Selenium is provided in the form of pellets placed in close proximity of the precursor stack to assure proper selenization. Samples are annealed using a halogen lamp perpendicular to the furnace following a specific temperature profile: ramp of 1°C/s is used and stopped at 570°, at this point a temperature plateau of 570°C is maintained for 30 minutes followed by natural cooling (about 1 hour). With this technique it is possible to produce a final $Cu_2ZnSn(S_{0.15}Se_{0.85})_4$ absorber with a thickness of 1.5 µm [3].

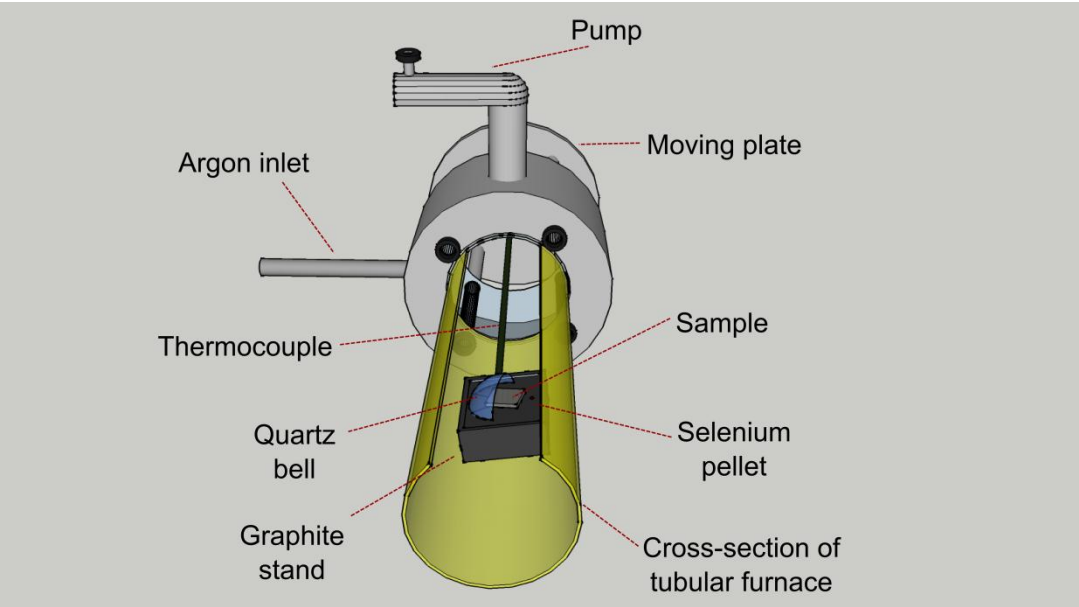

Figure 23: Cross-section of the tubular furnace employed for selenization process.

COMSOL simulations of selenization process using the profile described above demonstrate that a graphite box as heat conductor, allow having a temperature difference between the top and the bottom of the sample of only 6 degrees (see Figure 24).

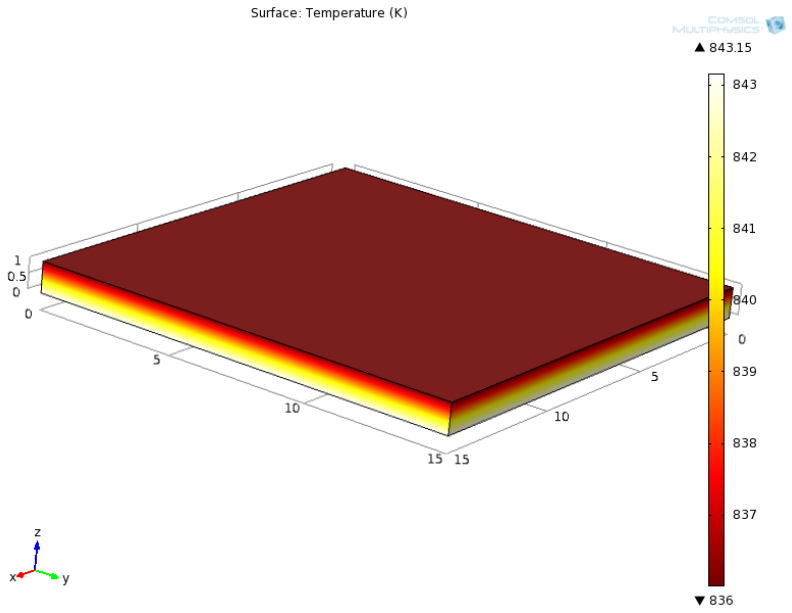

Figure 24: COMSOL simulation of temperature profile as function of the sample thickness (in millimiters).

3.1.4 Processing of the solar cell

3.1.4.1 CdS buffer layer

Solar cells are fabricated by adding a 70 nm n-type CdS layer grown by chemical bath deposition (CBD) to the CZTSSe thin films to form the hetero-junction. The CZTSSe absorber is soaked in a solution composed of cadmium acetate, thiourea and ammonia and heated on a hot plate for 11 min at 80°C. The reaction of precursors leading to the thin film CdS layer is the following:

$$Cd(NH_3)_4^{2+} + SC(NH_2)_2 + 2OH^- \rightarrow CdS + H_2NCN + 4NH_3 + 2H_2O$$

A magnetic agitator is employed to enhance uniformity. More details about CdS deposition is given in table 1.

Precursor material	Chemical formula	Concentration
Cadmium acetate	$Cd(CH_3CO_2)_2$	1.094 g/L
Thiourea	$SC(NH_2)_2$	1.54 g/L
Ammonium acetate	$NH_4C_2H_3O_2$	2.735 g/L

Table 1: CdS precursor deposition details.

3.1.4.2 Transparent conductive oxide

After CdS deposition, a combination of 50 nm i-ZnO and 450 nm Al:ZnO are grown by RF-sputtering from a pure ZnO target and from a 2% wt Al_2O_3-ZnO target respectively. The measured surface resistance of this TCO layer is around 25 Ω/☐.

3.1.4.2 Ni/Al grids

The front contact is metal grids composed of a combination of Ni and Al layers (total thickness 500 nm) deposed by e-beam evaporation using a deposition mask.

The structure of the completed CZTSSe solar cell is shown in Figure 25.

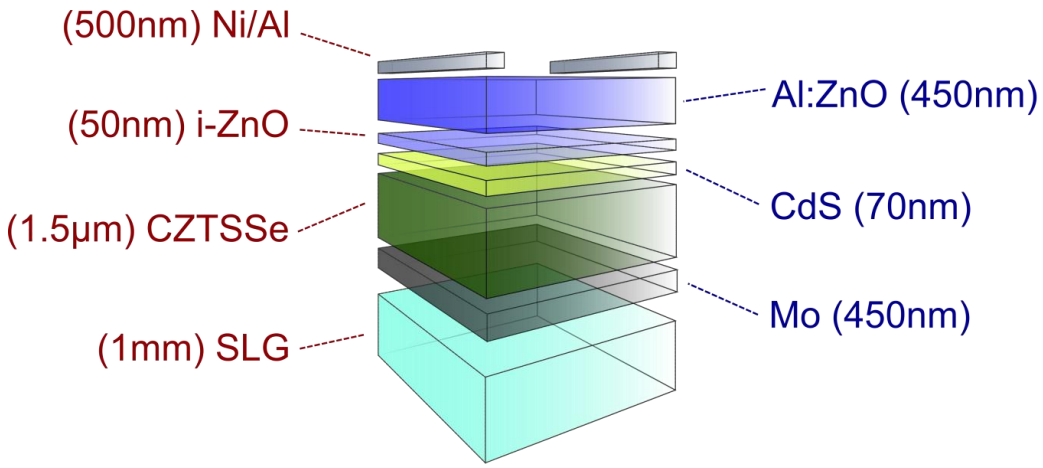

Figure 25: CZTSSe-based thin film solar cell.

3.2 Analysis techniques

In the spirit of understand and exploit the properties of quaternary compounds like CZTSSe, characterization at both material and device stage are mandatory. In particular, it is essential to monitor the compositions and elemental distribution of CZTSSe absorber, since it is not often homogeneously distributed and since these elemental distributions may affect the electrical characteristics of the CZTSSe solar cell.

3.2.1 Material analysis

3.2.1.1 Scanning Electron Microscopy

SEM has been widely employed for retrieving topological information from CZTSSe thin films on both surface and cross-sections (Figure 26). A Hitachi S4000 scanning electron microscope (SEM) is used to examine the morphology of the CZTSSe layers as well as to estimate their thicknesses. The use of the SEM requires very little in regard to sample preparation: the sample is cleaved along the surface in order to examine cross-section. CZTSSe sample is a conductor so no previous metal deposition is required. The images are taken always using a vacuum around 10^{-3} mbar and an accelerating voltage between 10 and

30 keV. The electron hitting to the sample are emitted by thermionic effect from a tungsten filament, whereas the collected electrons, giving the image, are secondary electrons resulting from the interaction of the incident beam with the sample at the point of entry.

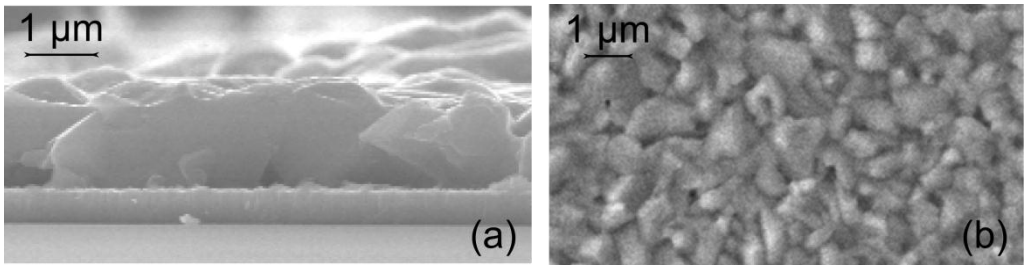

Figure 26: (a) Cross-section view of a as-annealed CZTSSe layer synthesized from a ZnS(480 nm)/Cu(180 nm)/Sn(240 nm) stack of precursors. (b) Top view of the same layer.

3.2.1.2 Energy Dispersive X-ray Spectroscopy

EDS/EDX is an analytical technique used for the elemental analysis of all the elements in the periodic table above beryllium. It exploits the emission of X-rays generated by an accelerated electron beam incident on the sample. CZTSSe measurements are performed at 25 kV in a Phillips XL30 SEM to determine the global chemical composition of the layers. Cross-sectional EDS is also performed in a Zeiss Ultra55 SEM at 30 kV using a micro-analysis system equipped with a 30 mm^2 SDD detector from Bruker. In particular cross-sections are prepared by mechanical polishing up to 30 microns followed by ion milling up to electron transparency (Gatan PIPS system operated at 3kV). Concerning the constituent elements of CZTSSe, the minimum detection limit (MDL) is as low as 0.2% wt. For elements like sodium (Na will be the main subject in chapter 5) the MDL is usually around 1-2% wt. under the best conditions. In our analysis, the main results giving out of the EDS analysis are the atomic cation (*[Zn]/[Sn]*, *[Cu]/[Zn+Sn]*) and anion (*[S+Se]/[Cu+Zn+Sn]*, *[S]/[S+Se]*) ratio compositions. They estimate the distance from stoichiometry: portraits of analysis made on CZTSSe in top and cross-sectional mode are depicted in Figure 27.

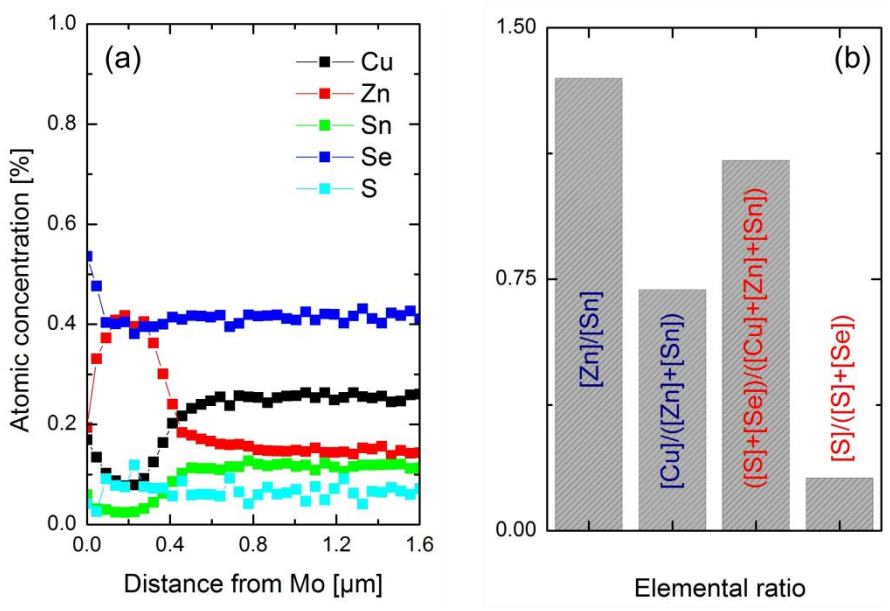

Figure 27: (a) Cross-section EDS analysis of a as-annealed CZTSSe layer synthesized from a ZnS(480 nm)/Cu(180 nm)/Sn(240 nm) stack of precursors. (b) Top EDS of the same layer.

3.2.1.3 X-Ray Diffraction

XRD is a powerful technique used to identify crystallographic and structural properties present of a material. The presence and composition of crystalline phases of CZTSSe layer are characterized by XRD and grazing incidence X-ray diffraction (GIXRD) in a D8 Advance Bruker AXS.

The diffraction patterns of minor phases like $Zn(S_x,Se_{1-x})$, $Cu_2Sn(S_x,Se_{1-x})_3$ are difficult to be identified by XRD due to superposition of their spectral lines with $Cu_2ZnSn(S_x,Se_{1-x})_4$ phase. Therefore, it is difficult to ascertain right minor phase from XRD but the remaining phases such as $Sn(S_x,Se_{1-x})$, $SnS(S_x,Se_{1-x})_2$, or $Cu_2(S_x,Se_{1-x})$ can indisputably be recognizable.

XRD has also been used to estimate the crystallite size of CZTSSe by using Scherrer's equation:

$$D = \frac{K\lambda}{B\cos\theta} \qquad \text{(eq. 12)}$$

where D is the mean size of the crystallite (it could be smaller or equal to the grain size), K is a dimensionless factor around 0.9, λ is the X-ray wavelength, B is the line broadening at half the maximum intensity (FWHM), after subtracting the instrumental line broadening, in radians, and θ is the Bragg angle.

3.2.1.4 Raman spectroscopy

Raman spectroscopy is a spectroscopic technique used to observe vibrational modes of materials. It is based on Raman scattering (inelastic scattering) of monochromatic light, usually from a laser in the visible, near-infrared, or near-ultraviolet range. The energy difference between the incident photons and those released inelastically by the sample corresponds to the vibrational energy levels of the molecule diffusing: the analysis of the shift of the spectral lines due to Raman Effect can therefore provide information on the chemical composition, molecular structure, and intermolecular interactions of the sample.

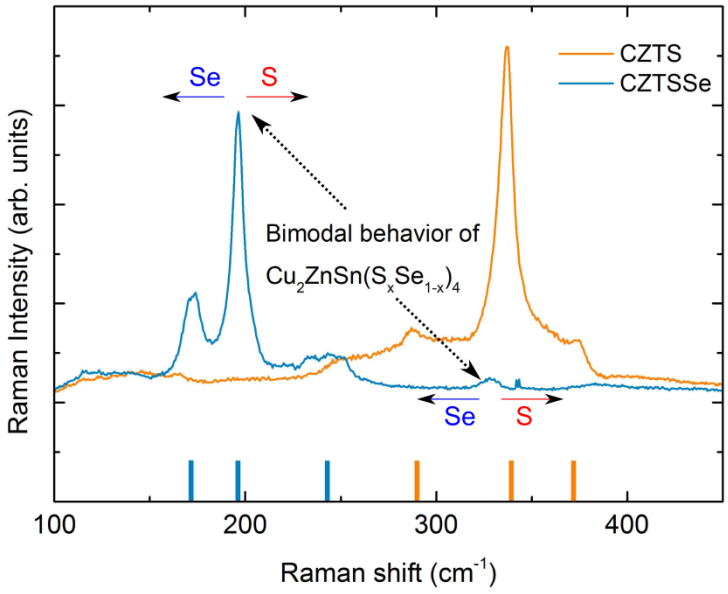

Figure 28: Raman spectra of pure CZTS and CZTSSe with 90% selenium layers. Main peaks of CZTS and CZTSe [15] are reported.

Raman spectroscopy is primarily a structural characterization tool useful to check the presence of minor phases. Confocal Raman spectroscopy is used in a backscattering

configuration with 10 mW 532 nm green laser excitation. Raman spectroscopy results also convenient to observe the bimodal behavior of CZTSSe compounds demonstrated by Grossberg *et al.* [16]: a variation in the chalcogens concentration (S, Se) will shift the CZTS and CZTSe A1 Raman modes towards higher (S-content increasing) or lower wavenumber (Se-content increasing) (See Figure 28).

3.2.1.5 Glow Discharge Spectroscopy

A GDS tool is used to evaluate the elemental depth profile in CZTSSe: the glow discharge Ar plasma source (in our case 13.56 MHz radio frequency power) provides a very fast sputtering rate of the order of µm/min, and an optical spectrometer for the real-time detection of etched species is used for determining the elemental depth profiles as a function of the thickness of the layer (30 nm spatial resolution).

Figure 29 shows a typical GDS spectrum of CZTSSe layer synthesized on Mo.

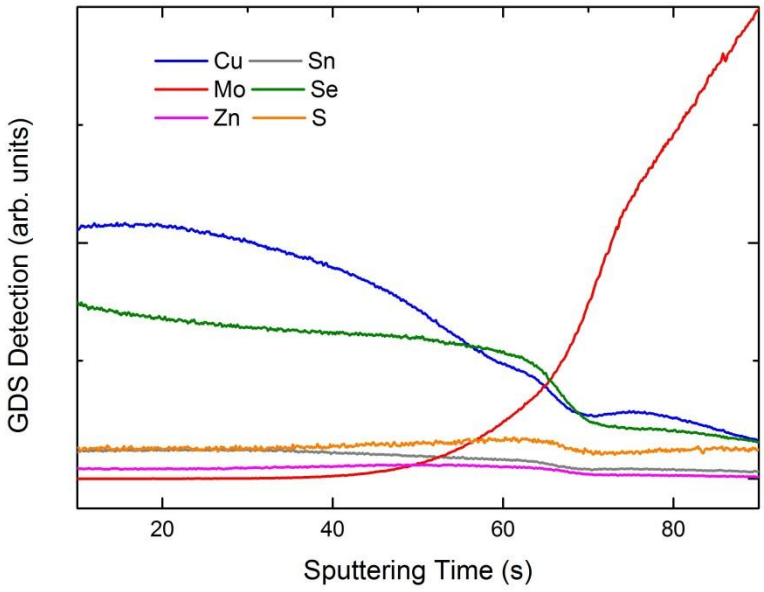

Figure 29: GDS spectrum of CZTSSe material synthesized on Mo.

3.2.1.6 Photoluminescence

PL is mainly used to study the material quality and intrinsic properties of CZTSSe. As for Raman spectroscopy, this method is very useful to quantify the chalcogens ratio inside CZTSSe compounds as reported in Ref. 15 (Figure 30).The spectral analysis of the PL is performed at low temperature (8 K) using a thermo-electrically cooled Andor InGaAs CCD. PL spectrum is excited by different femtosecond lasers at 365 and 780 nm with an average power between 20 and 120 mW.

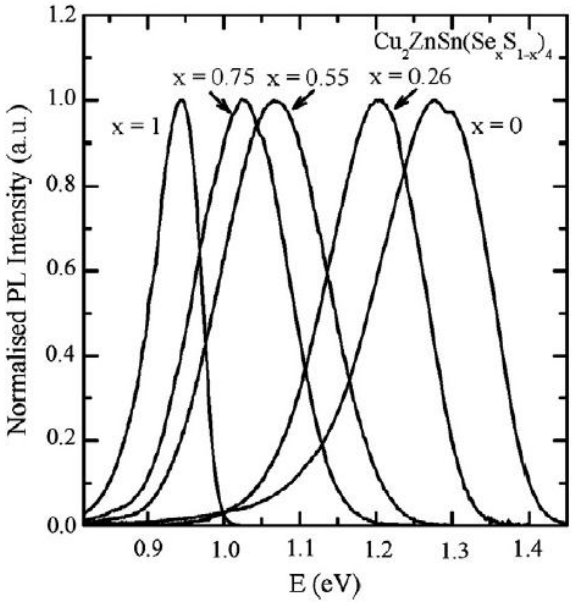

Figure 30: Normalized low-temperature photoluminescence spectra of the CZTSSe from Ref. 15

3.2.2 Cells analysis

3.2.2.1 Light current-voltage measurements

Light current-voltage measurements allow establishing the *PCE* of a solar cell. The need of comparison between devices manufactured at different companies and laboratories using different technologies boosted the necessity of find a standardized method of analysis.

The standards for cell testing are:

- AM1.5 for terrestrial cells and AM0 for space cells.
- Intensity of 1 kW/m^2 (one-sun of illumination)

- Cell temperature of 25 °C
- Four point probe

This standard is respected in the measurement of CZTSSe solar cell using a Spectra-Nova's CT Series Solar Cell Tester.

3.2.2.2 Dark current-voltage measurements

Dark current-voltage (dark I-V) measurements are commonly employed to evaluate the electrical characteristics of solar cells. The dark I-V measurement procedure does not provide information regarding the four figures of merit described in 2.1.8, but is more sensitive than light I-V measurements in determining loss parameters (R_s, R_{sh}, n, I_0) that dictate the electrical performance of a solar cell.

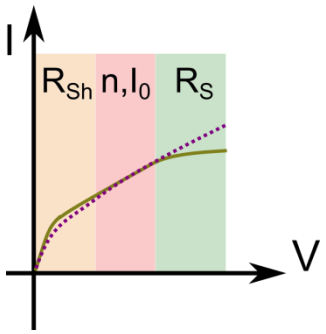

Figure 31: The olive curve is a typical dark I-V characteristic. The wine dashed curve shows the same device without the parasitic resistances (Law Shockley). The colored areas indicate where the different parameters are extracted: R_{sh} (yellow), n and I_0 (red) and R_s (green).

The extraction method is to perform parameter interpolation in the three areas of the curve (see Figure 31). R_{sh} can thus be extracted performing a linear regression of the curve around 0 V. R_s is obtained with a linear regression at high voltage. Finally, I_0 and n are obtained by interpolation of the exponential portion of the curve using the equation 3. I-V measurements are performed in darkness with a sourcemeter Keithley 2601A.

3.2.2.3 External Quantum Efficiency measurement

EQE indicates the ratio of the number of photons incident on a solar cell to the number of generated charge carriers. It is extracted from the spectral response of CZTSSe solar cells. It is defined as:

$$EQE(\lambda, V) = \int T_F(\lambda)\alpha(\lambda)e^{-\alpha(\lambda)x}\eta_C(x, V)\, dx \qquad \text{(eq. 13)}$$

where α and η_c are known, and T_F is is the fraction of incident light reaching the CZTSSe layer and is defined by:

$$T_F(\lambda) = \big(1 - R(\lambda)\big).\big(1 - a_{CdS+TCO}(\lambda)\big) \qquad \text{(eq. 14)}$$

where, R is the reflection of the CZTSSe/CdS/TCO structure and $a_{CdS+TCO}$ is the absorption into the buffer and window layers.

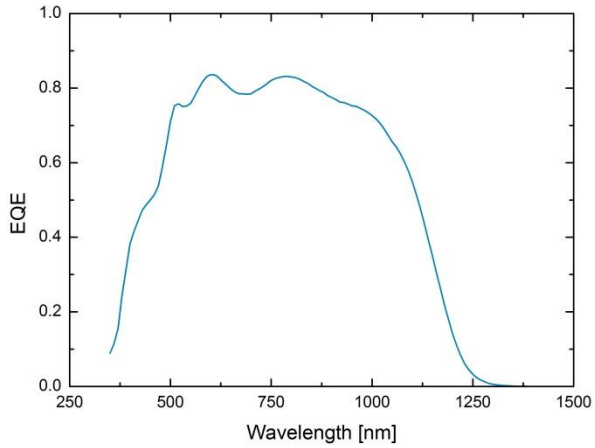

Figure 32: External quantum efficiency of a typical Mo|CZTSSe|CdS|TCO

EQE measurements are carried out in a Lot Oriel Spequest with a monochromator under chopped illumination and a lock-in technique.

3.3 References

[1] A. Luque, S. Hegedus, Handbook of Photovoltaic Science and Engineering, Second Edition, Chapter 13, Wiley and Sins, Ltd., Publication, 2011.

[2] H. Katagiri, K. Jimbo, S. Yamada, T. Kamimura, W.S. Maw, T. Fukano, T. Ito,T. Motohiro, Proceedings of Photovoltaic Energy Conversion Conference Vol. 3 (2003).

[3] L. Grenet, S. Bernardi, D. Kohen, C. Lepoittevin, S. Noel, N. Karst, A. Brioude, S. Perraud, H. Mariette, Cu2ZnSn(S1-xSex)4 based solar cell produced by selenization of vacuum deposited precursors, Solar Energy Materials and Solar Cells 101 (2012) 11-14.

[4] H. Yoo, R.A. Wibowo, A. Hölzing, R. Lechner, J. Palm, S. Jost, M. Gowtham, F. Sorin, B. Louis, R. Hock, Investigation of the solid state reactions by time-resolved X-ray diffraction while crystallizing kesterite Cu2ZnSnSe4 thin films, Thin Solid Films 535 (2013) 73–77.

[5] R.B.V. Chalapathy, Gwang Sun Jung, Byung Tae Ahn, Fabrication of Cu2ZnSnS4 films by sulfurization of Cu/ZnSn/Cu precursor layers in sulfur atmosphere for solar cells, Solar Energy Materials & Solar Cells 95(2011) 3216–3221.

[6] C. Platzer-Bjorkman, J. Scragg, H. Flammersberger, T. Kubart, M. Edoff, Influence of precursor sulfur content on film formation and compositional changes in Cu2ZnSnS4 films and solar cells, Solar Energy Materials & Solar Cells 98 (2012), 110–117

[7] G. Brammertz, M. Buffiere, Y. Mevel, Y. Ren, A. E. Zaghi, N. Lenaers, Y. Mols, C. Koeble, J. Vleugels, M. Meuris, J. Poortmans, Correlation between physical, electrical, and optical properties of Cu2ZnSnSe4 based solar cells, APPLIED PHYSICS LETTERS 102 (2013), 013902

[8] S. W. Shin, S.M. Pawar, C. Y. Park, Jae Ho Yun, Jong-Ha Moon, Jin Hyeok Kim, Jeong Yong Lee, Studies on Cu2ZnSnS4 (CZTS) absorber layer using different stacking orders in precursor thin films, Solar Energy Materials & Solar Cells 95 (2011) 3202–3206.

[9] K. Jimbo, R. Kimura, T. Kamimura, S. Yamada, W.S. Maw, H. Araki, K. Oishi, H. Katagiri, Cu2ZnSnS4-type thin film solar cells using abundant materials, Thin Solid Films 515 (2007) 5997.

[10] W. Xinkun, L. Wei, C. Shuying, L. Yunfeng, J. Hongjie, Photoelectric properties of Cu2ZnSnS4 thin films deposited by thermal evaporation, J. Semiconductors 33 (2012), 022002

[11] N. Sakai, H. Hiroi, H. Sugimoto, Development of cd-free buffer layer for Cu2ZnSnS4 thin-film solar cells, in 37th IEEE PVSC Conference (2011)

[12] A. Redinger, D.M. Berg, P.J. Dale, S. Siebentritt, The Consequences of Kesterite Equilibria for Efficient Solar Cells, J. Am. Chem. Soc. 156 (2011)

[13] T. Kato, H. Hiroi, N. Sakai, S. Muraoka, H. Sugimoto, Characterization of front and back interfaces in on Cu2ZnSnS4 thin film solar cells, 27th EPSEC, Frankfurt (2012)
[14] G. Brammertz, M. Buffière, S. Oueslati, H. ElAnzeery, K. Messaoud, S. Sahayaraj, C. Köble, M. Meuris, J. Poortmans, Applied Physics Letters, 103 (2013), pp. 163904
[15] N Kohara, Solar Energy Materials and Solar Cells, 67(2001), pp. 209–215
[16] M. Grossberg, J. Krustok, J. Raudoja, K. Timmo, M. Altosaar, T. Raadik, Thin Solid Films, 519 (2011), p. 7403

Chapter 4

Formation mechanism of $Cu_2ZnSn(S,Se)_4$

Outline

4.1 Motivation

CZTSSe compound is a complex material due to its number of constituents. In order to increase the efficiency of CZTSSe-based solar cells, and engineer new solutions to this scope, it is important to understand the mechanism of formation of the absorber starting from its raw components. As described in 2.4.2.4, it is very complicated to achieve a single-phase CZTSSe material without spurious minor phases. In particular the highest efficiency devices have all been obtained for materials with Zn-rich and Cu-poor compositions [1], with a cations ratios ([Cu]/([Zn]+[Sn])) around 0.85, and [Zn]/[Sn] around 1.20 [1]. It is reported experimentally [3-4] that Zn-rich/Cu-poor absorbers could promote, in most of the cases, the formation of resistive Zn(S,Se) phase which increase series resistance [5] and limit device performance.

The predicted reaction pathway for CZTSSe [6-7] is shown in equation 15, where *X* is for the chalcogens S and Se:

$$C_2ZTX_4(s) \leftrightharpoons \left(Cu_2X(s) + SnX(s) + ZnX(g) + \frac{1}{2}X(g)\right) \qquad \text{(eq. 15)}$$

The possibility to reduce the formation of minor phases is fundamental to improve CZTSSe solar cell efficiency.

4.2 Two-step selenization process

J. Scragg *et al.* claims that the search for the *"best fabrication route for CZTSSe"* [8] is not able to leave two requirements out of consideration: (i) a single phase material by simultaneous deposition of all the components, (ii) suppress tin losses [6] by annealing of CZTSSe under overpressure chalcogens and tin atmosphere. Precursor deposition and annealing must be stringed together (two-step process) when these two criteria are not achievable within a single system.

Two-step processes, in which precursors are vacuum-deposited and then selenized or sulfurized, have attracted a lot of attention not only as a technique suitable for large-scale module production (as for CIGS [9]), but also as one of the methods with the potential to yield high cell and module efficiencies [10-16]: up to 10.8% power efficiencies have been achieved by Solar Frontier [17].

During annealing process the chalcogens could be delivered by elemental S or Se atmosphere carried with an inert gas like Ar or N_2 [6, 8, 11], employing hydrogenated chalcogens atmosphere (H_2S, H_2Se) with a carrier gas [14, 18].

One of the main issues when using such a two-step process is the homogeneity of the obtained CZTSSe film: due to the incorporation difference of chalcogens, the material could be heterogeneous and CZTSSe could be obtained with a gradient of composition. One of the main parameters to control this issue is the order in which the thin films of the precursors are stacked (the stacking order) as already demonstrated by Fernandes *et al.* [19]. Yoo *et al.* [20] reported that it is possible to control the cuprous secondary phases in kesterite CZTS thin films by playing on the stacking order of Cu-poor metallic precursors.

4.2.1 Different precursor stacks

In this study, several CZTSSe thin films are prepared from two stacks of precursors named stack A and stack B, differing by the precursor deposition order. Both of the stacks start with a ZnS layer on a 5×5 cm^2 Mo-coated SLG, but then the deposition of Cu and Sn is inverted (Figure 30). The details of the precursor stacks are presented in table 1. These precursor thicknesses have been chosen to create a Zn-rich CZTSSe layer as used in efficient CZTSSe-based solar cells [1].

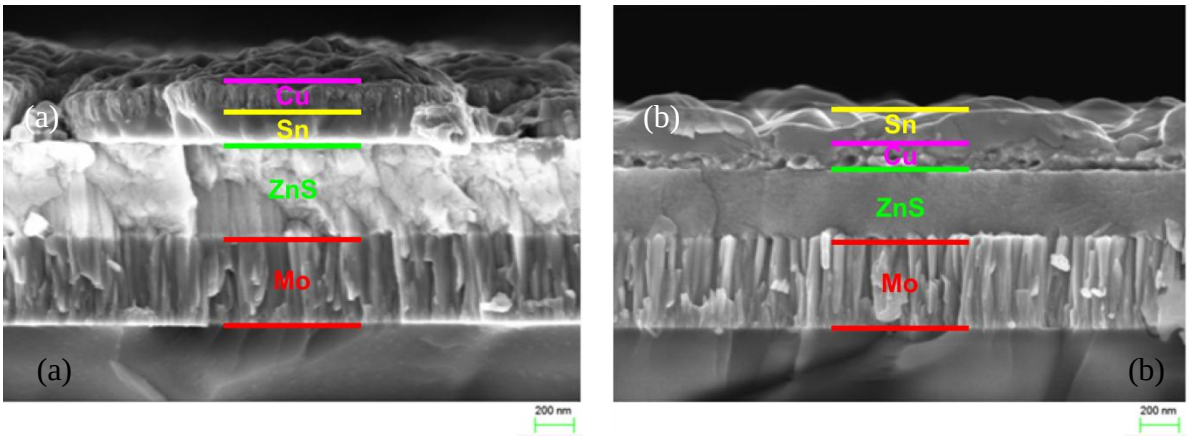

Figure 33: SEM images of different precursor stacks before annealing: stack A (a) and stack B (b).

Sample Name	Precursor stack	Technique of deposition	Thickness (nm)
Stack A	ZnS	Sputtering	460±40
	Sn	Evaporation	240±5
	Cu	Evaporation	180±5
Stack B	ZnS	Sputtering	460±40
	Cu	Evaporation	180±5
	Sn	Evaporation	240±5

Table 1: Precursor deposition details.

The cross-section of stack A in Figure 33a shows flat ZnS deposition profile and a Cu-profile quite irregular on the top. ZnS layer thickness in Figure 33b is thinner than stack A because it corresponds to an image taken on the edge of the glass substrate where the deposition rate is not uniform. Any characterization results reported in this chapter are taken on a region of CZTSSe material where the precursor's deposition rate is uniform.

Grazing-incidence X-ray diffraction is used to study material surfaces because the wave has very limited penetration [21]. In our case, it is used to characterize the precursor stacks and particularly the top metallic layers (Cu and Sn) before the selenization process. Within the experimental conditions, the depth of analysis has been estimated to be 250 nm, which means that the focus is on the top metallic layers and that the underlying ZnS layer is

excluded from the analysis. GIXRD on both stacks shows (Figure 34) that before selenization process, there is an intermixing between Cu and Sn at the interface leading to the formation of a Cu_6Sn_5 alloy. This intermixing is probably due to the radiated heat from the source material during evaporation.

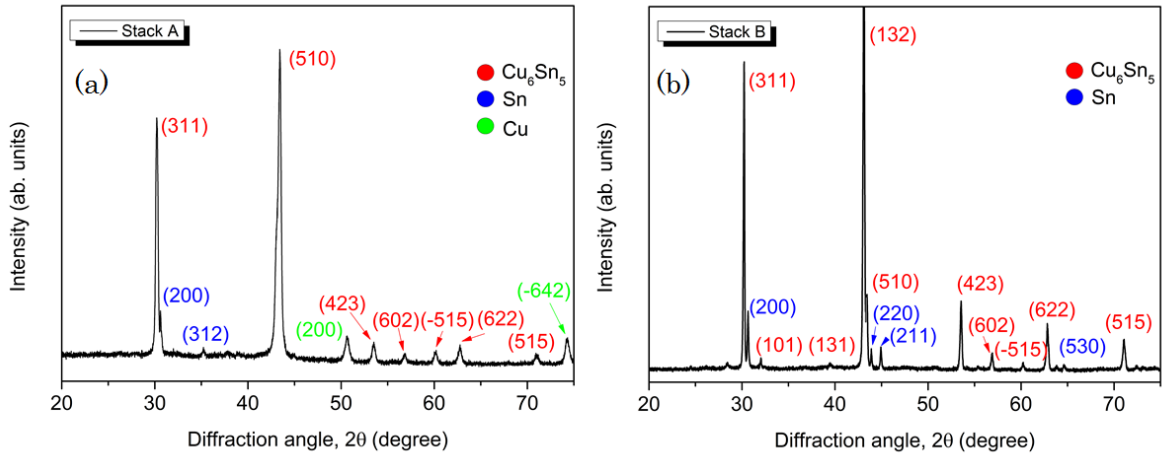

Figure 34: Grazing incidence XRD spectra of Stack A(a) and Stack B(b) before the selenization process. The diffraction peaks are indexed utilizing the International Center for Diffraction Data for Cu5Sn6 (01-072-8761), Cu (00-004-0836), Sn (03-065-0296).

4.2.2 Selenization annealing

The selenization of precursors to synthesize CZTSSe layers occurs in a tubular furnace under Ar atmosphere. Selenium is provided in the form of pellets placed in close proximity to the precursors to assure proper selenization (details on the selenization process are given in 3.1.3).

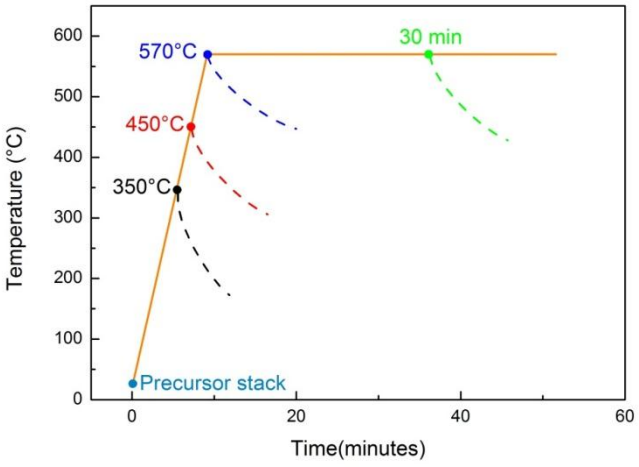

Figure 35: Temperature profiles of the samples which underwent selenization at 350°C, 450°C and 570°C (with and without the thermal plateau).

Four samples of each stack are prepared and each of them are selenized with a different temperature profile: ramps of 1 °C/s are used and stopped at the desired final temperature (350°C for the first one - 450°C for the second one - 570°C for the third one) followed by natural cooling. For the four samples, a temperature plateau of 570°C is maintained for 30 minutes. In all cases, the cooling time is about 1 hour (Figure 35).

4.3 The effects of precursor order on film growth

4.3.1 Study of the selenization process by SEM

Figure 36 and 37 show scanning electron microscopy cross-sectional views of stack A and stack B respectively after the selenization process at different temperatures. We estimate the final CZTSSe layer thickness to be around 1.5 µm for both samples. After selenization at 350°C and 450°C (Figure 36-37a and 36-37b, respectively) two layers are identifiable above the Mo film. Top layer in Figure 36b could induce a doubt concerning the possibility of having a double layer on top of ZnS: this is not true since it is only an artifact due to the not-perfect cleavage of the cross-section. A ZnS-like layer is identified closest to the Mo interface. This proves that the different precursors undergo incomplete selenization. After selenization at 570°C (Figure 36-37c), SEM characterization confirms a decrease in the ZnS-like layer thickness, and confirms partial intermixing of all the precursor elements before the plateau of temperature is reached.

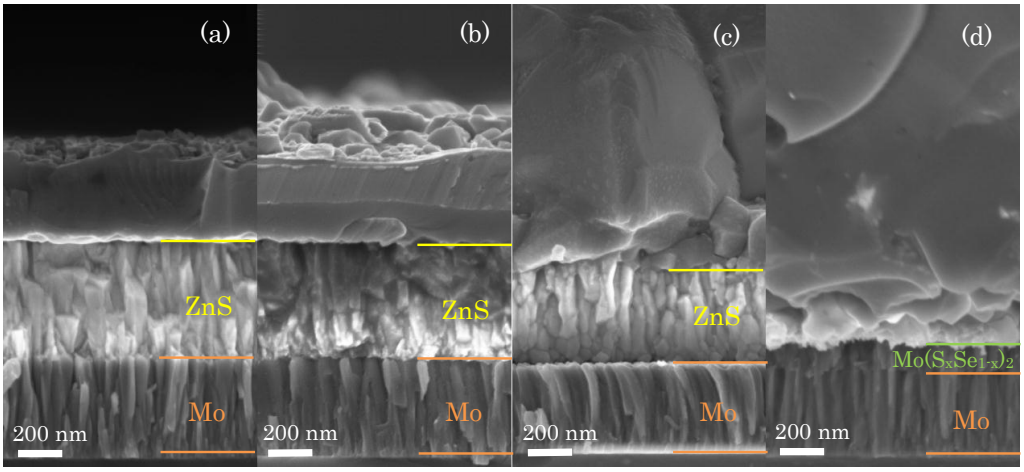

Figure 36: SEM images showing the formation of CZTSSe at different steps in the selenization process of Stack A: (a) after selenization at 350°C, (b) after selenization at 450°C, (c) after selenization at 570°C, (d) after selenization at 570°C with a 30 minute thermal plateau

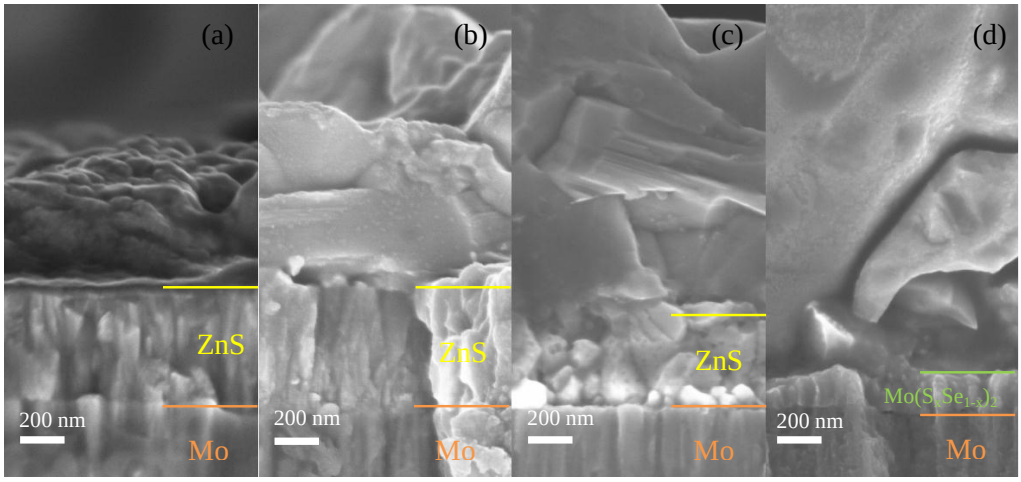

Figure 37: SEM images showing the formation of CZTSSe at different steps in the selenization process of Stack B: (a) after selenization at 350°C, (b) after selenization at 450°C, (c) after selenization at 570°C, (d) after selenization at 570°C with a 30 minute thermal plateau

After selenization at 570°C with a 30 min plateau (Figure 36-37d), the SEM image shows two distinguishable zones with large grains on top and smaller ones closer to the molybdenum interface. The larger grains are of the order of the layer thickness. In Figure 36-37d a thin layer of $Mo(S,Se)_2$ can also be observed which is in accordance with literature [22]: it is especially recognizable due to its typical columnar shape.

4.3.2 Study of the selenization process by EDS

EDS measurements are performed to evaluate compositional changes in the material with increasing temperature during the process of selenization (Figure 38 and 39).

The incorporation of Se into stack A increases with temperature: at 350°C no Se is observed (Figure 38a and 39a), indicating that evaporated Se needs higher temperatures to facilitate diffusion into the top Cu layer. At 450°C, the Se content increases with annealing temperature (Figure 38b), and at 570°C the CZTSSe stoichiometry for chalcogens is reached (([S]+[Se])/Metals~1) (Figure 39a). The 30 min plateau does not change the [S]/([S]+[Se]) ratio or the chalcogen:metal ratio (Figure 39a). The formation of a high Zn and Se content phase (probably Zn(S,Se)) in contact with Mo is noted (Figure 38c).

In stack B, selenium incorporation is larger at lower temperatures (350°C) than the one in stack A evidenced by the presence of high Sn and Se content phases (probably SnSe) in the top layer (Figure 38b) and a much lower [S]/([S]+[Se]) ratio at 350°C and 450°C (Figure 39b). This result indicates that the low-temperature incorporation of Se in the thin film is greatly enhanced when the Sn layer is in contact with the Se vapor. As in stack A, a phase with high content of Zn and Se (probably Zn(S,Se)) is still present at the Mo interface after the 30 min temperature plateau (Figure 38d).

It is also noted that at every annealing temperature before the 30 min plateau (350°C, 450°C, and 570°C) the [S]/([S]+[Se]) ratio is much lower for stack B than for stack A (Figure 39). This demonstrates that the incorporation of Se *in loco* of S atoms is easier in stack B than in stack A.

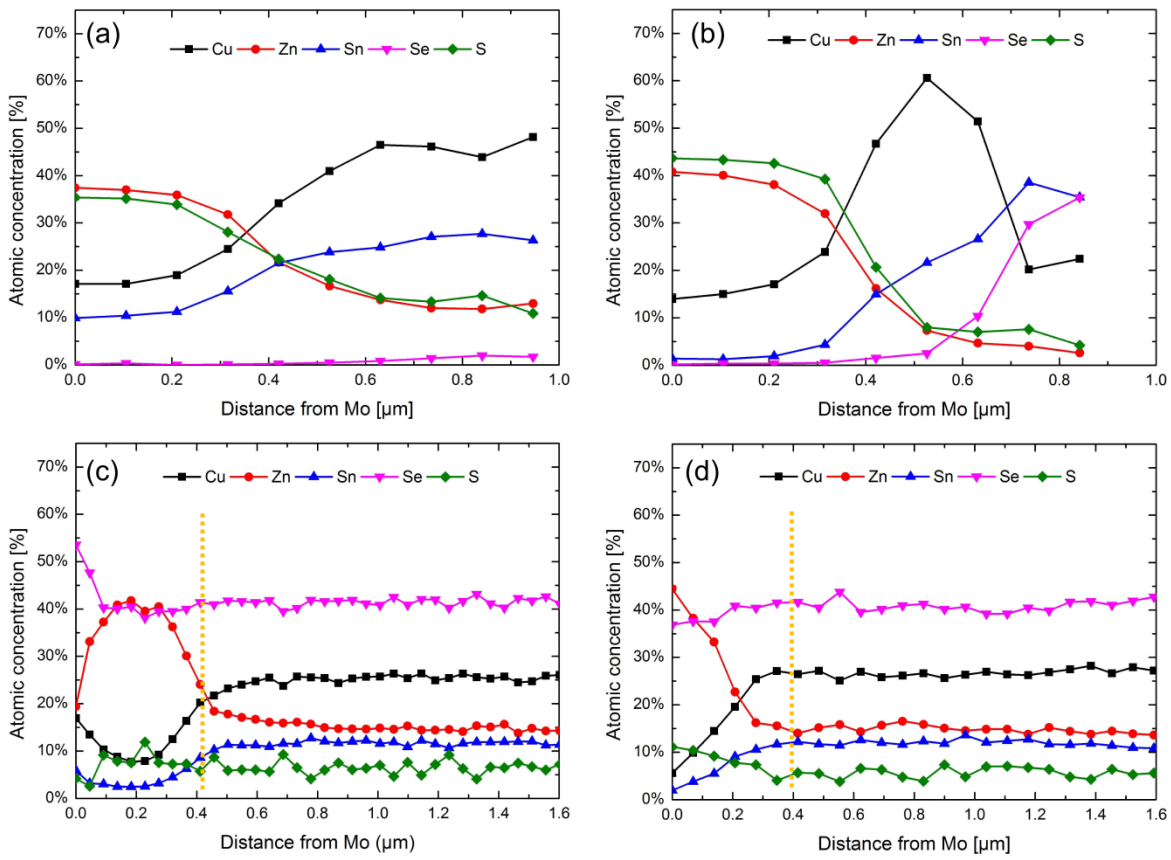

Figure 38: Cross-section EDS profiles of stack A selenized at 350°C (a) and 570°C – 30min (c); cross-section EDS profiles of stack B selenized at 350°C b) and 570°C – 30min (d). All statistical errors are twice the confidence limit. The yellow line in each image is the starting point for the calculation of [Zn]/[Sn], [Cu]/([Zn]+[Sn]) and [S]/([S]+[Se]) ratios shown in Table 2. The Zn-rich phase on the left of the black line is discarded in the composition calculations

The evaluation of the metal ratios [Zn]/[Sn] and [Cu]/([Zn]+[Sn]) in CZTSSe layers is a critical point since improved performance in solar cells has been attributed to a Cu-poor and Zn-rich absorber layers. Top-view EDS measurements at 25kV, at the end of the 30 min plateau, give [Zn]/[Sn]=1.31 and [Cu]/([Zn]+[Sn])=0.76 for stack A, [Zn]/[Sn]=1.35 and [Cu]/([Zn]+[Sn])= 0.72 for stack B. These atomic ratios are calculated over the whole wafer, thereby including the high Zn-content phase in contact with Mo. The [Zn]/[Sn] ratio decreases and the [Cu]/([Zn]+[Sn]) ratio increases by discarding the high Zn-content phase at the Mo interface. This has been calculated from cross-section EDS measurements (see Figure 38c and 38d), showing that these ratios should be calculated with care in case of layer inhomogeneity. Independent of methodology (top-view EDS or cross-section EDS),

an alloy composition of (*1-x*) = 0.13±0.05 ([S]/([S]+[Se])) is found in both stacks after the 30 min plateau (results summarized in Table 2).

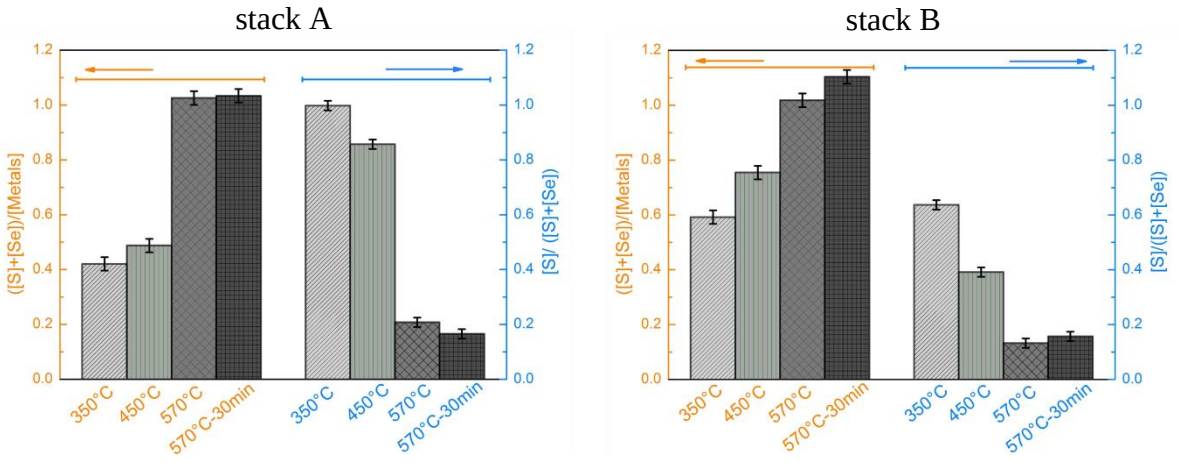

Figure 39: Compositional ratio at different steps of the selenization process of Stack A(a) and Stack B(b). Results are obtained from top-view from EDS measurements at 25kV. Values for the first steps have to be considered carefully because of the strong inhomogeneity of the layers.

Sample Name	EDS technique	[Zn]/[Sn]	[Cu]/([Zn]+[Sn])	[S]/([S]+[Se])
Stack A	Cross-section	1.26±0.03	0.97±0.02	0.13±0.03
	Top-view	1.31±0.06	0.76±0.06	0.13±0.05
Stack B	Cross-section	1.24±0.04	1.00±0.03	0.12±0.01
	Top-view	1.35±0.05	0.72±0.06	0.14±0.04

Table 2: Chemical composition of the thin films obtained from stack A and stack B, after selenization annealing at 570°C for 30 min. The atomic ratios are extracted from two types of energy dispersive spectroscopy measurements (cross-section and top-view, see the text for more details). The alloy composition (1-x) is given in the last column.

Using the chemical composition extracted from cross-section EDS measurements and reported in table 4, and using the molecular weight of each component, it is possible to calculate the CZTSSe density of stack A and B as function of the thickness. This density is reported in Figure 40 for both stacks: as noticeable it is around 5.75 g/cm^3 in the homogeneous part of the sample which is in accordance with the one (calculated at stoichiometry) reported in literature by Guen *et al.* [23].

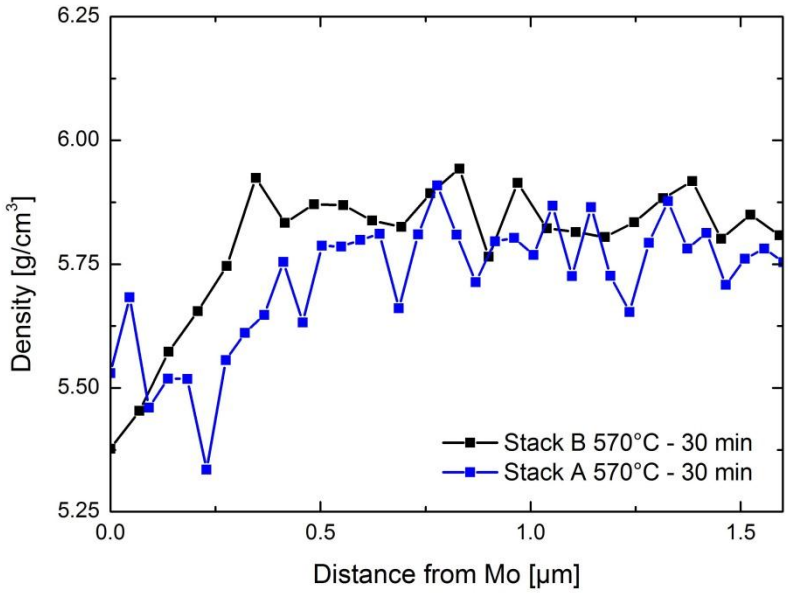

Figure 40: CZTSSe density of stack A and B at the end of selenization process

4.3.3 Study of the selenization process by Raman spectroscopy

Complementary to EDS which allows determining the chemical composition of the whole material, Raman spectroscopy is used to detect minority crystallographic phases in CZTSSe. The compositional dependence of Raman spectral features within $Cu_2ZnSn(S_{1-x}Se_x)_4$ with *x* values from 1 to 0 has already been studied by Grossberg *et al.* [24] showing a linear dependence of the A1 CZTSSe peaks to the alloy composition.

The Raman spectra of stack A selenized at different temperatures can be seen in Figure 41a. After selenization at 350°C a peak corresponding to SnS (190 cm^{-1}) can be seen [25], but there is no peak corresponding to Se-containing secondary phases. This indicates that the Se does not diffuse into the multilayer at this temperature and, is consistent with EDS results (Figure 36a). At 450°C a SnSe peak is noticeable (152 cm^{-1} [24]) and is attributed to Se diffusion into the stack and the onset of preliminary reactions with its components. At 570°C the wide 395-399 cm^{-1} peak cannot be unambiguously attributed to a definite chemical species.

Raman spectra at 570°C, with and without the 30 min plateau show the same profiles indicating the CZTSe peak (198 cm^{-1}) which could be assigned to the A1 mode of kesterite [24], and CZTS (327 cm^{-1} [26]). This is in good agreement with the bimodal behavior of the CZTSSe alloy already observed by Grossberg *et al.* [24]. The broad shoulder between 225 and 265 cm^{-1} comes most likely from minor phases in the material after the selenization process and the formation of the CZTSSe layer. The peak around 260 cm^{-1} could be attributed to the A1 peak of Cu_2Se [27] or to a Zn(S,Se) phase.

Raman spectra of stack B reveal a different behavior (Figure 41b). At 350°C, a SnSe peak (152 cm^{-1}) is observed, confirming that Sn reacts with Se to form SnSe, as suggested by EDS analysis (Fig. 38b). At 450°C a SnS peak is noticeable (187 cm^{-1} [25]) attributed to S diffusion from the ZnS layer towards the top of the stack. At 570°C the formation of

kesterite CZTSSe is evidenced by the Raman spectrum which shows the peaks of both CZTSe (201 cm^{-1} in Figure 41b) and CZTS (338 cm^{-1} in Figure 41b). The very sharp peak at 350 cm^{-1} is an artifact of the measurement and is not attributed to the sample. In contrast to stack A, the thermal plateau, namely a 30 minutes plateau at 570°C, is required in the case of stack B to get a well-defined material (notice the CZTSe peak sharpening between 570°C and 570°C-30 min).

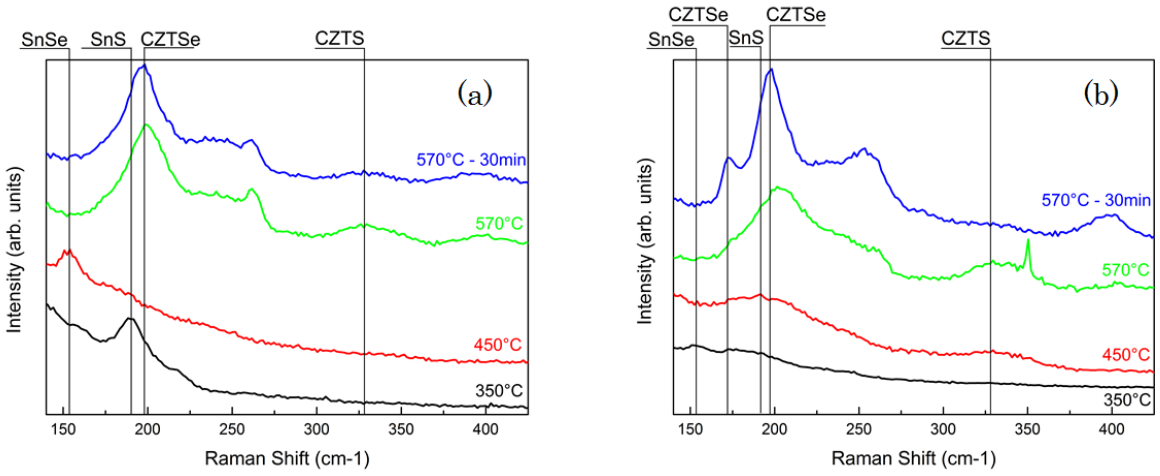

Figure 41: Raman spectra of the CZTSSe films at different temperatures for Stack A (a) and Stack B (b). The sharp peak at 355 cm-1 for CZTSSe spectrum at 570°C (green line in Stack B) is considered as an artifact of the measurement, and not indicative of the sample.

4.3.4 Study of the selenization process by GDS

The GDS spectra of stack A during selenization process can be seen in Figure 39. The spectra confirm that no Se has diffused layer after selenization at 350°C (Figure 39a) in accordance with EDS results (Figure 38-39a) and Raman spectra (Figure 38a). The diffusion of S through the Sn-layer (Figure 42a and 42b) can also be observed. After selenization at 450°C and 570°C (Figure 42b and 42c, respectively), the spectra indicate that Se-atoms have started to diffuse downwards. The GDS spectra at 570°C, with and without the thermal plateau (Figure 42d and 42c, respectively), exhibit similar behaviors and show an almost uniform distribution of elements. This result is in total agreement with Raman spectra (Figure 41a), and demonstrates that the final CZTSSe composition is achieved before the thermal plateau in the case of stack A.

Stack B GDS analysis (Figure 43) shows a different situation: the incorporation of Se has already started at low temperature (350°C) (Figure 43a). Its progressing can be seen at 450°C (Figure 43b), consistent with the EDS (Figure 38b and 39b) and Raman analysis (Figure 41b). Another important difference with stack A is that the distribution of elements is not uniform throughout layer prior to the thermal plateau (Figure 43c). After the plateau (Figure 43d), in the profile is very similar to that of stack A (Figure 42d), wherein the profiles for all elements are relatively constant throughout the material.

This analysis demonstrates that the 30 minute thermal plateau is required for CZTSSe compositional homogeneity in the case of stack B, but is not necessary for stack A.

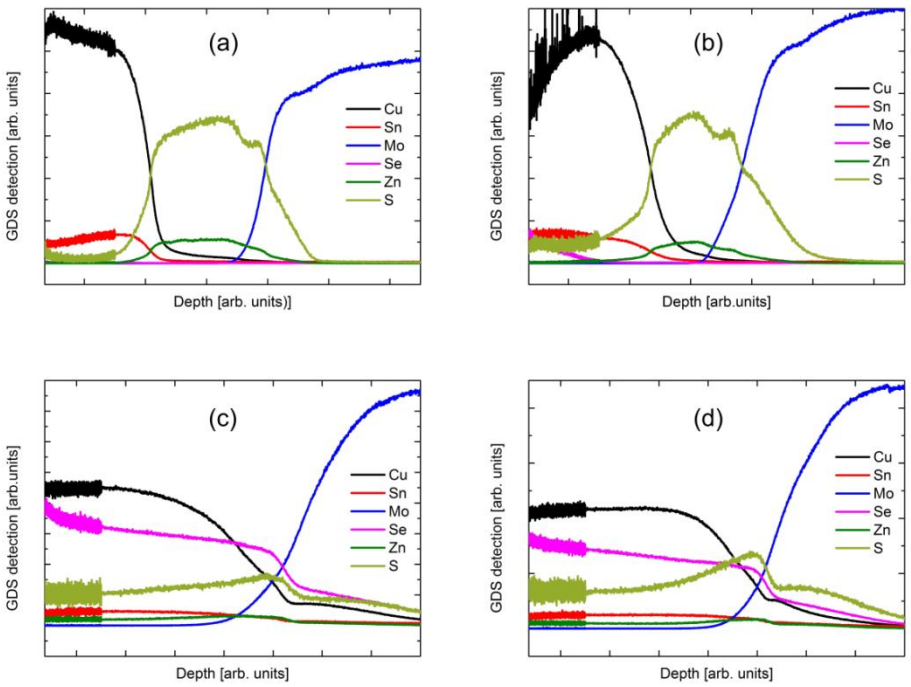

Figure 42: GDS spectra of Stack A: (a) 350°C, (b) 450°C, (c) 570°C, (d) 570°C - 30min

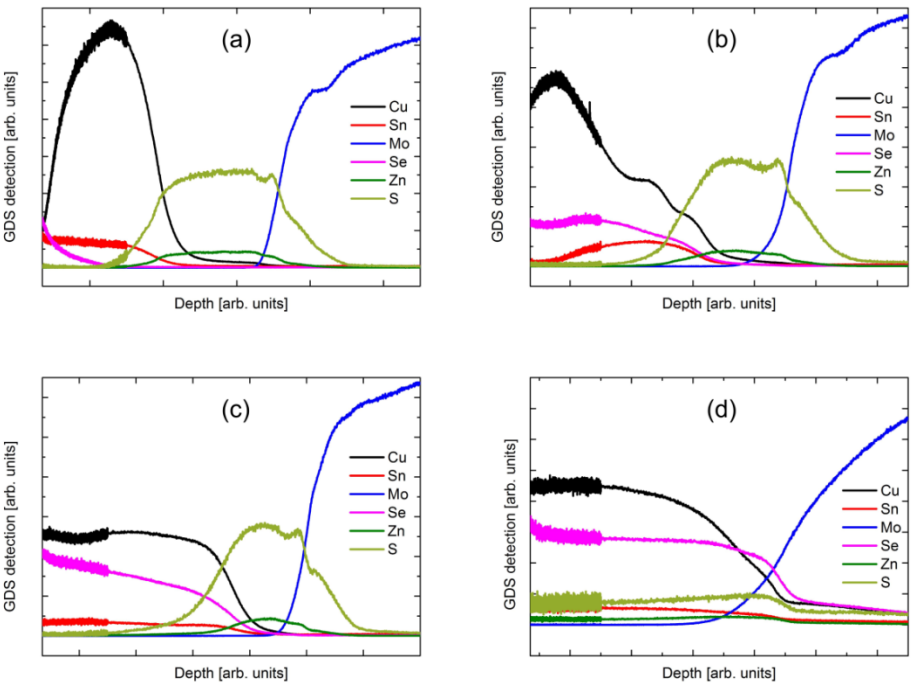

Figure 43: GDS spectra of Stack B: (a) 350°C, (b) 450°C, (c) 570°C, (d) 570°C - 30min

4.4 Minor phases at the end of selenization process

The experimental results show the importance, for the selenization process, of the position of the Sn and Cu layers in the precursor stack: for stack A (Cu on top) the Se incorporation is delayed; for stack B (Sn on top) where the Cu is directly in contact with the ZnS layer, the sulfur incorporation is the limiting process, and the annealing plateau at 570°C is necessary to obtain a homogenous material. In other words, it is found that the Cu layer inhibits the incorporation of chalcogens (selenium and sulfur) during the selenization process, as illustrated in Figure 44 which schematizes the mechanism. This result is of interest for potential industrial applications in order to optimize the synthesis duration.

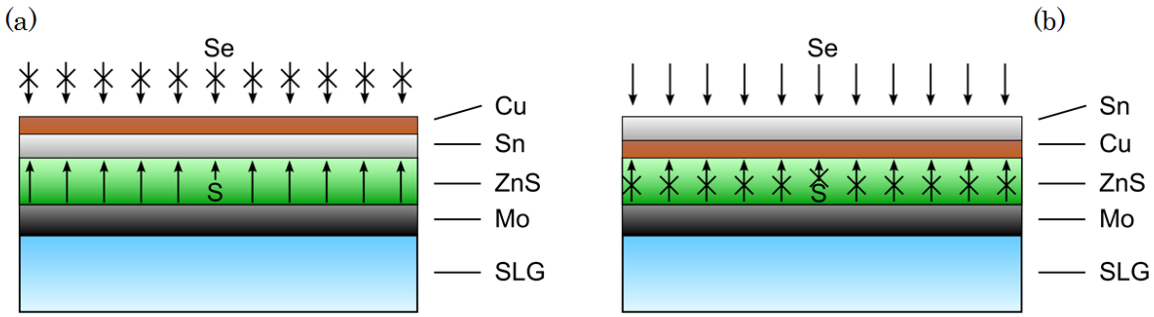

Figure 44: Model illustrating the strong interaction between Sn and chalcogens as compared to the one between chalcogens and Cu; this picture tends to explain qualitatively the different intermediate states which occur during the annealing process of stack A (a) and B (b).

In order to check the quality of the final CZTSSe absorber across its thickness at the end of selenization process, Raman microscopy is used on a beveled and polished samples of stack A and stack B. First, two samples of CZTSSe obtained from respectively stack A and stack B are beveled with an angle of one degree followed by mechanical polishing as for cross-sectional EDS described in 3.2.1.2.

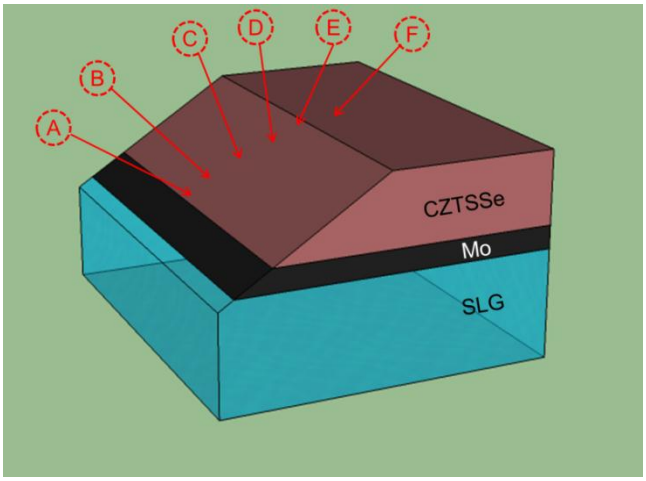

Figure 45: Model of the beveled and polished CZTSSe with an angle of 1 degree. The six points (A:F) represent the location point of Raman analysis.

The six points (A;F spaced every 20 µm) in Figure 45 represent the location where blue laser at a wavelength of 457 nm is hitting on the beveled samples for Raman analysis. The results are showed in Figure 46. The spectra in both cases show that at the end of the annealing process, no difference can be found between stack A and B at any point. At the same time, it is noticeable that at each point there is no shift of the CZTSe peaks (172, 197, 225 cm^{-1}) and CZTS peak (335 cm^{-1}) according to the bimodal behavior described by Grossberg *et al.* [24], confirming that there is no chalcogens gradient along the thickness of both samples as already seen by cross-sectional EDS (see 4.3.2). Moreover the variation of intensity of the A1 peaks is negligible thus highlighting the there is no variation of the quality of the material.
Moreover, the *"minor phase's region"* in each spectrum (230-260 cm^{-1} range) is not evolving along the thickness, meaning that in the end, the distribution of spurious phases in both samples is the same. The latter confirms that the CZTSSe layer is homogeneous all along its thickness.

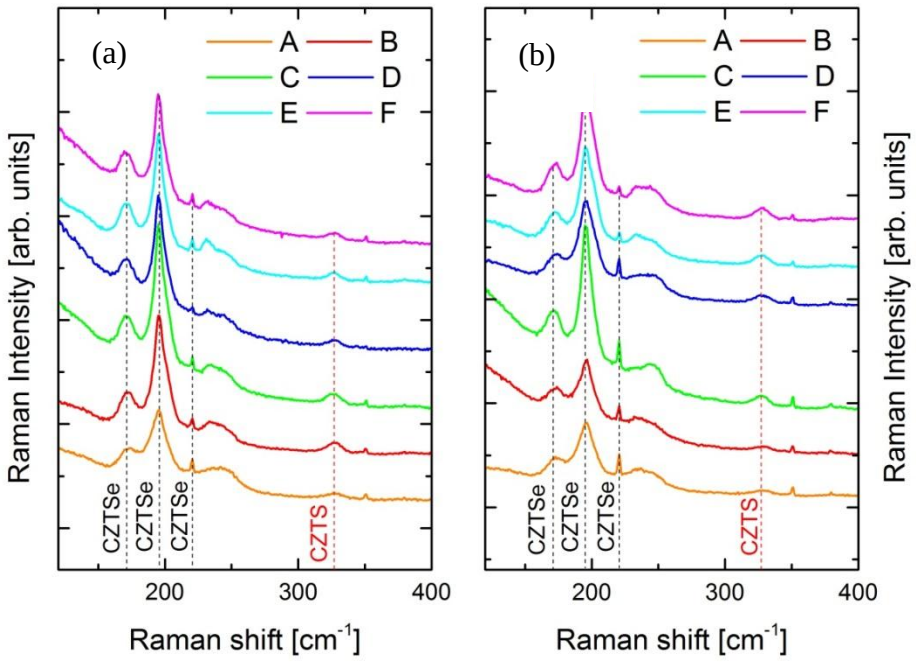

Figure 46: Raman spectra of beveled CZTSSe from stack A (a) and B (b).

4.5 Thermal considerations

In order to support the conclusion that Cu layer inhibits the incorporation of chalcogens during the selenization process as illustrated in Figure 44, some thermodynamic considerations on the formation of binary compounds are made by simulating the reactions of copper and tin with chalcogens:

(1) Sn + S ↔SnS
(2) Sn + Se ↔ SnSe
(3) Cu + S ↔ CuS
(4) Cu + Se ↔ CuSe

These simulations are run using FactSage 6.2 software [28] under the same conditions of temperature and pressure used in our experiments. Evaluation on the equilibrium constant $k = exp(-\Delta G/RT)$ (where ΔG is the Gibbs free energy of formation, $R=8.31\ J\ K^{-1}\ mol^{-1}$ is the ideal gas constant and T the temperature) for the four reactions proves that interactions between Sn and chalcogens (reactions (1) and (2)) are much more thermodynamically favorable. It is found that their equilibrium constants are five (at 350°C) and three (at 570°C) orders of magnitude larger than the ones of the cuprous reactions (reactions (3) and (4)). These thermodynamic data (indicating that the chalcogens react more easily with tin than with copper) are consistent with our experimental results which show a better incorporation of chalcogens when they are in direct contact with the Sn layer at the early stages of the selenization process (reactions (1) and (2) can occur). However they do not give any information about the diffusion of these chalcogens elements because no kinetic phenomena are taken into account within this approach.

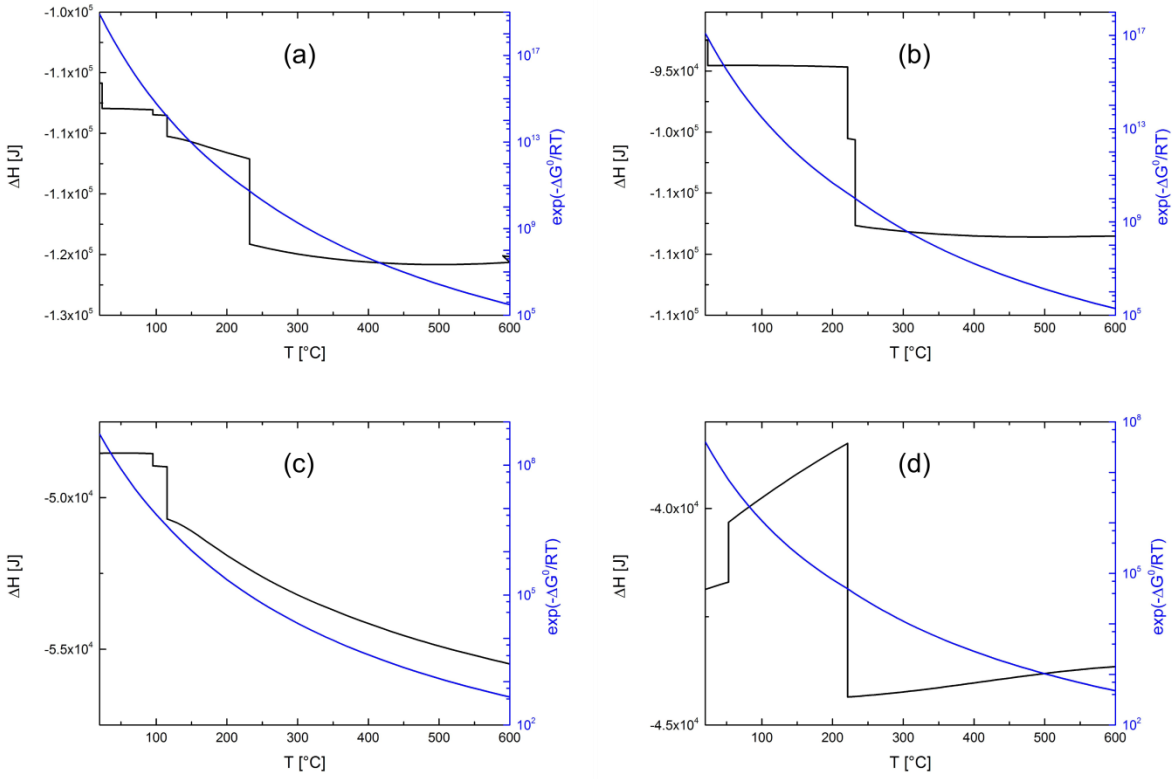

Figure 47: Thermodynamic simulations of the reactions of copper and tin with chalcogens: Sn + S ↔SnS (a), Sn + Se ↔SnSe (b), Cu + S ↔CuS (c), Cu + Se ↔CuSe (d). The ΔH is the enthalpy variation of the reaction.

4.6 $Cu_2ZnSn(S,Se)_4$ solar cells from different stack precursors

Another result is that at the end of the selenization process, the properties of the obtained CZTSSe solar cell are almost independent of the precursor stacking order. In order to validate the latter result from a device point of view, the CZTSSe thin films obtained by selenization at 570°C with a 30 minute thermal plateau for both stack A and stack B were integrated into photovoltaic devices. 18 SLG/Mo/CZTSSe/CdS/i-ZnO/ZnO:Al solar cells were fabricated and characterized for each stack (see Figure 48). We observe better short-circuit current density for stack A, and better open–circuit voltage for stack B. However, these differences are within the typical variations observed in our solar cell fabrication process. Similar efficiencies are obtained for both stacks, confirming that, after selenization, the CZTSSe photovoltaic performances are almost independent of the precursor stacking order.

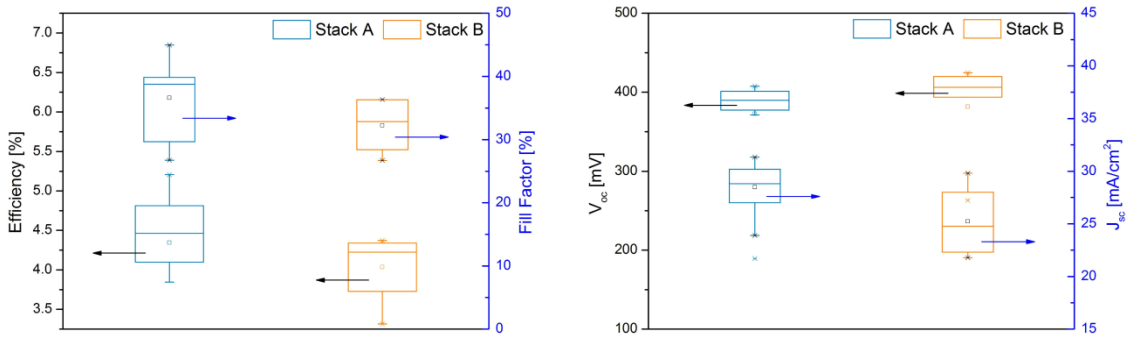

Figure 48: PV performances statistical study of 18 solar cells from different precursor stacks.

4.7 Conclusion

A study of the intermediate reactions during the selenization process for CZTSSe has been carried out. The results show the importance of the position of Sn and Cu in the precursor stack for the formation of intermediate phases before the formation of CZTSSe. The [S]/([S]+[Se]) ratio decreases with increasing temperature, since the Se is gradually replacing the S during the growth of the material. However, the Cu layer tends to prevent this substitution as well as the formation of a homogenous alloy by inhibiting the incorporation of chalcogens. Although the CZTSSe growth goes through different minor phases, in the end the composition of the film is relatively homogenous and almost independent of the precursor stacking order only after the complete process.

4.8 References

[1] W. Wang, M. T. Winkler, O. Gunawan, T. Gokmen, T. K. Todorov, Y. Zhu, D. B. Mitzi, Adv. Mater., doi: 10.1002/aenm.201301465

[2] S. Chen, X. G. Gong, A. Walsh, S. H. Wei, Applied Physics Letters 96 (2010), pp. 021902

[3] M. Mousel, A. Redinger, R. Djemour, M. Arasimowicz, N. Valle, P. Dale, S. Siebentritt, Thin Solid Films, 535 (2013), pp. 83-87
[4] G. Altamura, L. Grenet, C. Bougerol, E. Robin, D. Kohen, H. Fournier, A. Brioude, S. Perraud, H. Mariette, Journal of Alloys and Compounds 588 (2014), pp. 310–315
[5] A. Redinger, M. Mousel, M. H. Wolter, N. Valle, S. Siebentritt, Thin Solid Films 535 (2013), pp. 291-295
[6] J. J. Scragg, T. Ericson, T. Kubart, M. Edoff, C. Platzer-Björkman, Chemistry of Materials 23 (2011), pp. 4625-4633
[7] J. J. Scragg, P. J. Dale, D. Colombara, L. M. Peter, ChemPhysChem 13 (2012), pp. 3035-3046
[8] J. J. Scragg, T. Ericson, X. Fontané, V. Izquierdo-Roca, A. Pérez-Rodríguez, T. Kubart, M. Edoff, C. Platzer-Björkman, Prog. Photovolt: Res. Appl. 22 (2014), pp.10–17.
[9] A. Luque, S. Hegedus, Handbook of Photovoltaic Science and Engineering, Second Edition, Chapter 13, Wiley 2011.
[10] H. Katagiri, K. Jimbo, S. Yamada, T. Kamimura, W.S. Maw, T. Fukano, T. Ito,T. Motohiro, Proceedings of Photovoltaic Energy Conversion Conference 3 (2003).
[11] L. Grenet, S. Bernardi, D. Kohen, C. Lepoittevin, S. Noel, N. Karst, A. Brioude, S. Perraud, H. Mariette, Solar Energy Materials and Solar Cells 101 (2012), pp. 11-14.
[12] R.B.V. Chalapathy, Gwang Sun Jung, Byung Tae Ahn, Solar Energy Materials & Solar Cells 95 (2011), pp. 3216–3221.
[13] C. Platzer-Bjorkman, J. Scragg, H. Flammersberger, T. Kubart, M. Edoff, Solar Energy Materials & Solar Cells 98 (2012), pp. 110–117
[14] G. Brammertz, M. Buffiere, Y. Mevel, Y. Ren, A. E. Zaghi, N. Lenaers, Y. Mols, C. Koeble, J. Vleugels, M. Meuris, J. Poortmans, APPLIED PHYSICS LETTERS 102 (2013), pp. 013902
[15] S. W. Shin, S.M. Pawar, C. Y. Park, Jae Ho Yun, Jong-Ha Moon, Jin Hyeok Kim, Jeong Yong Lee, Solar Energy Materials & Solar Cells 95 (2011), pp. 3202–3206.
[16] T. Kato, H. Hiroi, N. Sakai, S. Muraoka, H. Sugimoto, 27th EPSEC, Frankfurt (2012)
[17] H. Hiroi, N. Sakai, T. Kato, H. Sugimoto, Proceedings of the IEEE Photovoltaic Specialists Conference 39th: 16–21 June 2013. Tampa (USA).
[18] H. Katagiri, N. Sasaguchi, S. Hando, S. Hoshino, J. Ohashi, T. Yokota, Solar Energy Materials & Solar Cells, 49 (1997), pp. 407-414.
[19] P. A. Fernandes, P. M. P. Salome, A. F. da Cunha, Semicond. Sci. Technol. 24 (2009), pp. 105013
[20] H. Yoo, J.H. Kim, Thin Solid Films 518 (2010), pp. 6567–6572.
[21] C.P. Norris, Surface Science Research, Nova Science Publishers Inc. (2005).
[22] K. Kim, K. Yoon, MoSe2 formation from selenization of Mo and nanoparticle derived Cu(In,Ga)Se2/Mo films, Photovoltaic Energy Conversion, Conference Record of the 2006 IEEE 4th World Conference 1 (2006) 506-508
[23] L. Guen, W.S. Glaunsinger, Journal of Solid State Chemistry 35 (1980), pp. 10.
[24] M. Grossberg, J. Krustok, J. Raudoja, K. Timmo, M. Altosaar, and T. Raadik, Thin Solid Films 519 (2010) 7403–7406.
[25] E. Khare, B.Himmetoglu, M. Johnson, D.J. Norris, M. Cococcioni, Journal of Applied Physics 111 (2012), 083707

[26] L. Sun, J. He, H. Kong, F. Yue, P. Yang, J. Chu, Solar Energy Materials and Solar Cells 95 (2011) 2907–2913.
[27] P.M.P. Salome, J.Malaquias, P.A.Fernandes, M.S.Ferreira, A.F.da Cunha, J.P. Leitao, J.C. Gonzalez, F.M. Matinaga, Solar Energy Materials & Solar Cells 101(2012) 147–153
[28] http://www.factsage.com/

Chapter 5

Sodium Incorporation

Outline

5.1 Motivation

In the case of CIGS solar cells, it is well known that the presence of sodium in the absorber layer is beneficial [1] and necessary to obtain high conversion efficiencies [2]. It mainly improves device performance through FF and V_{oc}; also hole density increases [3]. Although the exact action of Na on the structural and electronic properties of the absorber material is not clearly understood, defect passivation at the grain boundaries is nowadays the most considered explanation since it allows to have a favorable band alignment and so decrease recombination [4].

Due to the similarity between CIGS and CZTSSe technology, as for CIGS, Na may also play a critical role in CZTSSe. In literature, it is demonstrated that Na diffusion in CZTS affects grain size, crystal texture, and conductivity [5]. Different techniques have been applied to incorporate Na into the absorber in order to study its effect on the CZTSSe properties. Li *et al.* at NREL shows the beneficial effect of Na incorporation on V_{oc} and FF in CZTSe by evaporating 15 nm of NaF during CZTSe coevaporation [6]. Schwartz *et al.* reported, using atomic probe tomography, that Na segregates at CZTSe/ZnSe interfaces thus it could affect the formation and growth of the ZnSe domains in coevaporated CZTSe [7]. Li *et al.* reported also on the optical influence of Na in CZTS using Na-containing sol-gel precursors [8].

This chapter reports in details the characterization methods and experimental measurements on the CZTSSe layer grown with different Na-containing substrates, and electrical performances of solar cells built using the latter CZTSSe.

5.2 Substrates

5.2.1 Soda Lime Glass

The soda-lime glass is the most common type of glass for PV applications. SLG not only has the advantage of being made from inexpensive raw materials, but also the practical inconvenience of low working temperatures. It can be used in a wide range of scientific and industrial applications.

SLG employed in this study is 1 mm thick furnished by Goodfellow [9] with a 12 wt% NaOH.

5.2.2 Borosilicate Glass

Borosilicate glass is a type of glass that includes at least 5% boric oxide. The boric oxide makes the glass resistant to higher temperatures, and also improves its resistance to chemical corrosion. This glass is very popular in the manufacture of scientific instruments, and it was once widely used to make glass for PV applications as well.

BS employed in this study is 1 mm thick furnished by Corning [10] with a 1.8 wt% NaOH.

5.2.3 EAGLE2000 glass

EAGLE2000 glass is a lightweight alkaline earth boro-aluminosilicate glass with a low density and a low coefficient of thermal expansion. Corning's EAGLE2000 glass shows an even higher chemical durability. The high, broadband optical transmission and low light absorbance, in combination with the low mass of EAGLE2000, make it an ideal solution for many demanding optical applications.
EAGLE2000 employed in this study is 1 mm thick furnished by Praezisions Glas & Optik GmbH [11] with a 0.01 wt% NaOH.

5.2.4 Titanium

Ti is a lightweight and mechanically and chemically resistant metal. Furthermore, it has a good resistance at high temperature. Ti substrate is 99.6% Ti and contains very little harmful impurities (like iron) which could diffuse and modify the electronic properties of the materials deposited above it.
Ti employed in this study is 0.5 mm thick furnished by Goodfellow [9] and is totally sodium free.

5.3 Mo:Na back contact

A recent solution to better control the Na incorporation into CZTSSe is to directly incorporate a preset quantity of Na in the Mo back contact: it allows to get rid of the Mo barrier when the sodium is coming from the substrate. The doped layer thus formed is called Mo:Na. The latter is directly deposited by DC sputtering from a target of Mo:Na. It is developed using exactly the same type of equipment and process of a standard Mo back contact (see 3.1.1).

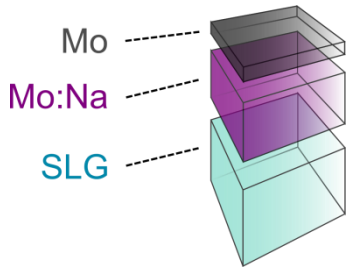

Figure 49: Back contact bilayer Mo:Na|Mo.

The development of Mo:Na layers is relatively recent: the first scientific papers on the subject dating from 2011 relating CIGS technology [12-13]. On the best of my knowledge, no studies are published about the synthesis of CZTSSe on Mo:Na back contact.
Bilayers MoNa (450nm)|Mo (100nm) are deposited using DC sputtering in the same equipment (Figure 49). The Mo-capping layer is used to avoid the incorporation of damp in the MoNa layer and improve the electrical resistance of the BC. The MoNa is deposited from a sputtering target composed of Mo:Na containing 5% sodium (atomic percentage) in

the form of sodium molybdate Na_2MoO_4. The composition of 5% sodium was chosen because it is one that seems to lead to better performance, according to a study made on CIGS by Blösch *et al.* [14].

5.4 CZTSSe synthesized on different substrates

CZTSSe material is synthesized on Mo-coated different substrates (SLG, BS, VSS and Ti) by two step selenization process as described in 3.1.3. Two studies are performed: (i) material and device characterization are performed in order to find a relationship between sodium incorporation in CZTSSe and its material properties for absorbers synthesized on SLG and BS, (ii) Mo:Na back contact is evaluated by comparison of PV characteristics between CZTSSe solar cell with Mo and Mo:Na BC on different substrates (SLG, BS, VSS, Ti).

5.5 CZTSSe characterization

5.5.1 Sodium concentration

The measurement of sodium concentrations as a function of depth in CZTSSe synthesized on various substrates is accomplished using Secondary Ion Mass Spectrometry because of its very low detection limits and excellent depth resolution. Because the secondary ion yields of sodium under the SIMS measurement are dependent upon the matrix composition of the CZTSSe, the quantification of this measurement requires the use of appropriate reference materials. In this case the reference material is a CZTSSe absorber which is grown on titanium (sodium-free substrate) and then bombarded with a known concentration of Na-ions. The Na-SIMS profile extracted from the latter will be the reference to quantify sodium concentration in the CZTSSe by using spectrum comparison.
The key to quantification in dynamic SIMS is the Relative Sensitivity Factor (RSF), which provides the conversion from measured secondary ion intensities to impurity density. RSF is a function of the element of interest and the sample matrix.

5.5.1.1 Sodium implantation

Ion implantation is the technique employed to introduce Na into the CZTSSe synthesized on Ti (sodium-free substrate) in order to have a reference spectrum. It consists of introducing charged atoms into a material, by delivering to them sufficient energy so that they enter beyond the surface area of the absorber. The main advantage of sodium implantation is the precise control of the number and of the penetration depth of the Na-ions. The dose indicates the number of ions implanted per unit of surface of the target (given in atoms/cm^2) and the energy of ions (in keV) is the parameter controlling the spatial distribution of the atoms.

5.5.1.2 Sodium incorporation in CZTSSe

SIMS depth profiles reveal varying Na concentrations inside the absorbers (dashed line in Figure 50). The lower Na concentrations were found in BS in a range between 10^{17}-10^{18} atoms/cm^3, whereas for SLG the Na concentration is larger than 10^{19} atoms/cm^3. It is noticeable as well that in both samples the concentration of Na into CZTSSe is higher close to the Mo interface where the Zn content is higher. This increase in Zn concentration is related to a Zn(S,Se) phase, as demonstrated in Chapter 4, which itself could be related to the higher Na concentration in this region, as suggested by Schwarz *et al.* [7].

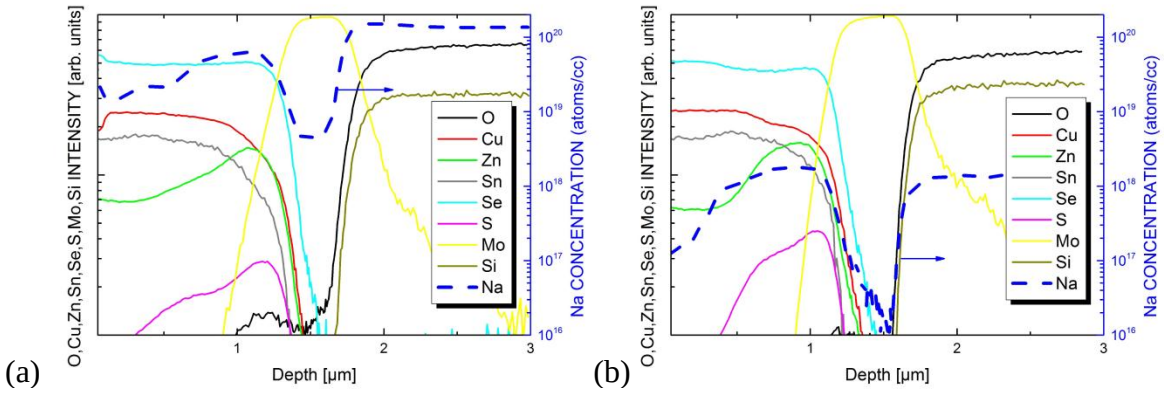

Figure 50: Na concentration measured by SIMS for CZTSSe on different Mo-coated SLG (a) and BS (b). O, Cu, Zn, Sn, Se, S, Mo, Si concentrations are in arbitrary units.

In order to evaluate of a possible relationship between the Zn(S,Se) phase formation and the Na diffusion, CZTSSe is synthesized by the usual method (see 3.1.3) with a different ZnS precursor thickness (inset Figure 51).

In Figure 51 is reported the SIMS profile measurement of CZTSSe after selenization of precursor stacks with different ZnS thickness. The results show that the Na signal is more intense in correspondence of the amplification of the Zn and S signals. This could drive to the idea that Na segregation in the bottom of CZTSSe absorber could be somehow involved in the growth of Zn(S,Se) phases.

The benefits and drawbacks of Na for CZTSSe solar cells have to be further elucidated in future studies. Moreover further comparative studies of Na-containing and Na-free samples must be planned for the future in order to unravel the relationship between Na and Zn-rich phase segregation.

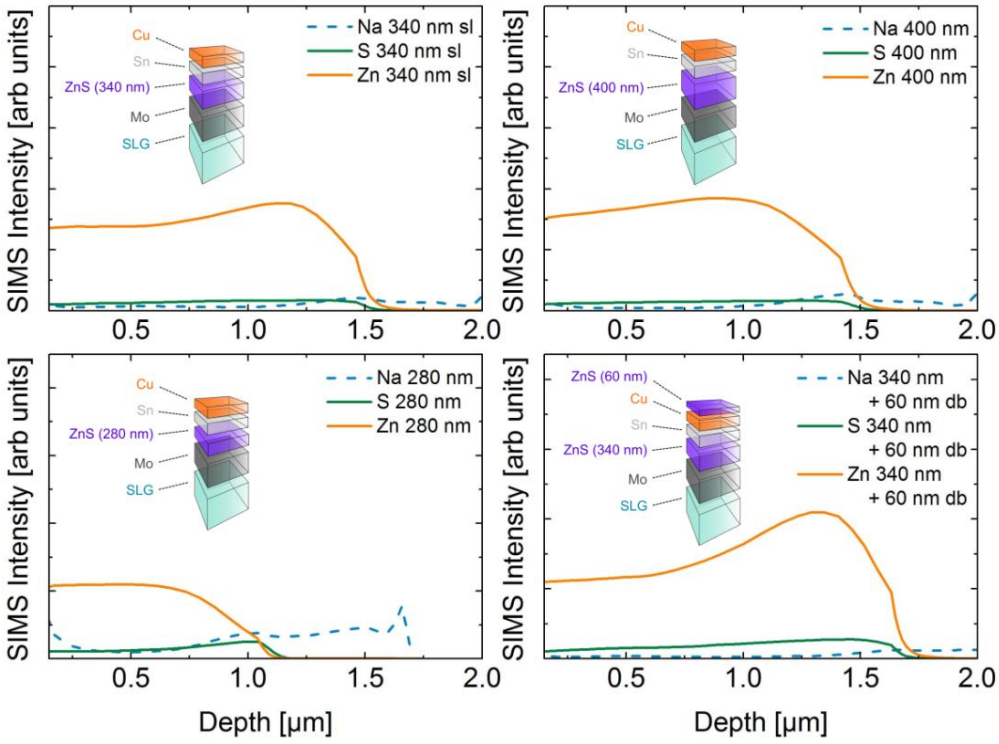

Figure 51: SIMS profile measurement on CZTSSe starting from different ZnS precursor thickness. Schematic of the precursor stack prior to selenization process with different ZnS thicknesses are shown in the insets: 340 nm (a), 400 nm (b), 280 nm (c), 340 + 60 nm double layer (d).

5.5.2 Grains size dependency on Na-content

X-ray diffractions of CZTSSe on SLG and BS are shown in Figure 52. The films were found to be polycrystalline and having two prominent reflections (112) and (220) recorded respectively at a Bragg angle of 27.325° and 47.636°. Using the Scherer's formula (see 3.2.1.2) the crystallite dimension of the two samples is calculated: the results, exposed in Table 1, show that in the case of SLG glass, the size of the crystallite was calculated to be 43 nm, whereas in the borosilicate glass case the mean crystallite dimension was only 34 nm. This shows that there is a significant increase in the size when the CZTSSe is synthesized on substrates containing higher Na-content as confirmed Prabhakar *et al.* [5].

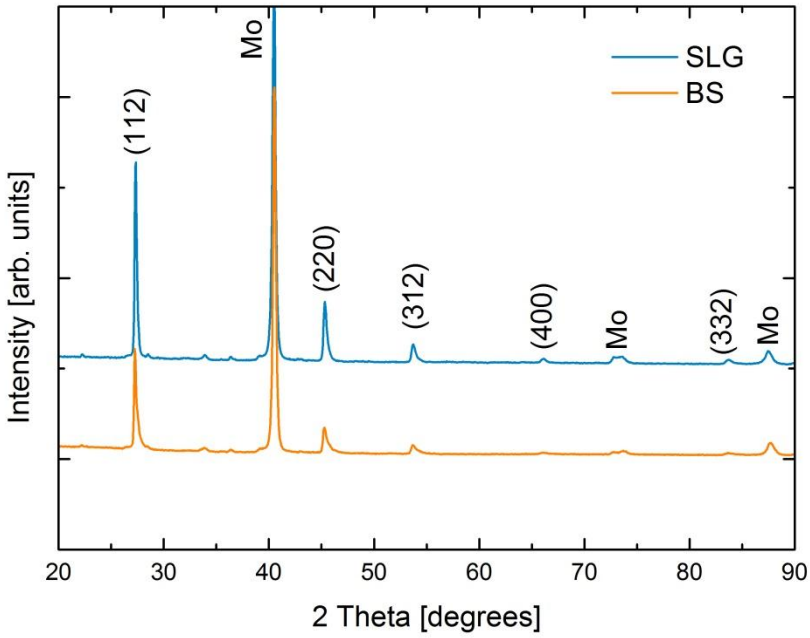

Figure 52: XRD spectra for CZTSSe on different Mo-coated glasses.

Sample	Position	FWHM	Crystallite size (nm)
SLG	27.325	0.2122	42.854
BS	27.299	0.2712	33.627

Table 1: The calculated crystallite size using the Scherer's formula.

Cross-sectional SEM images of the CZTSSe grains synthesized on SLG (a) and BS (b) are also reported in Figure 53. They show that bigger grains and less voids are present in CZTSSe synthesized on SLG, confirming that the latter has better quality compared to CZTSSe grown on BS.

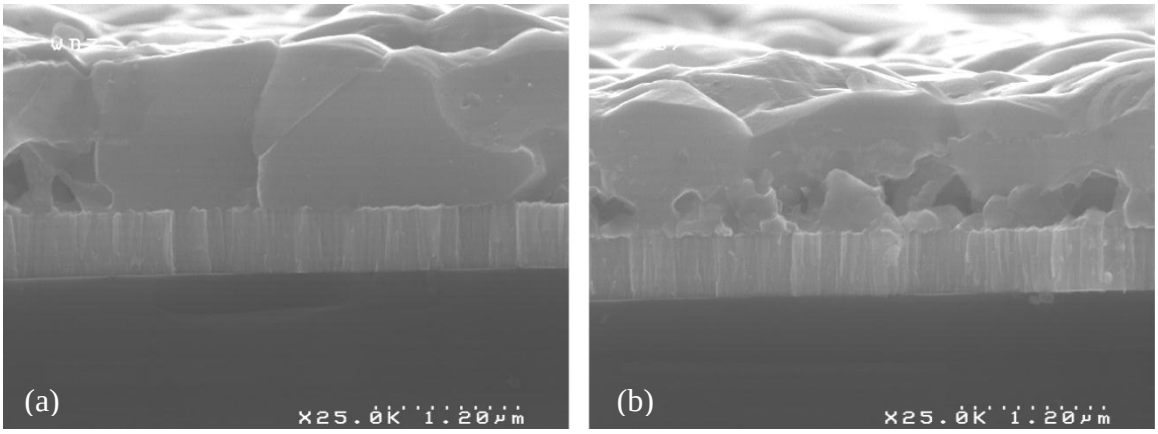

Figure 53: SEM images showing the CZTSSe synthesized on Mo-coated: (a) SLG (high Na-content), (b) BS (low Na-content).

5.5.3 Minor phases dependency on Na-content

Raman spectra for both samples are acquired in backscattering configuration with a 10 mW/cm^2 532 nm green laser excitation. The Raman spectra of SLG and BS depicted in Figure 54 show that the A1 CZTSe peak (198 cm^{-1}) and A1 CZTS peak (326 cm^{-1}) of SLG are more pronounced compared to the ones of BS (respectively at 194 cm^{-1} and 323 cm^{-1}). The latter concept is validated when computing FWHM of the A1 CZTSe peaks for the two spectra: $FWHM_{SLG} = 70$ vs $FWHMS_{BS} = 100$.

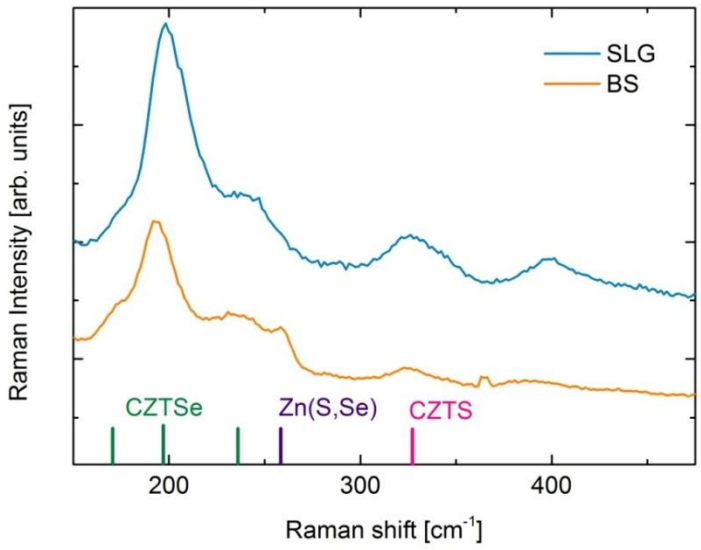

Figure 54: Raman spectra for CZTSSe on different Mo-coated glasses.

Since the CZTSSe Raman intensities are usually related to the concentration of a given phase, it is possible to identify CZTSSe with higher Na concentration (SLG) as a material with better quality than CZTSSe with a lower Na content. Secondary CZTSe peaks (237 cm^{-1} in SLG and 230 cm^{-1} in BS) together with a Zn(S,Se) peak (259 cm^{-1} in BS) are also detected.

5.5.4 CZTSSe quality dependency on Na-content

The PL spectra of the SLG and BS samples measured at T=7 °K are presented in Figure 55. The excitation power density was 818 mW/cm^2. For both SLG and BS, the spectra are relatively complex with emission occurring at several distinct peak wavelengths (Figure 55). Although the two spectra show the same features (the main luminescence peak occurs at 0.955 eV), the measurements performed in the present study indicate that the PL intensity of SLG is much more intense than the BS one, where the Na concentration is almost two orders of magnitude lower. This reflects the influence of Na, which improves the radiative over non-radiative recombination rates.

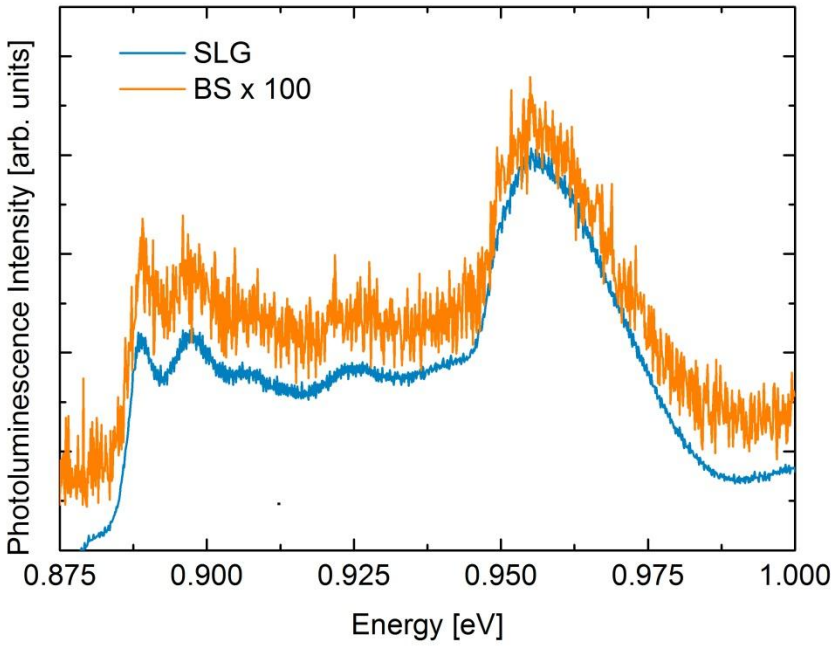

Figure 55: PL spectra for CZTSSe on different Mo-coated glasses.

5.6 $Cu_2ZnSn(S,Se)_4$ solar cells on different Na-content substrates

After material characterizations CZTSSe absorbers grown on different substrates are employed in full PV devices: at least twenty 0.25 cm^2 solar cells have been fabricated and

electrically characterized for each CZTSSe|substrate combination. Light J-V characteristics are depicted for all the cells in Figure 56 showing that photovoltaic performances increase along with the Na content in CZTSSe.

The median power conversion efficiency in the case of SLG is higher than BS and the dispersion of results is smaller. The variation of PCE between cells build on different substrates is clearly dominated by the variation of the FF and V_{oc}. Both V_{oc} and J_{sc} are higher in the case of SLG: in particular V_{oc} gain is remarkable with an absolute gain of 83 mV among the respectively highest values. As demonstrated in CIGS technology, Na incorporation into absorber could increase the p-doping of the material: there are no confirmations that this is also the case for CZTSSe, but if positive this could be one reason for the augmentation of the V_{oc}.

Possible implications of parasitic resistances in the FF are evaluated through dark J-V measurement. Figure 57 discloses series resistance, shunt resistance, dark saturation current, and ideality factor extracted from dark J-V characteristics. In the case of SLG, median R_s is higher in the case of BS, whereas R_{sh} is comparable in two cases. Actually the J_0 median value seems to be slightly higher in the case of BS, which could also explain why there is a lost in V_{oc} in the latter although almost the same shunt resistance is detected in both samples. The ideality factor in the case of SLG is lower than BS: this means that the recombination rate is lower in the case of CZTSSe synthesized on SLG. This result is in agreement with the radiative over non-radiative recombination ratio deduced from PL.

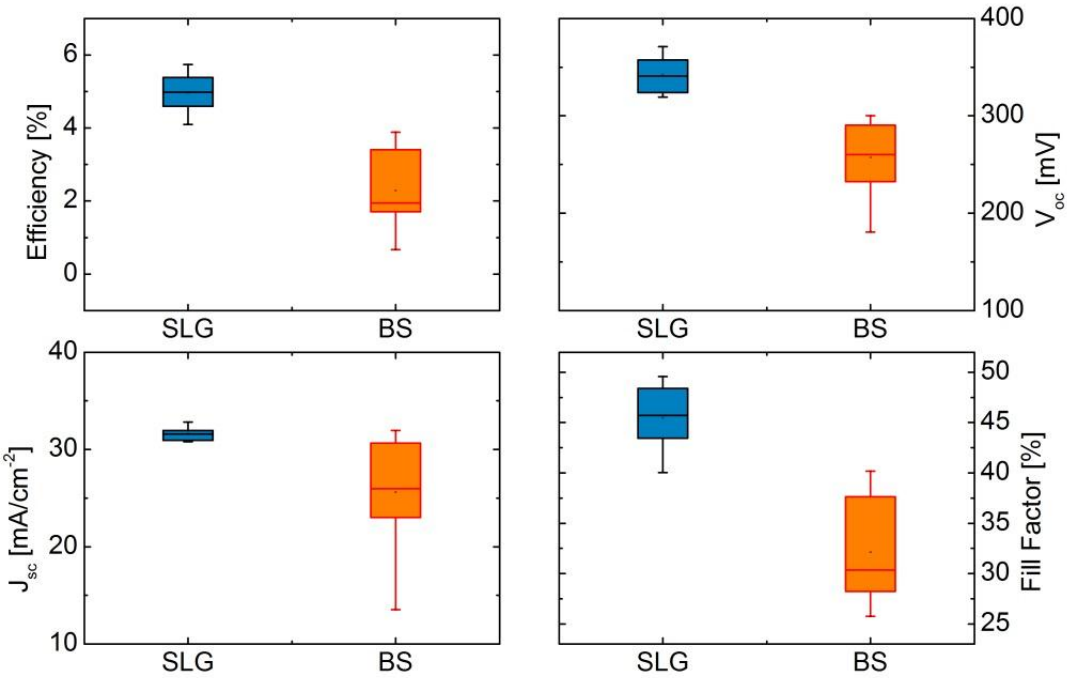

Figure 56: Current-voltage measurements under illumination (simulated AM1.5 spectrum, 100 mW/cm²) of Al:ZnO/i-ZnO/CdS/CZTSSe/Mo solar cells synthesized on SLG (blue boxes) and BS (orange boxes).

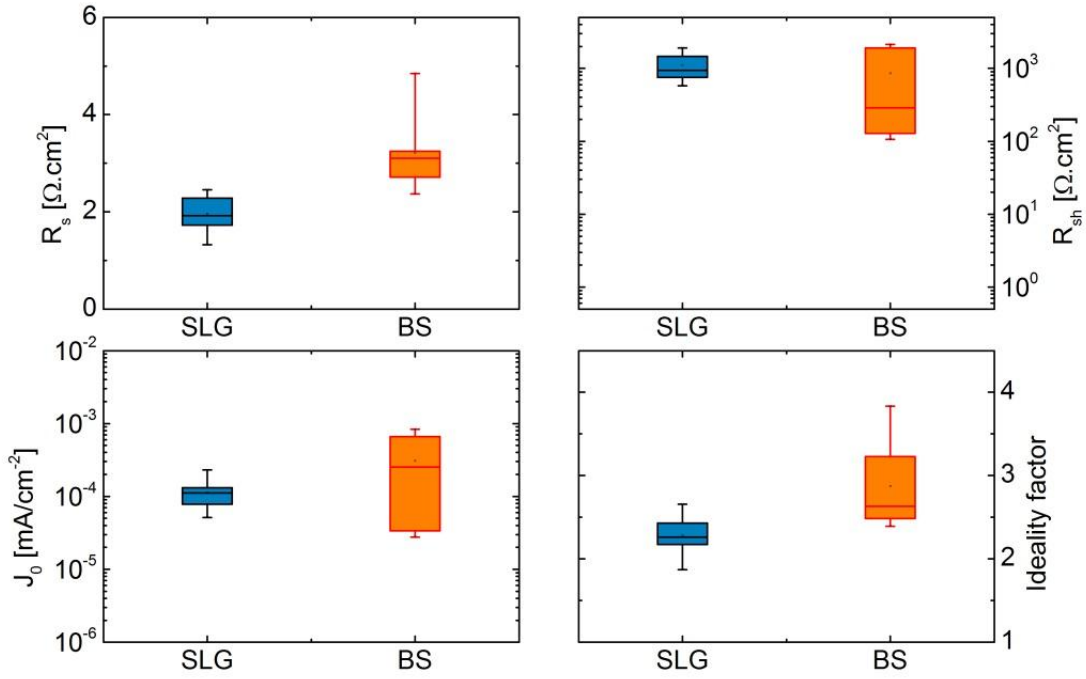

Figure 57: Dark current-voltage measurements of Al:ZnO/i-ZnO/CdS/CZTSSe/Mo cells synthesized on SLG (blue boxes) and BS (orange boxes).

5.7 $Cu_2ZnSn(S,Se)_4$ solar cells with Mo:Na back contact

In literature, Mo:Na back contact is reported to be a good compromise to provide sodium in CIGS solar cell when the absorber is synthesized on Na-free substrates like stainless steel [16] and titanium [17].

The influence of replacing a standard Mo back contact with a Mo:Na one (details on this material are given in 5.3) in CZTSSe solar cell is evaluated. In order to perform this study, different substrates have been used: SLG, BS, VSS and Ti: the Na-content in those substrates goes from 12% to 0%. Figure 58 shows the PV performances of CZTSSe solar cell with a Mo:Na back contact, whereas Figure 59 shows the PV performances with a standard Mo back contact.

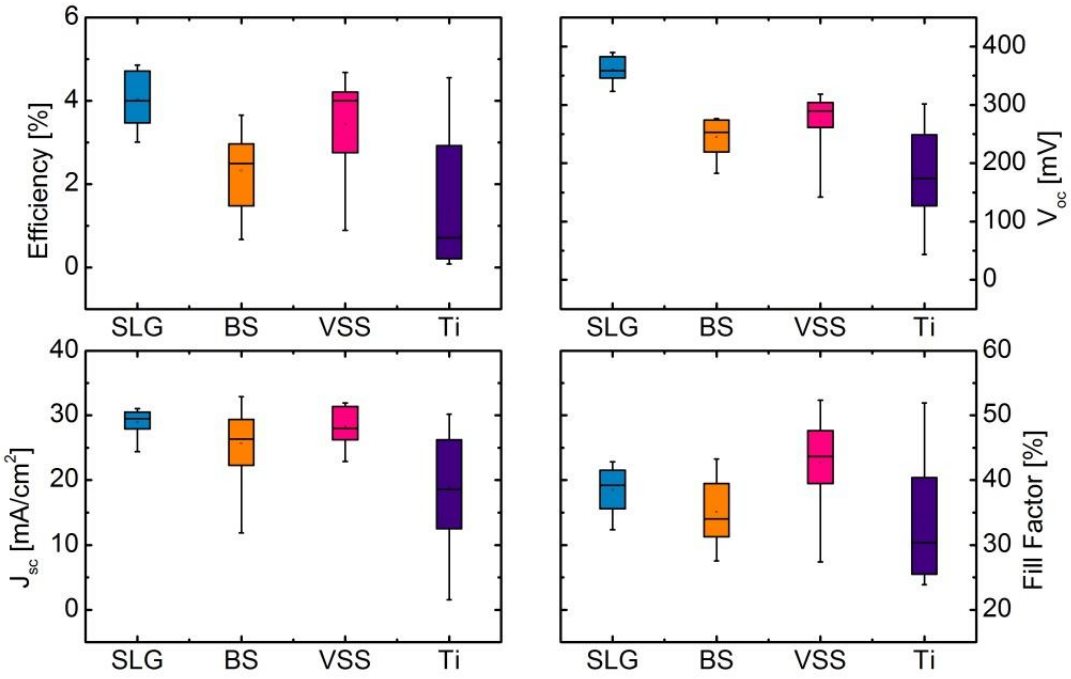

Figure 58: Light current-voltage measurements of Al:ZnO/i-ZnO/CdS/CZTSSe/Mo/Mo:Na cells synthesized on SLG (blue boxes), BS (orange boxes), VSS (fuchsia) and Ti (violet).

A comparison between the two back contacts highlights the fact that two situations are distinguishable: *(i)* the SLG and BS case, *(ii)* the VSS and Ti case.
In *(i)* it is noticeable that PV performances are higher for SLG and commensurable for BS when a Mo back contact is employed. Two possible reasons are foreseen at the origin of this behavior: the first one could be that further sodium contribution does not improve PV performances in CZTSSe. It has already been demonstrated in the case of CIGS solar cells that PV performances increase along with Na incorporation until a certain threshold before start decreasing [18]: this could also be the case for CZTSSe technology. The second one could be related to the high resistance of the Mo:Na back contact [17] which could dominate over the benefits brought by sodium. Roger *et al.* demonstrated that the resistance of the Mo:Na is high enough to overcome the one of the TCO, giving as a result a higher series resistance in the related photovoltaic cell [17].
In *(ii)* it is noticeable how PV performances increase when a Mo:Na back contact is used. Since both VSS and Ti are almost Na-free, the benefits of sodium incorporation in CZTSSe are evident and lead to an improvement of electrical characteristics.

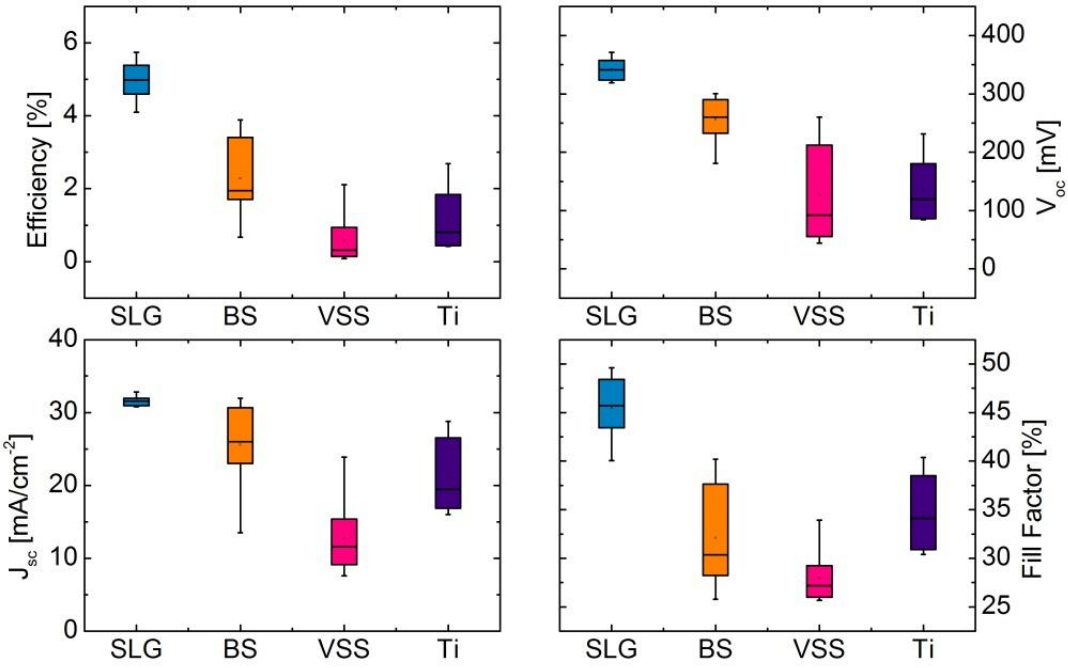

Figure 59: Light current-voltage measurements of Al:ZnO/i-ZnO/CdS/CZTSSe/Mo cells synthesized on SLG (blue boxes), BS (orange boxes), VSS (fuchsia) and Ti (violet).

At the end of this comparison study, a hypothesis rises up: the sodium supply in CZTSSe solar cell, as for CIGS technology, is useful to boost PV performances only until a certain value included in between 5% and 12%. This value is not precisely accessible because of: *(i)* the high influence of the Mo:Na back contact resistance, *(ii)* the possible implication of Na incorporation at the doping level. Further characterizations are needed in order to confirm these assumptions.

5.8 Conclusion

The effects of different Mo-coated Na-content substrates on the electro-optical properties of CZTSSe are addressed. This is done through characterization of the finished devices using XRD, Raman spectroscopy, photoluminescence and J-V characteristics. The SIMS analysis shows that relatively high concentration of Na is found in CZTSSe grown on SLG compared to CZTSSe grown on BS. Results indicate the beneficial effect of Na, evidenced by increases in the photovoltaic performances (above all open-circuit voltage and efficiency) and PL intensity.

5.9 References

[1] A. Chirila, S. Buecheler, F. Pianezzi, P. Bloesch, C. Gretener, A. R. Uhl, C. Fella, L. Kranz, J. Perrenoud, S. Seyrling, R. Verma, S. Nishiwaki, Y. E. Romanyuk, G. Bilger, A. N. Tiwari, Nature Materials 10 (2011), pp. 857–861.
[2] K. Granath, M. Bodega, L. Stolt, Solar Energy Materials, 60 (2000), pp. 279-293.
[3] R. J. Matson, J. E. Granata, S. E. Asher, M. R. Young, AIP Conference Proceedings, no. October (1999), pp. 542-552.
[4] R. Caballero, C.A. Kaufmann, T. Eisenbarth, M. Cancela, R. Hesse, T. Unold, A. Eicke, R. Klenk, H.W. Schock, Thin Solid Films, 517 (2009), pp. 2187-2190.
[5] T. Prabhakar, N. Jampana, Sol. Energy Mater. Sol. Cells 95 (2011), pp. 1001.
[6] J. Li, D. Kuciauskas, M. Young, I. Repins, Appl. Phys. Lett. 102 (2013), pp. 163905
[7] T. Schwarz, O. Cojocaru-Mirédin, P. Choi, M. Mousel, A. Redinger, S. Siebentritt, D. Raabe, Applied Physics Letters 102 (2013), pp. 042101
[8] Y. Li, Q. Han, T. Kim, W. Shi, J Sol-Gel Sci Technol 69 (2014), pp. 260–265
[9] http://www.goodfellow-ceramics.com/
[10] http://www.corning.com/
[11] http://www.pgo-online.com/
[12] L. Mansfield, I. Repins, J. Pankow, M. Young, C.Dehart, R. Sundaramoorthy, C. Beall, B. To, M. Carducci, D. Honecker, Proceedings of the 37th IEEE Photovoltaic Specialists Conference (PVSC 37) Seattle, Washington, July2011.
[13] R. Wuerz, A. Eicke, F. Kessler, P. Rogin, and O. Yazdani-Assl, Thin Solid Films, 519 (2011), pp. 7268–7271.
[14] P. Blosch, F. Pianezzi, A. ChirilaÌ†, P. Rossbach, S. Nishiwaki, S. Buecheler, A. Tiwari, Journal of Applied Physics, 113 (2013), pp. 054506.
[15] G. Altamura, L. Grenet, C. Bougerol, E. Robin, D. Kohen, H. Fournier, A. Brioude, S. Perraud, H. Mariette, Journal of Alloys and Compounds 588 (2014), pp. 310–315
[16] Y. Hashimoto, T. Satoh, S. Shimakawa, T. Negami, Proceedings of 3rd World Conference on Photovoltaic Energy Conversion 1 (2003), pp. 574 - 577.
[17] C. Roger, G. Altamura, F. Emieux, O. Sicardy, F. Roux, R. Fillon, P. Faucherand, N. Karst, H. Fournier, L. Grenet, F. Ducroquet, A. Brioude, S. Perraud, Journal of Renewable and Sustainable Energy, 6 (2014), pp. 011405.
[18] P. Blösch, S. Nishiwaki, A. Chirilă, L. Kranz, C. Fella, F. Pianezzi, C. Adelhelm, E. Franzke, S. Buecheler, A. N. Tiwari, Thin Solid Films, 535 (2013), pp. 214-219

Chapter 6

New back contact in $Cu_2ZnSn(S,Se)_4$ solar cells

Outline

6.1 Motivation

In most of the publications dealing with CZTSSe thin films for PV applications, the structure of the solar cell is directly copied from those used in CIGS technology: Al:ZnO/i-ZnO/CdS/CIGS/Mo [1-2] in which CZTSSe is replacing CIGS [3-4]. Especially, Mo is used as back contact (BC), but this choice has not been optimized yet for CZTSSe.

The properties of the BC have a strong impact on the solar cell performances. Patel *et al.* [5] simulated numerically the current-voltage characteristics of a Al:ZnO/i-ZnO/CdS/CZTSSe/BC solar cell trying to find the optimum BC material and CZTSSe layer thickness which gives the best cell performances. SCAPS software simulations of CZTSSe solar cells with different BC [6] showed that solar cell performances are improved by increasing the BC work function. According to these simulations, Mo is not the best BC in terms of power conversion efficiency. On the other hand, Scragg *et al.* [7] suggested reexamining the choice of molybdenum due to a phase-segregation at CZTSSe|Mo interface during annealing.

Those results have motivated the work described in this chapter in which we have studied experimentally the effects of different back contacts on the performances of CZTSSe solar cells. In this study several metals (Au, W, Pd, Pt, Ni) have been deposited on top of a Mo thin film in order to study: *(i)* the possibility of synthesizing CZTSSe on different BC, *(ii)* the interaction of the BC with the chalcogens during the selenization process, *(iii)* the influence of the BC on Al:ZnO/i-ZnO/CdS/CZTSSe/BC/Mo solar cell performances.

The choice of these metals as possible replacement for Mo is directly derived from the results published in Ref. 6: in fact all of them have a metal work function which is higher than the one of Mo (5 eV) which allow contemplating a better efficiency of the CZTSSe solar cell. Moreover, gold is already employed in CIGS technology due: to its high reflectance it allows the photon recycling increasing the photovoltaic performances.

6.2 Back contact deposition

Two different techniques are used to deposit 100 nm-thick BC on Mo-coated SLG: W and Au are deposited via DC-sputtering at room temperature, while Pd, Pt and Ni are deposited by high vacuum electron-beam evaporation. In both cases deposition rates are controlled by a quartz balance. It should be noted that in this study, the 100-nm-thick BC (Au, W, Pt, Pd, Ni) is deposited on top of a 450-nm-thick Mo layer (Figure 60).

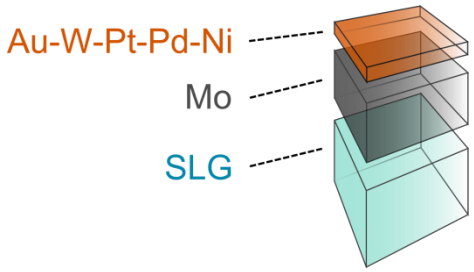

Figure 60: Back contact bilayer.

There are three reasons to keep an underlying Mo layer: *(i)* some metals like for example Pd and Pt do not have a good adhesion on soda-lime glass, *(ii)* we assume that Mo may play a role of barrier for contaminants from glass (in order to be more confident that the CZTSSe performances do not suffer from excess of contamination, we prefer to have the same diffusion barrier), *(iii)* in the context of low-cost solar cells like CZTSSe-based ones, the interest of an alternative back contact may only exist if the new back contact is not expensive; due to the cost of the metals used in this work (except W), it could be of interest to add a thin interfacial layer between Mo and CZTSSe but not to replace the 450-nm-thick Mo layer.

6.3 CZTSSe synthesized on different back contacts

CZTSSe material is synthesized on different back contacts by two step selenization process as described in 3.1.3.

6.3.1 Study of the selenization process by GDS

Figure 61 shows GDS spectra of CZTSSe synthesized on different BCs. Palladium and nickel (CZTSSe|Pd and CZTSSe|Ni in Figure 61e and 61f, respectively) diffuse into the CZTSSe reaching the surface of the sample.

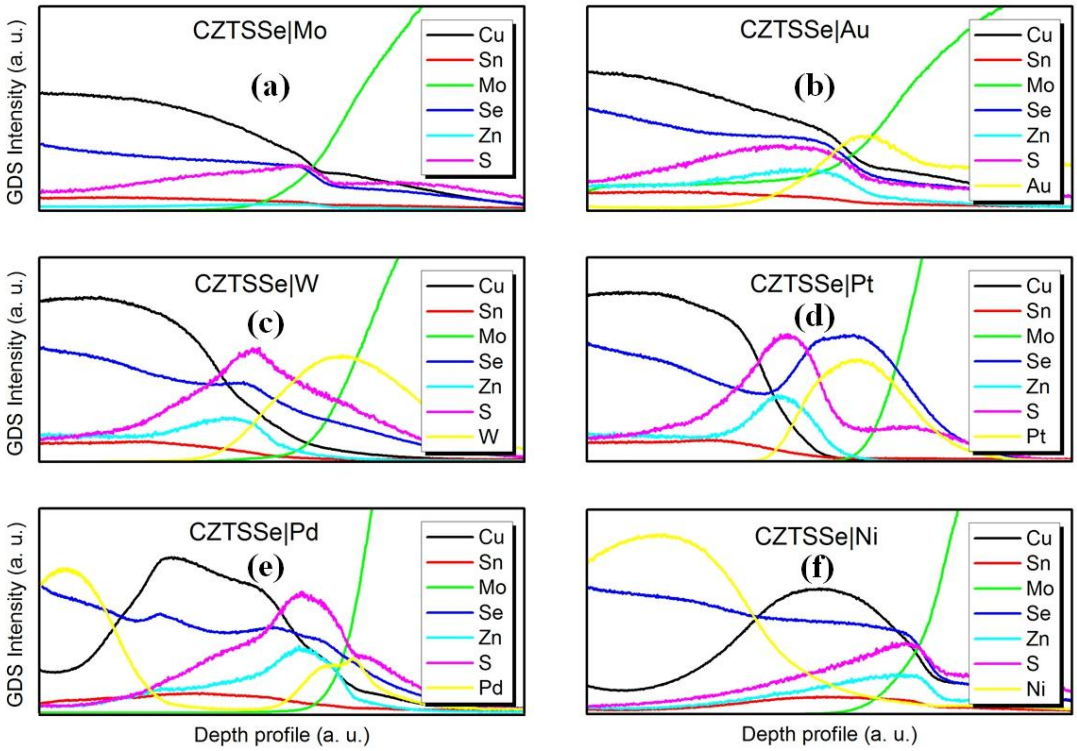

Figure 61: GDS spectra of CZTSSe synthesized on Mo (CZTSSe|Mo) (a), Au (CZTSSe|Au) (b), W (CZTSSe|W) (c), Pt (CZTSSe|Pt) (d), Pd (CZTSSe|Pd) (e), Ni (CZTSSe|Ni) (f).

The diffusion of Ni through the absorber layer has been already noticed also for CIGS solar cells [8]. On the contrary Au, W and Pt remain in contact with Mo. In the case of Au (CZTSSe|Au in Figure 61b), the Mo signal is not equal to zero far from the BC: this is simply due to the presence of voids in the CZTSSe layer at the measured point. In the case of W (CZTSSe|W in Figure 61c) we can see an important superposition of W with S and Se profiles. Finally for Pt (CZTSSe|Pt), there is a clear superposition of the Pt and Se profiles (Figure 61d).
Hereinafter only characterization made on CZTSSe on Au, W and Pt are presented since it has been demonstrated that CZTSSe grown on Pd and Ni is not of interest due to their diffusion towards the surface.

6.3.2 Study of the selenization process by XRD

Figure 62 shows the diffraction spectra of CZTSSe grown on Au, W and Pt. The CZTSSe patterns [9] are recognizable by the main reflections at 22.0°, 27.2°, 33.8°, 45.1° and 53.5° which are visible in all the spectra; the reflection of Mo is at 40.2° and 87.4° [9].

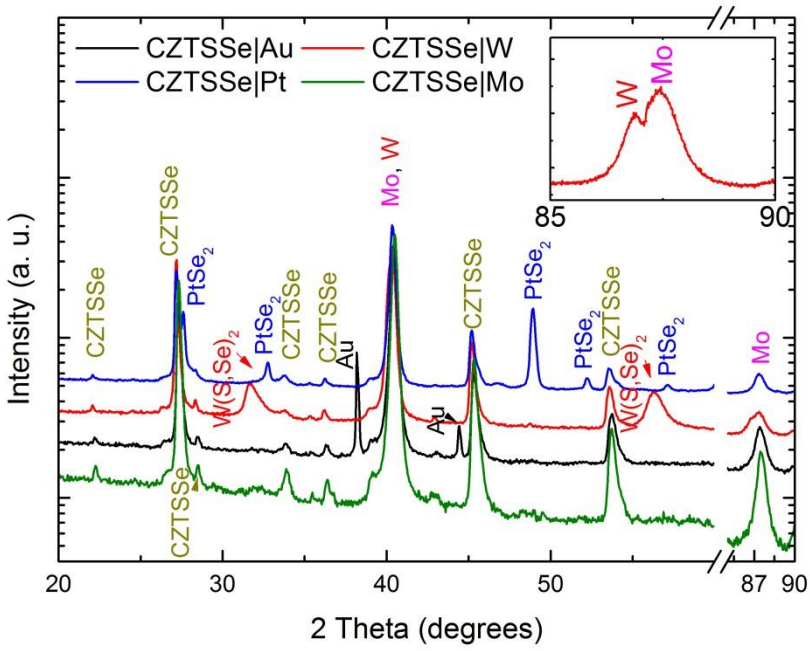

Figure 62: XRD patterns of CZTSSe synthesized on Mo (CZTSSe|Mo), Au (CZTSSe|Au), W (CZTSSe|W), Pt (CZTSSe|Pt). Patterns are shifted vertically and the x-axis is cut between 60 and 85 degrees for clarity. The inset shows a zoom on CZTSSe|W in the range 85-90 degrees.

In the case of CZTSSe on Au (CZTSSe|Au), the Au peaks at 38.2° and 44.6° are visible. It should be noted that no gold-chalcogens phases are detected pointing the fact that Au BC has not reacted with neither S nor Se during the selenization process. In the case of

CZTSSe on W (CZTSSe|W), the W reflection at 39.9° [10] overlaps with the Mo one since they have almost the same lattice constants but at higher diffraction angles it is possible to distinguish W (86.9°) from Mo (87.4°) (inset in Figure 62) which proves that metallic W is still present. Moreover $W(S,Se)_2$ peaks are present respectively at 32.0° and 56.5° [11] indicating the W has reacted with sulfur and selenium, which is consistent with the GDS spectrum (see the overlap of W, S and Se profiles in Figure 61c). Finally for CZTSSe on Pt, the reflections at 32.8° and 48.6° are signatures of the $PtSe_2$ phase [9]; again, this is consistent with the GDS spectrum (see the overlap of Pt and Se profiles in fig. 61d). No peaks of metallic Pt are visible.
To sum up, XRD analysis discloses that: *(i)* Au does not react with chalcogens, *(ii)* W reacts but not completely, *(iii)* Pt completely reacts with selenium.

6.3.3 Study of the selenization process by Raman

Figure 63 shows Raman analysis made on CZTSSe grown on Mo (Figure 63a), Au (Figure 63b), W (Figure 63c) and Pt (Figure 63d). Raman spectra of CZTSSe|Au and CZTSSe|W show the same profiles indicating both the peak of CZTSe at 197 cm^{-1} which could be assigned to the A1 mode of kesterite [12], and the peak of CZTS at 329 cm^{-1} [13]. This is in good agreement with the bimodal behavior of the CZTSSe alloy [14].

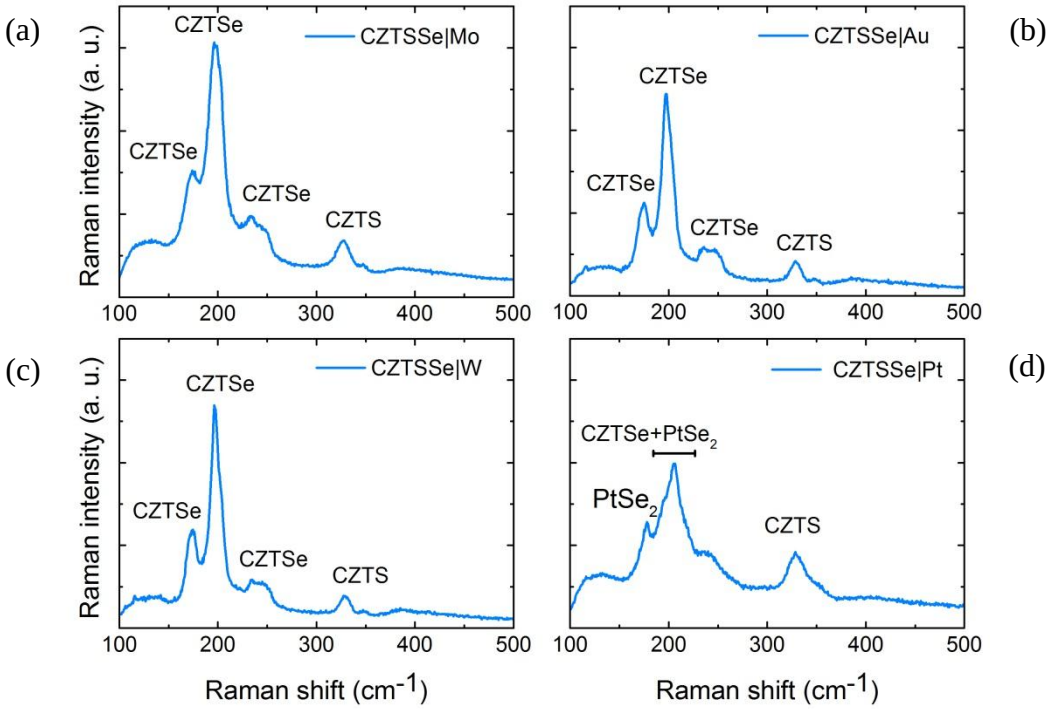

Figure 63: Raman spectra of CZTSSe synthesized on Mo (CZTSSe|Mo) (top-left), Au (CZTSSe|Au) (top-right), W (CZTSSe|W) (bottom-left), Pt (CZTSSe|Pt) (bottom-right). The inset in the bottom-right of Fig. 61d shows the Raman spectrum of $PtSe_2$.

Other signatures of CZTSe are present in the range of 174-176 cm^{-1} and 234-236 cm^{-1} [13]. In the case of CZTSSe|Pt, the spectrum is more complicated with broader CZTSSe related peaks and additional ones.
As no Raman spectrum of $PtSe_2$ is found in the literature, a 100-nm-thick layer of Pt has been selenized in the same way as CZTSSe (see 3.1.3) and then characterized by XRD confirming the formation of a single phase of $PtSe_2$ (Figure 64).

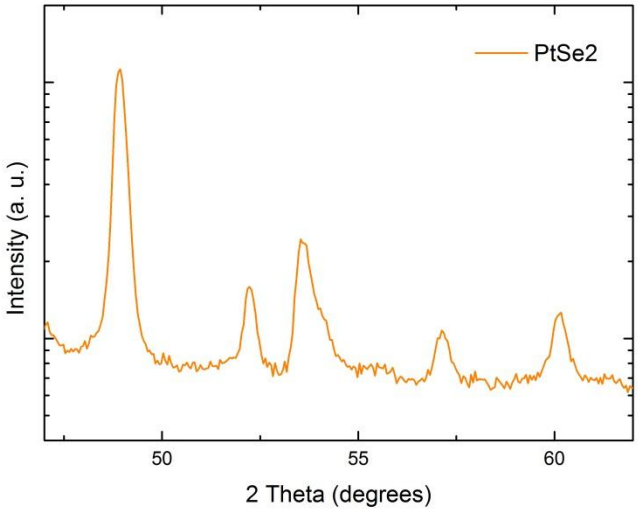

Figure 64: XRD patterns of $PtSe_2$.

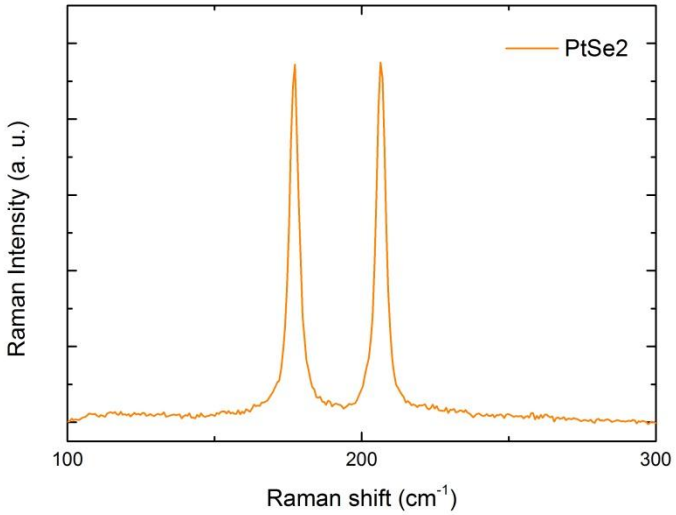

Figure 65: Raman spectrum of $PtSe_2$.

Then Raman spectrum of this pure $PtSe_2$ sample is acquired and used to further characterize CZTSSe|Pt (Figure 65). It is noticeable in the Raman spectra that the peaks at 205 cm^{-1} and 177 cm^{-1} are signatures of $PtSe_2$. The kesterite peaks of CZTSe and CZTS are also visible (at 195 cm^{-1} and 328 cm^{-1}, respectively) but with a widening of their own signal, which is an indication of a low crystallographic quality. $PtSe_2$ is visible although the CZTSSe layer should absorb the laser signal since many voids are present at the surface as observed in SEM (Figure 66).

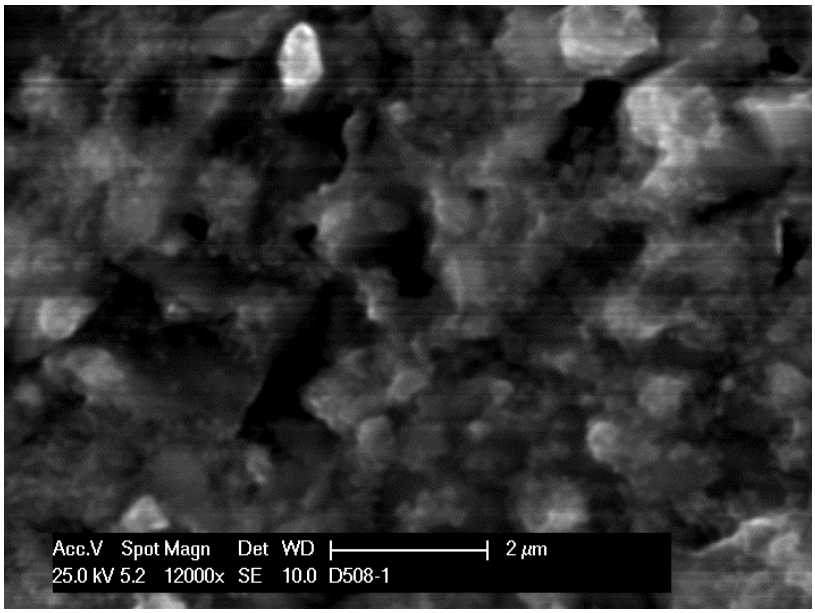

Figure 66: Top-view SEM image of CZTSSe|Pt.

6.3.4 Study of the selenization process by SEM

SEM cross-section images of CZTSSe|Au, CZTSSe|W and CZTSSe|Pt samples are shown in Figure 67. For the CZTSSe|Au sample (Figure 67a), the 1.1 µm thick CZTSSe layer is apparently in direct contact with the Mo and the 100 nm layer of gold is not visible after selenization process. But it is also noticed on the SEM images that, in some zones where the CZTSSe layer is detached from Mo layer, particles with a diameter around 270 nm appear (inset in Figure 67a). These particles are identified as gold by cross-sectional EDS (shown further in 6.5.2). During the selenization process, the 100 nm–thick gold layer is dewetted to form gold particles on the bottom of the absorber with an estimated mean distance of 350 nm among them. This dewetting occurs during the annealing process since it was a uniform layer after precursor deposition as confirmed by SEM images. This Au dewetting process allows Mo to be exposed to the incoming Se during annealing thus forming a thin layer of $MoSe_2$. CZTSSe|W SEM image (Figure 67b) shows a 1.1 µm-thick CZTSSe layer and a 350 nm-thick layer detected on the top of Mo: according to the results obtained by GDS and XRD, part of it could be assigned to a $W/W(S,Se)_2$ phase. In the case of the CZTSSe|Pt sample (Figure 67c), according to the previous characterizations, the

layer detected on the top of Mo is assigned to $PtSe_2$; as for CZTSSe|W, big CZTSSe grains are visible. Noteworthy are, in the three cases (Figure 67), the small grains at the interface between CZTSSe and BC. These small grains have been attributed to a Zn-rich phase [15].

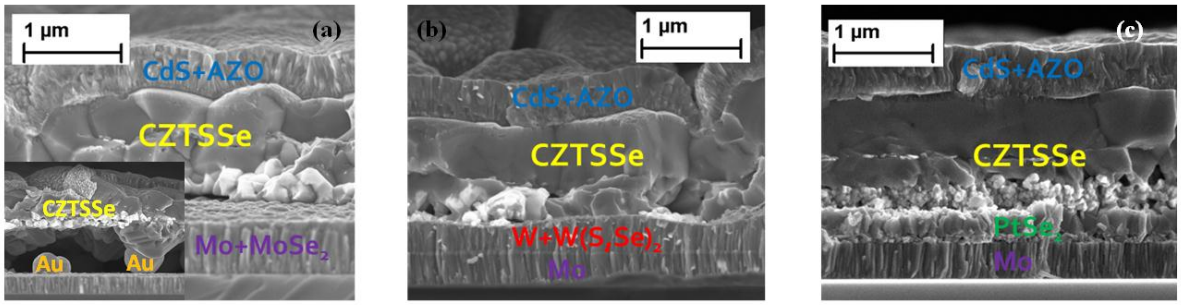

Figure 67: SEM images of Al:ZnO/i-ZnO/CdS/CZTSSe/BC/Mo solar cells synthesized on Au (CZTSSe|Au) (a), W (CZTSSe|W) (b), Pt (CZTSSe|Pt) (c). The inset in Fig. 64a shows the SEM image of gold particles after selenization process.

6.4 $Cu_2ZnSn(S,Se)_4$solar cells built with different back contacts

After these characterizations CZTSSe|Au, CZTSSe|W and CZTSSe|Pt are employed in full PV devices (Figure 68): at least eight 0.25 cm^2 solar cells have been fabricated and electrically characterized for each CZTSSe|BC combination and compared with CZTSSe solar cells built on a standard Mo BC.

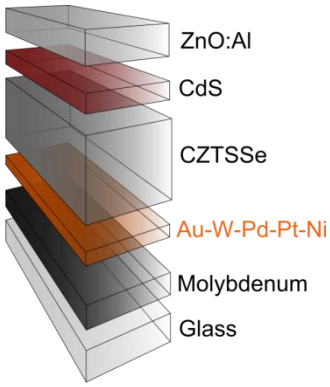

Figure 68: Schematic of Al:ZnO/i-ZnO/CdS/CZTSSe/BC/Mo solar cells.

On Figure 69 photovoltaic properties are depicted for all the cells. First, it is noticeable that solar cells built on Pt exhibit very low performances and will be excluded from the following discussion. These low performances could be the effect of a low crystallographic quality CZTSSe as demonstrated by Raman spectroscopy and because of the voids in the absorber as mentioned before.

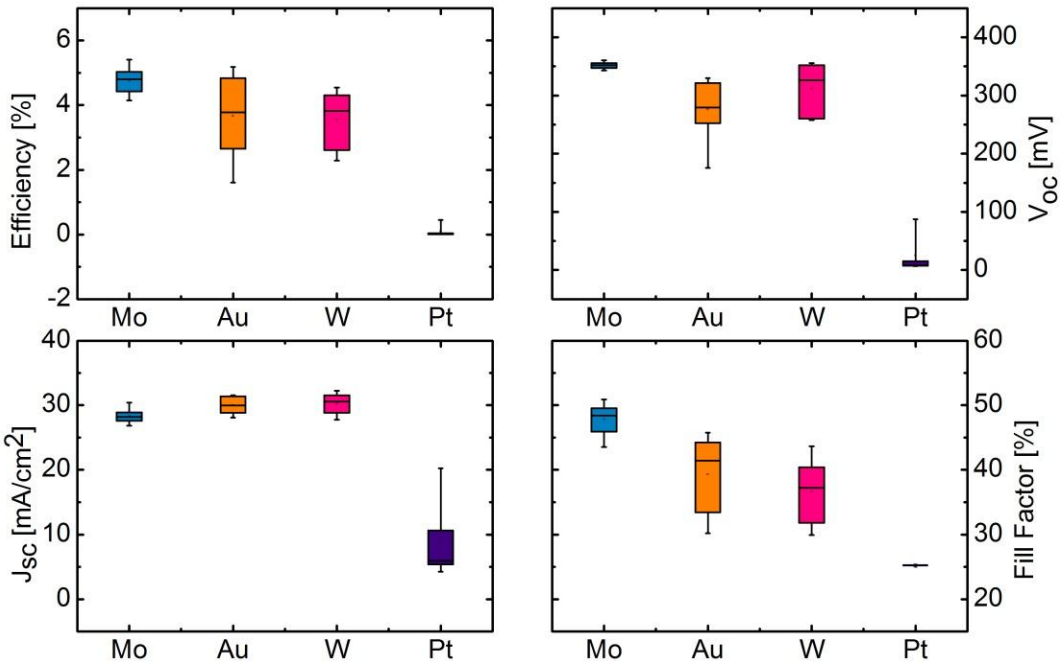

Figure 69: Current-voltage measurements under illumination (simulated AM1.5 spectrum, 100 mW/cm²) of Al:ZnO/i-ZnO/CdS/CZTSSe/BC/Mo solar cells.

The power conversion efficiency in the case of Mo is higher compared to the other BC (Au and W) and the dispersion of results is smaller. The variation of PCE between cells with different BC is clearly dominated by the variation of the fill factor. To check the possible implications of parasitic resistances in the FF, dark J-V measurement have been carried out (Figure 70). Figure 70 discloses series resistance, shunt resistance and dark saturation current extracted from dark J-V characteristics of CZTSSe|Mo-, CZTSSe|W- and CZTSSe|Au- based solar cells: in the case of W, the median R_s is four times higher than in the case of Mo probably due to the thick W/W(S,Se)$_2$ layer (see Fig. 67b). In the case of Au, the lower R_{sh} is responsible for the low FF.

The BC does not have a clear influence on J_0. Actually the J_0 median value seems to be slightly higher in the case of Mo, but the extraction of this parameter is subject of an important uncertainty because of the parasitic resistances and the high ideality factor. For this reason we assume that the small variation is irrelevant and caused by the fit method. It means that the BC might not affect the diode operation.

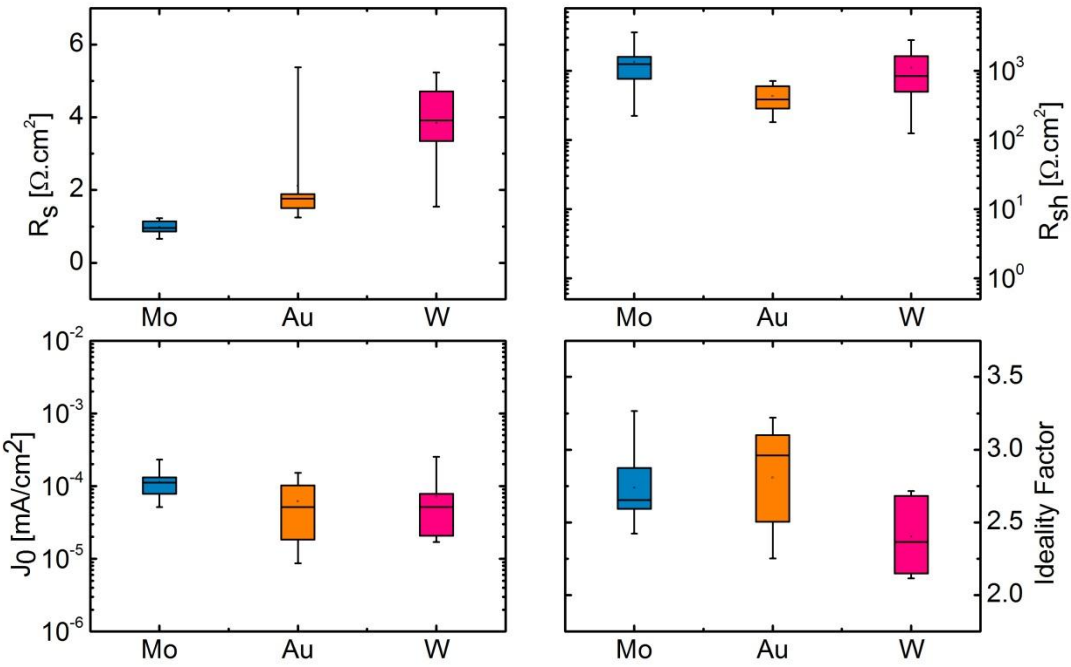

Figure 70: Dark current-voltage measurements of Al:ZnO/i-ZnO/CdS/CZTSSe/BC/Mo solar cells.

6.5 Current improvement

Beyond the analysis of PCE of different solar cells, it is remarkable that the median short-circuit current is higher for CZTSSe|W (30.2 mA/cm^2) and for CZTSSe|Au (31.5 mA/cm^2) than for CZTSSe|Mo (28.6 mA/cm^2).

In order to find out a reason for this current gain, two hypotheses are settled up. In the case of CZTSSe|Au a possible incorporation of Au into CZTSSe will lead to a decrease of the bandgap (due to Au_{Cu} replacement) which could explain the current gain: this hypothesis is verified by external quantum efficiency and cross-sectional EDS in TEM. COMSOL simulations are used for CZTSSe|Au solar cells in order to check on possible plasmonic effect in CZTSSe due to gold particles. In the case of CZTSSe|W capacitance-voltage (C-V) measurements are employed to estimate the doping profile: the idea is that a lower doping profile can increase the space charge region of the CZTSSe so increasing the collection efficiency.

6.5.1 Bandgap evaluation

To understand these differences, EQE measurements on the best performing CZTSSe solar cells with Mo–, Au– and W–BC have been carried out and shown on Fig. 71. The quantum

efficiency in the visible range is promising (~90%) for the three cells; the CZTSSe|Mo and CZTSSe|W curves have the same trend in the 380 nm – 1300 nm range although CZTSSe|W shows higher efficiency, whereas CZTSSe|Au EQE is lower between 750 nm and 1150 nm but it is still able to absorb photons in the 1150 nm – 1450 nm range. In the inset of Figure 71, the ratio of quantum efficiencies of cell built on W to cell built on Mo show the wavelength dependence of the current collection. The increase of this ratio at long wavelengths could mean a better collection of carriers generated deep in the absorber in the case of CZTSSe|W.

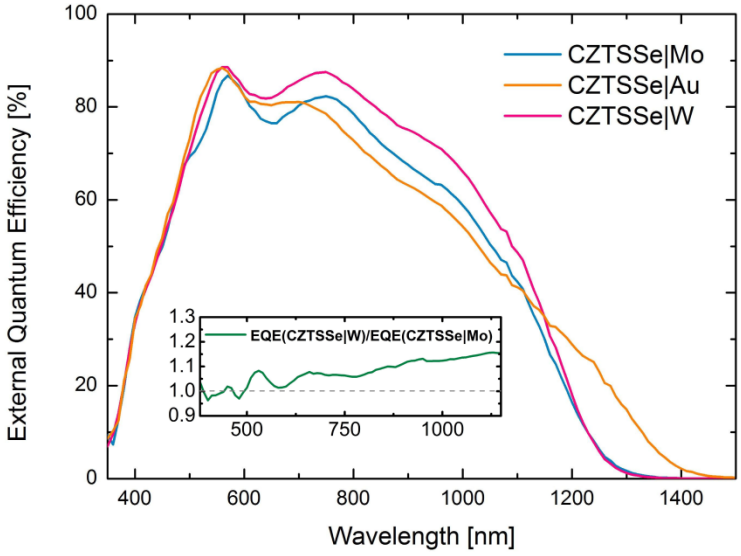

Figure 71: External quantum efficiency measurements on best performing CZTSSe solar cells with Mo-, Au-, W-back contacts. Bandgaps E_g are deduced via linear extrapolation of the low energy slope of the EQE. The inset shows EQE spectrum of CZTSSe|W solar cell divided by the EQE spectrum of CZTSSe|Mo solar cell.

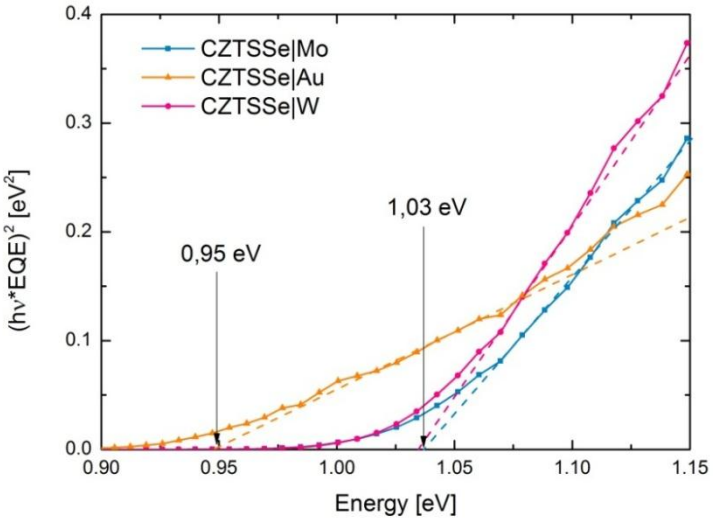

Figure 72: The bandgap energies extracted from the Tauc plot.

Concerning the gold BC, the more triangular shape of the EQE spectrum is the signature of current collection losses in the absorber. A major difference between CZTSSe|Au and the other cells is the current production in the 1150 nm – 1450 nm range. The evaluation of absorber bandgap from EQE curves plotted in Figure 72 gives 1.03 eV in the case of Mo and W and 0.95 eV in the case of Au.

6.5.2 Study of gold particles by TEM

A hypothesis to explain both the decrease of the bandgap and the current collection loss at long wavelengths may be the diffusion of gold partially replacing the copper in the CZTSSe layer close to the back contact. However, this hypothesis has not been clearly confirmed up to now, since no gold diffusion has been evidenced with the different characterization techniques used: GDS is not spatially resolved enough to determine such a diffusion, no shift in XRD spectra has been identified due to potential Au_{Cu} replacement, and no gold minor phases are found by Raman. For this reason incorporation of Au into CZTSSe is checked by performing a cross-sectional EDX analysis in a TEM. The results represented in Figure 73 show that Au has not diffused into the CZTSSe. This result allows us to put aside the hypothesis concerning the Au_{Cu} replacement to explain the lower bandgap and thus the latter as possible explanation for the current gain.

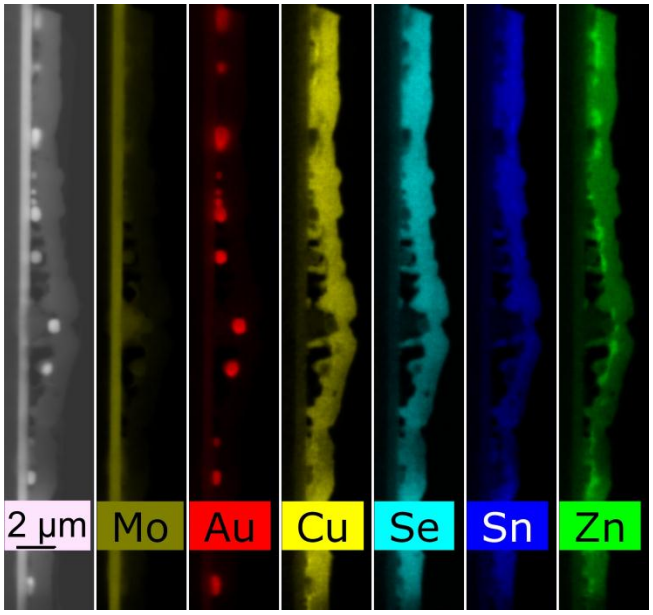

Figure 73: Cross-sectional EDS analysis of CZTSSe|Au performed in a TEM.

6.5.3 Plasmonic effect of gold particles

The fact that no gold incorporation into CZTSSe is so far discovered, paves the way to another possibility to explain the gain of current: a plasmonic effect due to gold particles in order to enhance light absorption in CZTSSe solar cells [17].

Plasmon light-trapping has already been used in other technologies like a-Si [18] and CIGS [19] in order to enhance the light absorption into the absorber layer by coupling and trapping freely propagating plane waves into the semiconductor thin film layer.

Figure 74: Schematic of COMSOL simulation

Simulations on COMSOL multiphysics [20] are performed in order to check on a possible plasmonic effect due to Au particles in CZTSSe. Figure 75 represents the normalized intensity (I/I_0 where I_0 is the intensity of the electromagnetic field used as excitation) in the CZTSSe layer in a cylinder centered around a half gold sphere of variable radius (Figure 74). The radius of the cylinder corresponds to the inter-particle distance based on the amount of gold deposited initially (62.5×10^6 μm^3).

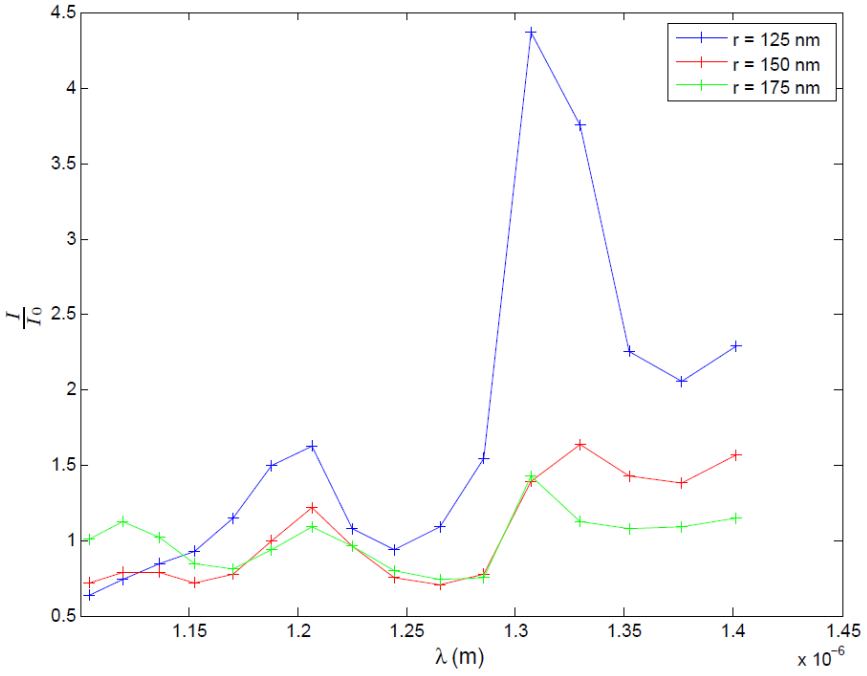

Figure 75: COMSOL simulations of electromagnetic field gain due to gold particles resonance with different radius.

Actually there are two moderate resonances of 50nm-width around 1200 and 1300 nm which are exactly in the range of interest (see EQE of CZTSSe|Au in Figure 71). This phenomenon is more important for small sphere of a 125 nm diameter but the latter is in contrast with SEM measurements which show an average particle radius of 200 nm (Figure 67). However the gain is not enough to corroborate the idea of a current gain due to plasmonic effect.

6.5.4 Capacitance-Voltage characteristics

C-V measurements for these three types of cells are performed in order to extract charge carrier density (*N*). The capacity of the p-n junction is considered as the one of a parallel plate capacitor (eq. 16) according to the approximation of Shockley [21].

$$C = \frac{\varepsilon \varepsilon_0 A}{w} \qquad \text{(eq. 16)}$$

Where *C* is the capacitance, *A* is the surface of the solar cell (0.25 cm^2), ε and ε_0 are the relative permittivity in the material and the vacuum permittivity, and *w* is the SCR width.
Considering no deep or interface defects nor additional parasitic resistances, and in the approximation of a p-n^+ junction it is possible to assume that the SCR, is located in the CZTSSe layer: the latter will certainly influence the estimation of the final *N*.
The capacitance then is computed as:

$$\frac{C}{\varepsilon_0 A} = \frac{1}{{w_a}/{\varepsilon_a} + {w_b}/{\varepsilon_b} + {w_c}/{\varepsilon_c}} \approx \frac{\varepsilon_a}{w_a} \qquad \text{(eq. 17)}$$

Where *w* is the SCR within the absorber (*a*), buffer (*b*), and TCO (*c*).
Moreover, considering the relationship relying the SCR to the potential (eq. 20), it is possible to extract the *N* as function of the SCR width [22]:

$$w = \sqrt{\frac{2\varepsilon\varepsilon_0}{qN}(V_D - V)} \qquad \text{(eq. 18)}$$

$$\frac{1}{C(V)^2} = \frac{q\varepsilon N(w)}{2(V+V_D)} \qquad \text{(eq. 19)}$$

or

$$N(w) = \frac{q\varepsilon C(V)^2}{2(V+V_D)} \qquad \text{(eq. 20)}$$

where V_D is the diffusion voltage and *N(w)* is the net charge carrier density at the edge of the SCR.

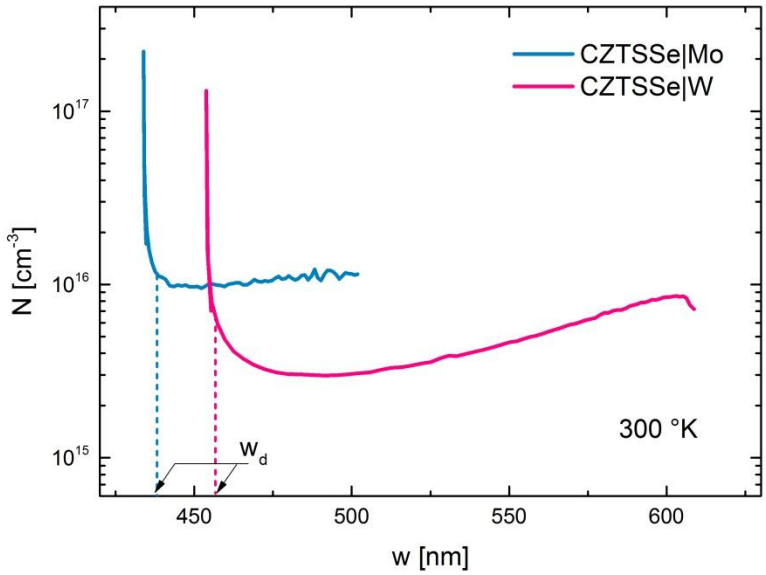

Figure 76: Net charge carrier profile extracted from C – V characteristics of CZTSSe|Mo and CZTSSe|W solar cells at 300 K. The C – V is performed using 100-mV, 100-kHz ac excitation with dc bias from 0.2 to – 3 V

C-V measurements indicate that there is a lower N in CZTSSe|W solar cell (~10^{15} cm^{-3}) compared to CZTSSe|Mo (~10^{16} cm^{-3}): as a consequence the SCR is wider which could induce a better charge collection and thus an improvement of the photo-generated current (J_{ph}) (Figure 76). The latter result is consistent with the EQE gain in the 750nm-1150nm range for CZTSSe|W solar cell (inset in Figure 71) and may explain the slightly higher V_{OC} in the case of Mo. Leakage current prevent us to extract carrier density in the case of CZTSSe|Au.

6.6 Conclusion

In conclusion, the replacement of Mo back contact in CZTSSe solar cells by other types of metals has been experimentally studied. Results show that, between the different metals used to replace Mo BC, only W and Au are eligible given that they provide a higher current compared to Mo. For tungsten this could be explained by a better charge collection in the near infrared part of the solar spectrum. In the case of gold it is not possible to give a unequivocal explanation to account for this effect. No evidences of a possible reaction between Au and chalcogens have been found although CZTSSe synthesized on this BC is irregular at their interface. However, Mo remains the best BC in terms of power conversion efficiency.

6.7 References

[1] I. Repins, M. A. Contreras, B. Egaas, C. DeHart, J. Scharf, C. L. Perkins, B. To, R. Noufi, Prog. Photovolt: Res. Appl. 16 (2008), pp.235–239
[2] N. Naghavi, Z. Jehl, F. Donsanti, J-F Guillemoles, I Gérard, M Bouttemy, A Etcheberry, J-L Pelouard, S Collin, C Colin, N Péré-Laperne, N Dahan, J-J Greffet, B Morel, Z. Djebbour, D. Lincot, Proc. SPIE, 8256 (2012), pp. 825617
[3] W. Wang, M. T. Winkler, O. Gunawan, T. Gokmen, T. K. Todorov, Y. Zhu, D. B. Mitzi, Adv. Mater., doi: 10.1002/aenm.201301465
[4] L. Grenet, S. Bernardi, D. Kohen, C. Lepoittevin, S. Noel, N. Karst, A. Brioude, S. Perraud, H. Mariette, Solar Energy Materials and Solar Cells 101 (2012), pp. 11-14.
[5] M. Patel, A.Ray, PhysicaB 407, 4391–4397 (2012)
[6] http://users.elis.ugent.be/ELISgroups/solar/projects/scaps.html
[7] J. J. Scragg, J. T. Wätjen, M. Edoff, T. Ericson, T. Kubart, and C. Platzer-Björkman, J. Am. Chem. Soc. 134, 19330−19333 (2013)
[8] P. Jackson, Barrierenworkshop, Stuttgart, Mars 2004.
[9] International Center for Diffraction Data: CZTSe – 10708930; Cu2SnSe4 – 10780600; Mo – 10714645; PtSe2 –107882281.
[10] I. Djerdj, A.M. Tonejc, A. Tonejc, N. Radić, Vacuum, 80, 1–3 (2005)
[11] P. K. Panigrahi and A. Pathak, Sci. Technol. Adv. Mater. 9, 045008 (2008)
[12] P.A. Fernandes, P.M.P. Salomé, A.F. da Cunha, Thin Solid Films, 517, 2519–2523 (2009)
[13] L. Sun, J. He, H. Kong, F. Yue, P. Yang, J. Chu, Solar Energy Materials and Solar Cells, 95, 2907–2913 (2011).
[14] M. Grossberg, J. Krustok, J. Raudoja, K. Timmo, M. Altosaar, and T. Raadik, Thin Solid Films, 519, 7403–7406 (2010).
[15] G. Altamura, L. Grenet, C. Bougerol, E. Robin, D. Kohen, H. Fournier, A. Brioude, S. Perraud, H. Mariette, Journal of Alloys and Compounds 588 (2014), pp. 310-315
[16] Z. Jehl Li-Kao, N. Naghavi, F. Erfurth, J. F. Guillemoles, I. Gérard, A. Etcheberry, J. L. Pelouard, S. Collin, G. Voorwinden, D. Lincot, Prog. Photovolt: Res. Appl. 20, 582–587 (2012)
[17] V. E. Ferry, L. A. Sweatlock, D. Pacifici, H. A. Atwater, Nano Letters 8 (2008), pp. 4391-4397
[18] H. Tan, R. Santbergen, A. H. M. Smets, M. Zeman, Nano Letters 12 (2012), pp. 4070-4076
[19] S. Park, R. Sharma, J. Sim, B. Baek, H. Ahn, J. Kim, C. Lee, Applied Surface Science, 280 (2013), pp. 757-763
[20] http://www.comsol.com/
[21] Sze, Physics of SEMICONDUCTOR DEVICES. JOHN WILEY & SONS, 3rd edition, 2007.
[22] S. Hegedus, W. Shafarman, Progress in Photovoltaics 12 (2004), pp. 2-3

Chapter 7

Influence of [S]/([S]+[Se]) ratio in $Cu_2ZnSn(S,Se)_4$ solar cells

Outline

7.1 Motivation

To obtain thin film solar cells with high power conversion efficiency, the band gap (E_g) engineering of the absorber layer is a possible solution. Clear correlations between E_g grading and device performances have already been demonstrated in CIGS solar cells by introducing Ga-gradients in the absorber [1]. In CZTSSe absorber layers, E_g can be tuned by changing the chalcogens ratio ([S]/([S]+[Se])) as reported in literature [2-4]. In particular Grossberg *& al.* [3] have found experimentally a linear dependence of E_g within $Cu_2ZnSn(S_{1-y}Se_y)_4$, with *y* values from 1 to 0, by optical measurements. Moreover, Chen *& al.* have also reported a near linear dependence of E_g on the chalcogens ratio with a small bowing parameter ($b = 0.1$) by using density functional theory [4].

Solar cell modeling is widely used to predict their PV performances. As CZTSSe polycrystalline thin film solar cells are complex in nature, numerical simulation of solar cells is a useful way to predict the effect of various parameters on the output performances. In this chapter we investigate the influence of the [S]/([S]+[Se]) ratio on CZTSSe-based solar cells PV properties.

7.2 Solar cell capacitance simulator (SCAPS)

The software SCAPS 3201 [5] is employed in this study and details of device structure and simulation are elaborated in the following sections. A particular attention is paid to the choice of the input parameters. SCAPS 3201 is a 1-D computer software to simulate the PV characteristics of thin film solar cells. Important information such as electric field distributions, free and trapped carrier populations, recombination profiles as a function of position can be also extracted from the SCAPS program.

7.3 $Cu_2ZnSn(S,Se)_4$ simulation parameters

In this chapter, the simulator is used to study CZTSSe based solar cells with the intention to propose new absorber design for high efficiency solar cells. A solar cell structure of Mo | CZTSSe | CdS | i-ZnO | ZnO:Al | Ni/Al grids was implemented for this study in the SCAPS 3201 environment. All the parameters of the different materials employed in the solar cell structure are listed and described hereafter.

7.3.1 Contacts

Ni/Al finger grids are chosen as front contact: they are of common use in thin film technology [6-7]. In the simulation model only Ni (metal work function 5.1 eV) is used since no metal stack is possible for the contact. Mo is used as back contact (metal work function 5.0 eV): as mentioned in chapter 7, it appears to be the most performing back contact tested so far in technology. As already demonstrated in CIGS and CZTS technology a $Mo(S,Se)_2$ phase at the interface between Mo and the absorber could be present depending on the deposition technique employed. Regarding these simulations no $Mo(S,Se)_2$ phase at the interface between Mo and CZTSSe layer is taken into account because of a lack of information regarding its mobility and thermal velocity. Electrical

properties of both contacts are exposed in Table 1.

Properties	Back contact	Front contact
Electron work function	5.0 eV (Mo)	5.1 eV (Ni)
SRV(*) of electron	10^7 cm/s	10^7 cm/s
SRV(*) of hole	10^7 cm/s	10^7 cm/s

Table 1: Electrical contact parameters used in the simulation; (*) SRV represents surface recombination velocity. These data are taken from CIGS solar cells in SCAPS database.

7.3.2 Solar cell parameters

The rest of the solar cell structure is composed by a i-ZnO | ZnO:Al stack as transparent conductive oxide (TCO), a n-doped CdS film as the buffer layer, and a p-doped CZTSSe film as the absorber layer.

Table 2 shows the material parameters used in the simulation: hereafter we discuss the semiconductor properties of each layer, with particular attention to the CZTSSe ones. It is important to highlight that the parameters in table 2 are taken or estimated from data published in the literature, but not necessarily from studies reporting the best devices performances.

Relative permittivity (ε_{CZTS} = 6.5 and ε_{CZTSe} = 8.6) are estimated from admittance spectroscopy measurements by Gunawan *& al.* [8]. CZTSSe is a self-compensated material in which the formation of acceptor-type lattice defects outnumbers donor-type defects. CZTS acceptor concentration ($N_{A,CZTS}$) is found to be 3×10^{18} cm^{-3} by photoconductivity measurements [9]; in the same reference a compensation ratio $k = N_{D,CZTS}/N_{A,CZTS} = 0.83$ is measured with $N_{D,CZTS}$ as the CZTS donor concentration. $N_{D,CZTS}$ is calculated from k and $N_{A,CZTS}$ and it is found to be 2.5×10^{18} cm^{-3}.

In CZTSSe material the donor and acceptor concentrations are mainly affected by the variation of Cu and Zn contents [10]: since there is only a variation in S and Se contents in the considered CZTSSe, we have attributed the same k (0.83) for pure CZTS and CZTSe. An acceptor concentration in CZTSe ($N_{A,CZTSe} = 1\times10^{17}$ cm^{-3}) is measured in Ref. 11, thus a $N_{D,CZTSe} = 8.0\times10^{16}$ cm^{-3} is then calculated.

With these parameters a net doping [17] is calculated for CZTS and CZTSe (eq. 21):

$$p = \left(\frac{N_A - N_D}{2N_D}\right) N_V exp\left[-\frac{E_A}{k_B T}\right] \qquad \text{(eq. 21)}$$

E_A is the activation energy of the Cu_{Zn} antisite defects for self p-type doping in kesterite CZTS and CZTSe (respectively 120 meV and 150 meV) [18]: $p_{CZTS} = 3.1\times10^{15}$ cm^{-3} and

p_{CZTSe} = 7.4×10^{14} cm^{-3} are finally computed. The latters are consistent with net doping evaluated by admittance spectroscopy for CZTS (10^{15}-10^{18} cm^{-3} range) [19-20] and CZTSe (10^{14}-10^{17} cm^{-3} range) [21-22] in the literature.

The CZTSSe is doped by introducing a single acceptor defect 120 meV above VB ($N_{A,CZTS}$ = 3.0×10^{18} cm^{-3}) in the CZTS and 150 meV above VB ($N_{A,CZTSe}$ = 1×10^{17} cm^{-3}) in the CZTSe, and a single donor defect 120 meV below CB ($N_{D,CZTS}$ = 2.5×10^{18} cm^{-3}) in the CZTS and 150 meV below CB ($N_{D,CZTSe}$ = 8.0×10^{16} cm^{-3}) in the CZTSe. In this way the software is able to consider the doping compensation in CZTSSe, as demonstrated by matching of the doping concentration between the calculated value and the quantity posted by SCAPS.

CZTS and CZTSe hole band mobility ($\mu_{h,CZTS} = \mu_{h,CZTSe}$)= 12.6 cm^2/V.s are taken from Ref. 12. CZTS and CZTSe electron band mobility ($\mu_{e,CZTS}$ = 44.7 cm^2/V.s and $\mu_{e,CZTSe}$ = 40 cm^2/V.s) are derived from hole mobility and ratio of effective masses [12]. The electron affinity for CZTS (χ_{CZTS} = 4.1 eV) is calculated by using conduction band (CB) alignment offset at CZTS|CdS interface from direct and inversion photoemission measurement by Bär *& al.* [13] and the value of χ_{CdS} = 4.4 eV extracted from Ref. 14. χ_{CZTSe} = 4.7 eV is calculated in the same way from Ref. 15.

Effective density of states in conduction and valence band are calculated using equations 22 and 23:

$$N_c = 2\left(\frac{2\pi m_e^* k_B T}{h^2}\right)^{\frac{3}{2}} \quad \text{(eq. 22)}$$

$$N_v = 2\left(\frac{2\pi m_h^* k_B T}{h^2}\right)^{\frac{3}{2}} \quad \text{(eq. 23)}$$

where m_e^* and m_h^* are the electron and hole effective mass extracted from first principle calculation reported by Persson [16], k_B is the Boltzmann's constant, T is the temperature in Kelvin, and h is the Planck's constant). Finally it is calculated $N_{c,CZTS}$ = 8.1×10^{16} cm^{-3} and $N_{v,CZTS}$ = 1.5×10^{19} cm^{-3} for CZTS and $N_{c,CZTSe}$ = 7.9×10^{17} cm^{-3} and $N_{v,CZTSe}$ = 4.5×10^{18} cm^{-3} for CZTSe.

To obtain the material parameter for a CZTSSe alloy with an arbitrary [S]/([S]+[Se]) ratio, value are linearly extrapolated from Table 2 (eq. 24).

$$Cu_2ZnSn(S_xSe_{1-x})_4 = xCZTS + (1-x)CZTSe \quad \text{(eq. 24)}$$

Semiconductor Property	**CZTSSe**		**CdS**	**i–ZnO**	**ZnO:Al**
	CZTS	**CZTSe**			
Layer thickness (nm)	1200		70	50	450
Relative permittivity, ε_r	6.5 [8]	8.6 [8]	5.7 [8]	9.0 [23]	9.0 [23]

Acceptor concentration, N_A ($1/cm^3$)	3.0×10^{18} [9]	1.0×10^{17} [11]	4.0×10^{3} (*) [27]	1.0×10^{1} [12]	1.0×10^{1} [17]
Donor concentration, N_D ($1/cm^3$)	2.5×10^{18} (*) [9]	8.0×10^{17} (*) [11]	1.1×10^{16} [28]	1.0×10^{16} [29]	1.0×10^{18} [17]
Electron band mobility, μ_e ($cm^2/V.s$)	44.7 (**)	40 [12]	50 [29]	100 [29]	100 [17]
Hole band mobility, μ_h ($cm^2/V.s$)	12.6 [12]	12.6 [12]	20 [29]	25 [29]	25 [17]
Electrical band gap (eV)	1.5 [26]	1.0 [25]	2.4 [9]	3.4 [29]	3.7 (***) [24]
Electron affinity, x_e (eV)	4.1 (*)	4.6 (*)	4.4 [14]	4.5 [29]	4.6 [9]
Effective density of states in conduction band (N_c) ($1/cm^3$)	8.1×10^{16} (*)	7.9×10^{17} (*)	2.0×10^{19} [29]	9.0×10^{18} [29]	2.2×10^{18} [17]
Effective density of states in valence band (N_v) ($1/cm^3$)	1.5×10^{19} (*)	4.5×10^{18} (*)	1.5×10^{18} [29]	4.0×10^{18} [29]	1.8×10^{19} [17]

Table 2: material parameters used in the simulation; the CZTSSe parameters correspond to a kesterite crystal structure. (*) calculated value, (**) estimated value. (***) The ZnO:Al band gap is found to broaden with increasing dopant concentration [23]. The parameter values with no asterisk are experimental ones taken from literature.

7.3.3 Defects in $Cu_2ZnSn(S,Se)_4$ absorber

Values for CZTSSe radiative recombination rate and Auger electron/hole capture coefficients of 5×10^{-9} cm^3/s and 10^{-29} cm^6/s respectively are used as reported in Ref. 30. In order to model non-radiative recombination (Shockley-Read-Hall) in CZTSSe layer, a Gaussian distribution of defects is introduced in the gap and centered in its midpoint. The trap density (N_{def}) is 5.0×10^{16} cm^{-3} in the case of CZTS and 1.9×10^{16} cm^{-3} in the case of CZTSe. Precise values of trap densities have been obtained by successive iteration in order, for the simulated cells with pure CZTS and CZTSe absorber layer, to approach the literature values of V_{oc} and J_{sc} of the best-performing CZTS [31] and CZTSe [32] solar cells. These values are found to be in the typical range in CIGS solar cells modeling from literature (10^{14} – 10^{18} cm^{-3}) [33-34]. The defect capture cross-section (σ) is derived from the equation 25:

$$\tau \cong \left(\sigma v_{th} N_{def}\right)^{-1} \qquad \text{(eq. 25)}$$

by considering a typical minority carrier lifetime (τ) as reported in literature (1-10 ns), and a thermal velocity of electrons (v_{th}) around 10^7 cm/s.

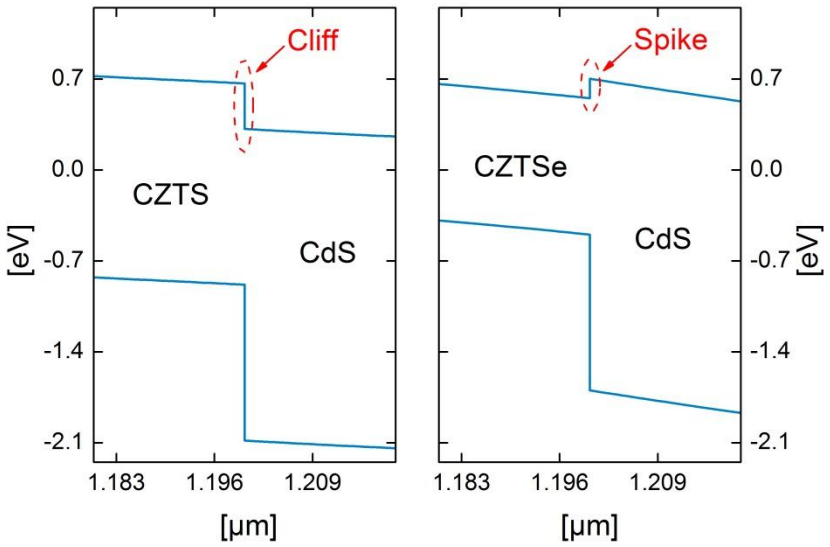

Figure 77: Cliff-like and spike-like alignment respectively at CZTS|CdS and CZTSe|CdS interface

Defect Property	CZTSSe		CdS	CZTSSe|CdS interface
	CZTS	CZTSe		
N_{def}	(D) 5×10^{17} cm^{-3}	(D) 1.9×10^{16} cm^{-3}	(A) 10^{18} cm^{-3}	(N) 10^{12} cm^{-2}
Position	Midgap	Midgap	midgap	midgap
W_G	0.1 eV	0.1 eV	0.1 eV	0.1 eV
σ_e	10^{-15} cm^2	10^{-15} cm^2	10^{-17} cm^2	10^{-18} cm^2
σ_h	10^{-15} cm^2	10^{-15} cm^2	10^{-12} cm^2	10^{-13} cm^2

Table 3: Summary of defect distribution parameters: donor-like defect (D), acceptor-like defect (A), neutral-like defect (N), defect characteristic energy width of a defect distribution (W_G).

Nowadays a lot of groups around the world are tackling the study of defects at the CZTSSe | CdS interface. It has been demonstrated that a CB "spike-like" alignment at the CZTSSe | CdS interface reduces the effects of interface defects on PV performances: this is due to the principle of charge carrier inversion at the interface as reported by Redinger *& al.* [37]. On the contrary a CB "cliff-like" alignment at the interface, although it is a typical II-type alignment which is ideal to promote charge separation at the interface thus decreasing recombination, is more harmful because of a lower defect activation energy (Figure 77).

Charged traps at the interface can adversely affect V_{oc} and remains an area for material improvement.
In our study defect distribution parameters for the CZTSSe | CdS interface are taken from literature on CIGS | CdS interface [36]. Defect distribution parameters for CZTSSe, CdS [35], and CZTSSe | CdS interface are summarized in Table 3.

7.4 $Cu_2ZnSn(S,Se)_4$ solar cells with different [S]/([S]+[Se]) ratio

The simulations are run at a fixed temperature of 300 K. The solar cell is illuminated with AM1.5G spectrum (1 kW/m^2) on the TCO face, and the composition of the absorber layer is varied to find the influence of [S]/([S]+[Se]) gradient on the solar cell characteristics.
Before starting with simulations of chalcogens gradients, the PV characteristics of our modeled CZTS and CZTSe are compared with the best-performing real counterpart published respectively in Ref. 31 and 32. These results are shown in Table 4:

Simulations	PV Properties			
	V_{oc} [Volt]	J_{sc} [mA/cm^2]	FF [%]	PCE [%]
CZTS	0.72 *(0.70)*	21.3 *(21.6)*	62.9 *(60.0)*	10.3 *(9.2)*
CZTSe	0.41 *(0.41)*	39.0 *(38.9)*	73.2 *(61.4)*	10.4 *(9.7)*

Table 4: PV performances comparison of modeled CZTS and CZTSe solar cells with best performing real CZTS [31] and CZTSe [32] (values in brackets).

Very good matching of J-V characteristics (in particular concerning V_{oc} and J_{sc}: at least 97% matching in both cases) have been obtained. The higher PCE, in the case of modeled devices, is mainly influenced by the higher FF: the latter could be explained by smaller series resistance (R_s) in the simulated device. The reason for smaller R_s might be: (i) the absence of $Mo(Se,S)_2$ between the absorber and the back contact in our simulation, (ii) the difference between material parameters used to model TCO, and the experimental ones. A comparison between extracted R_s from simulation (< 0.7 Ω.cm^2), and reported R_s (1.05 Ω.cm^2) [32] for pure CZTSe, confirms our first assessment. The same comparison for pure CZTS is not possible due to the lack of reported experimental values [31].

7.4.1 Linear variation of the chalcogens gradient

The composition of the kesterite CZTSSe layer is linearly varied between pure CZTS and pure CZTSe. The composition of the absorber varies along the thickness with the chalcogens ratio [S]/([S]+[Se] according to equation 26:

$$y(x) = \frac{x}{L}(t - s) + s \qquad \text{(eq. 26)}$$

where *L* denotes the thickness of the CZTSSe layer, *x* the distance from the back contact, *t* the chalcogens ratio at the Mo|CZTSSe interface, *s* the chalcogens ratio at the CZTSSe|CdS interface. Figure 78 shows all the possible linear variations of the absorber (yellow area) which are studied in the present paragraph.

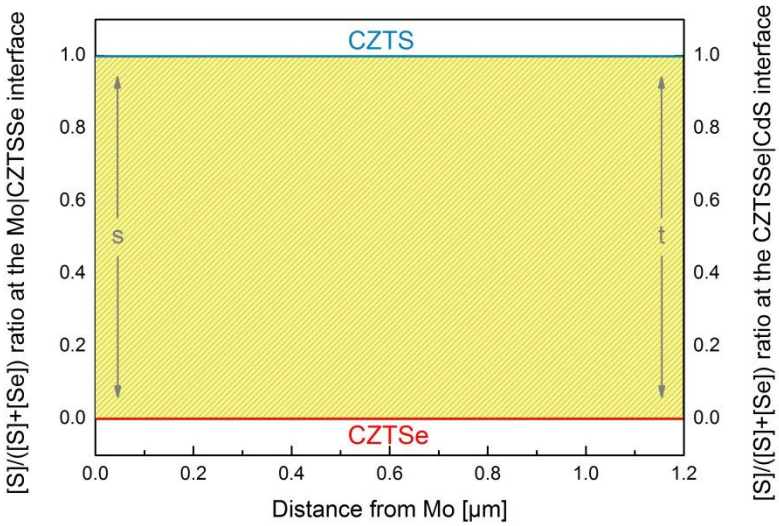

Figure 78: Composition graph of CZTSSe absorber layer. The CZTSSe absorber thickness (L) is 1.2 µm.

The PV characteristics, as a result of simulations, are reported in the colormaps of Figure 79. A higher PCE is achieved for compositions that are more S-rich towards the back contact and more Se-rich towards the CdS interface (Figure 79a). This means also that a good choice of the bandgap, decreasing from the BC to the CdS interface ($s > t$), will improve the PV characteristics of CZTSSe solar cells. The latter entail a conduction band decreasing from the Mo towards the CdS (purple line in Figure 80). It can be noticed that the band diagram shown in Figure 80 fits well with the results published by Persson [38]: in the change from CZTS to CZTSe due to Se incorporation, there is a shift towards lower energies of the CB, which leads to the decrease of E_g. The valence band is not affected by the chalcogens ratio variation, at least far from the metal contacts.
The best efficiency of 16.5% is achieved (current-voltage curve in Fig. 81) with a CZTSSe bandgap of 1.2 eV ([S]/([S]+[Se]) = 0.4) at the back contact and 1.1 eV ([S]/([S]+[Se]) = 0.2) at the absorber | buffer interface (inset Fig. 79). This latter PCE result is higher than the best performing CZTSSe solar cell (12.6% PCE) published by IBM [2] where no chalcogens gradient is present and a constant [S]/([S]+[Se]) ~ 0.25 is present. With the same constant chalcogens ratio in our simulations, an overall efficiency of 13.1% is achieved.

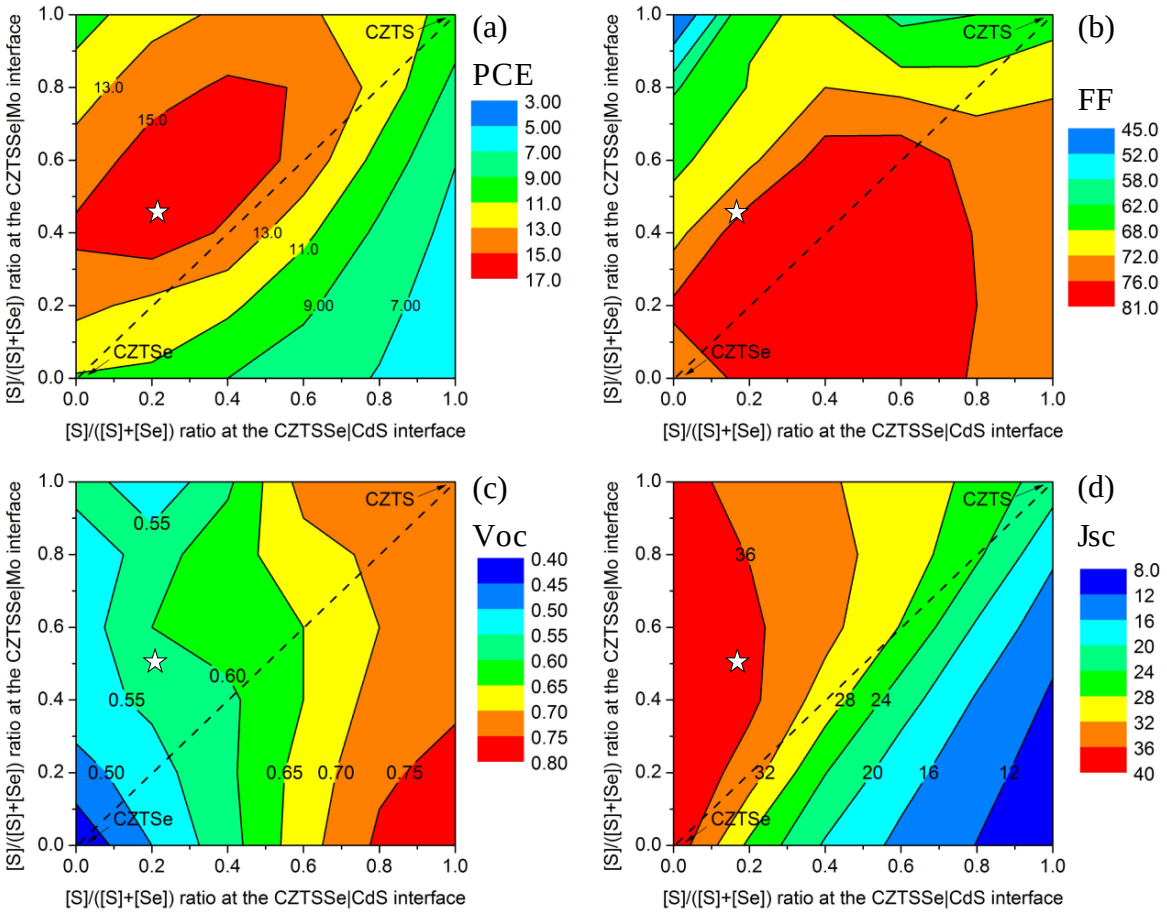

Figure 79: PV characteristics variation of Mo | CZTSSe | CdS | i-ZnO | ZnO:Al solar cell where the CZTSSe absorber has a linear variation of the [S]/([S]+[Se]) ratio as function of depth. PCE/% (a), FF/% (b), V_{oc}/Volt (c), J_{sc}/(mA/cm^2) (d), the white star indicates the best performing solar cell.

FF variations do not follow PCE trend: high FF is found in the vicinity of a bandgap with no gradient (range 1 – 1.3 eV) and whenever the S-content increases from the BC towards the CZTSSe|CdS interface. Since no $Mo(S,Se)_2$ is modeled at the interface with the BC, and no change of the TCO properties are provided within each simulation, a reason to explain the variations of the FF could be a better contact interface between the Mo and the absorber with low S-content close to BC (Figure 79b). In general, at the back surface of the CZTSSe a contact barrier may be established due to Fermi level pinning or a particular band alignment between the Mo and CZTSSe. It has been demonstrated by Scheer and Schock [37] that a barrier height for holes less than 0.3 eV is not harmful for FF and thus PCE. In our simulations the barrier height at the Mo interface is always higher than 0.3 eV, but it increases when the S-content increase within the BC (Figure 80): the latter may explain the FF loss encountered in our simulations.

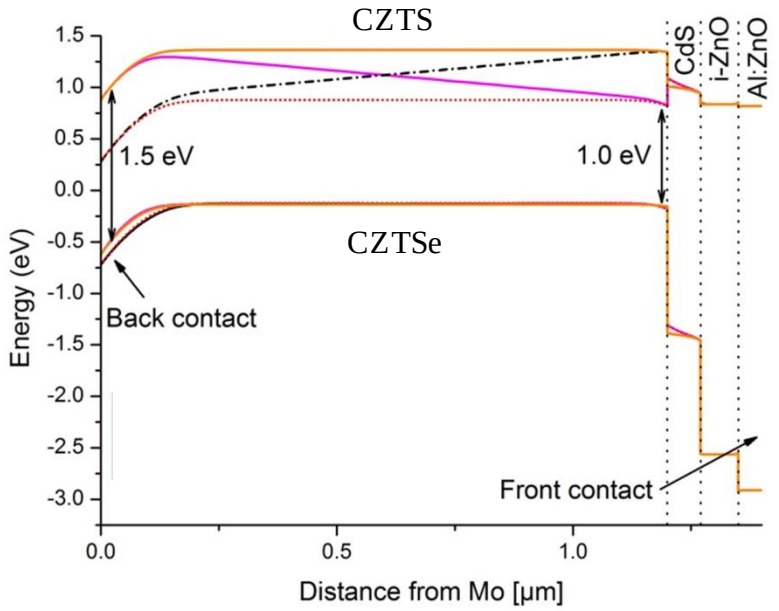

Figure 80: Graphical representation of the band alignments within different CZTSSe solar cells in the dark: CZTS (orange line), CZTSe (red dotted line), bandgap decreasing from Mo to CdS (purple line), bandgap decreasing from CdS to Mo (black line).

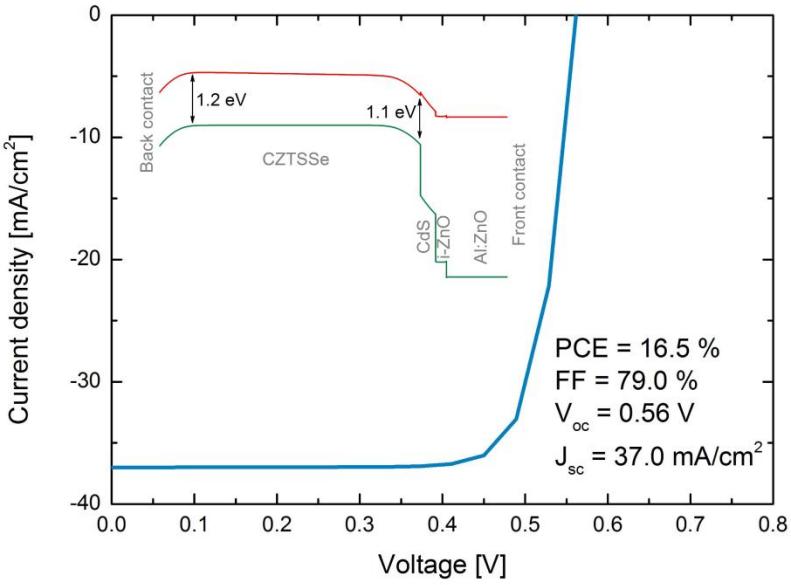

Figure 81: J-V characteristics of the best-performing Mo | CZTSSe | CdS | i-ZnO | ZnO:Al solar cell. CZTSSe absorber has a linear variation of the [S]/([S]+[Se]) ratio as function of depth (inset).

V_{oc} variations are dominated by the composition variation at the interface with the buffer layer and are not related to chalcogens variation towards the BC (Figure 79c). In particular, V_{oc} increases with the widening of the bandgap at the CZTSSe|CdS interface.
Of more interest is the V_{oc} loss as a function of the bandgap grading (Figure 82). V_{oc} loss is defined as:

$$V_{oc,loss} = \frac{E_g}{q} - V_{oc} = \frac{kT}{q} ln\left(\frac{J_{00}}{J_{ph}}\right) \quad \text{(eq. 27)}$$

where J_{ph} is the photogenerated current and J_{oo} is the reference current density. To evaluate V_{oc} losses in linearly graded absorbers, the value of E_g is taken at the interface with CdS. Colormap in Figure 79 shows that V_{oc} loss is more important along with the increase of E_g at the buffer interface. This loss could be due mainly to a low J_{ph} since a high J_{00} (values increasing as a function of the bandgap from 10^{13} A/cm^2 for pure CZTSe to 10^{21} A/cm^2 for pure CZTS) is extracted from dark J(V) simulations using equation 28:

$$J_0 = J_{00} e^{-\left[\frac{E_T}{kT}\right]} \quad \text{(eq. 28)}$$

where E_T is considered as the $E_{g,CZTSSe}$ at the CZTSSe|CdS interface.

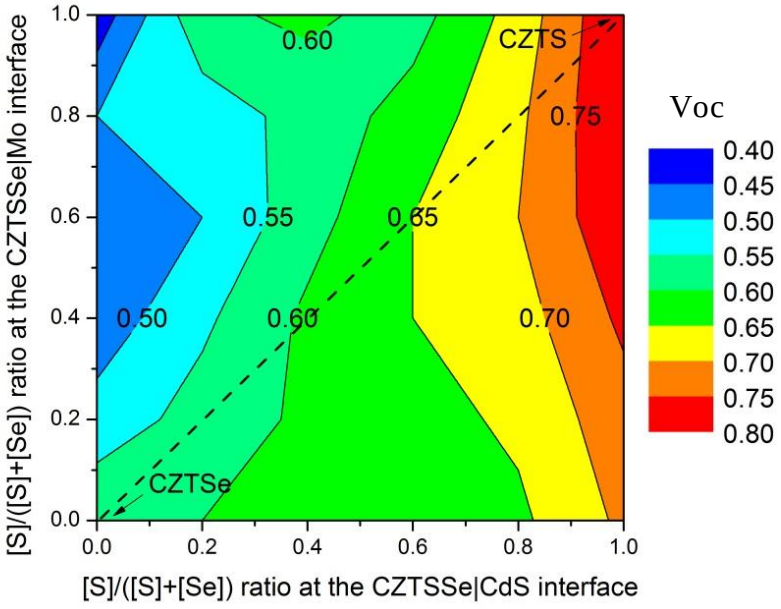

Figure 82: Voc losses variation (in Volt) of Mo | CZTSSe | CdS | i-ZnO | ZnO:Al solar cell where the CZTSSe absorber has a linear variation of the [S]/([S]+[Se]) ratio as function of depth.

J_{sc} variations (Figure 79d) depend mostly on the variation of the bandgap at the absorber|buffer interface. Three parameters are taken into account to try to explain the difference in the simulated J_{sc}: (i) E_g, (ii) the electric field ($\vec{E}$) created by the CB slope in

the absorber ("negative" when the E_g increases towards the CdS interface, and "positive" when the E_g decreases towards the CdS interface), (iii) the band alignment at CZTSSe|CdS interface (spike-like or cliff-like alignment) [37]. A low E_g allows increasing the photogenerated current. A positive CB slope in CZTSSe assists electron collection due to the production of a favorable $\vec{E}$ which drives electron towards the buffer layer, whereas a negative slope produces an unfavorable $\vec{E}$ thus limiting the collection of photogenerated carriers. The red part of the map in Figure 79d is characterized by having small E_g at the CZTSSe|CdS interface, a positive slope which drifts apart the minority carriers towards CdS rising up the J_{ph}, and a spike-like alignment at the buffer interface which promote charge inversion thus decreasing recombination at the interface. On the contrary low values of J_{sc} are encountered when E_g is high at the interface with CdS, or negative CB slope is present.

7.5 Conclusions

In summary it has been demonstrated by numerical simulations that a good choice of the absorber composition can boost PV performances in Mo | CZTSSe | CdS | i-ZnO | ZnO:Al | Ni/Al solar cells without changing the absorber material quality. In particular, linear [S]/([S]+[Se]) ratio gradients along the depth of the absorber have an impact on solar cell efficiency. Among all the different absorber studied, solar cells having a CZTSSe layer with a linear grading compositions from [S]/([S]+[Se]) = 0.4 (E_g = 1.2 eV) at the back contact to [S]/([S]+[Se]) = 0.2 (Eg = 1.1 eV) at the interface with CdS has been found to be the best performing one (PCE = 16.5%, FF = 79.0%, V_{oc} = 0.56 V, J_{sc} = 37.0 mA/cm^2). The latter results should allow achieving, experimentally, CZTSSe solar cell with good PV performances without change the absorber quality. This is possible since the variation of the chalcogens is almost ineffective on the CZTSSe lattice parameters thus not playing an important role in the formation of defects in the material.

7.6 References

[1] T. Dullweber, G. Hanna, W. Shams-Kolahi, A. Schwartzlander, M.A. Contreras, R. Noufi, H.W. Schock, Thin Solid Films 361–362 (2000), pp. 478–481

[2] H. Wei, Z. Ye, M. Li, Y. Su, Z. Yang, Y. Zhang, Cryst. Eng. Commun. 13 (2011), p. 2222

[3] M. Grossberg, J. Krustok, J. Raudoja, K. Timmo, M. Altosaar, T. Raadik, Thin Solid Films, 519 (2011), p. 7403

[4] S. Chen, A. Walsh, J. Yang, X.G. Gong, L. Sun, P.X. Yang, J.H. Chu, S.H. Wei, Phys. Rev. B, 83 (2011), p. 125201

[5] http://users.elis.ugent.be/ELISgroups/solar/projects/scaps.html

[6] I. Repins, M. A. Contreras, B. Egaas, C. DeHart, J. Scharf, C. L. Perkins, B. To, R. Noufi, Progress in Photovoltaics: Research and Applications, 16 (2008), pp. 235–239

[7] K. Wang, O. Gunawan, T. Todorov, B. Shin, S. J. Chey, N. A. Bojarczuk, D. Mitzi, S. Guha, Applied Physics Letters , 97 (2010), pp.143508 - 143508-3

[8] O. Gunawan, T. Gokmen, C. W. Warren, J. D. Cohen, T. K. Todorov, D. A. R. Barkhouse, S. Bag, J. Tang, B. Shin, D. B. Mitzi, Appl. Phys. Lett. 100, 253905 (2012)

[9] J. C. Gonzalez, G. M. Ribeiro, E. R. Viana, P. A. Fernandes, P. M. P. Salome, K. Gutierrez, A. Abelenda, F. M. Matinaga, J. P. Leitao, A. F. da Cunha, J. Phys. D: Appl. Phys. 46 (2013) 155107
[10] H. Wei, Z. Ye, M. Li, Y. Su, Z. Yang, Y. Zhang, Cryst. Eng. Commun. 13 (2011), p. 2222
[11] A. Nagaoka, K. Yoshinoa, H. Taniguchi, T. Taniyama, H. Miyake, Journal of Crystal Growth, 354 (2012), pp. 147–151
[12] I. L. Repins, H. Moutinho, S. G. Choi, A. Kanevce, D. Kuciauskas, P. Dippo, C. L. Beall, J. Carapella, C. DeHart, B. Huang, S. H. Wei, J. Appl. Phys. 114, 084507 (2013)
[13] M. Bär, B. A. Schubert, B. Marsen, R.G. Wilks, S. Pookpanratana, M. Blum, S. Krause, T. Unold, W. Yang, L. Weinhardt, C. Heske, H.-W. Schock, Appl. Phys. Lett., 99 (2011), p. 222105
[14] J. J. Scragg, P. J. Dale, L. M. Peter, 10 (2008), pp. 639–642
[15] R. Haight, A. Barkhouse, O. Gunawan, B. Shin, M. Copel, M. Hopstaken, D. B. Mitzi, Appl. Phys. Lett. 98, 253502 (2011)
[16] C. Persson, J. Appl. Phys. 107, 053710 (2010)
[17] X. Zi-qiang, L. Yan, C.Hang, Materials Science in Semiconductor Processing, 9 (2006), pp. 132–135
[18] S. Chen, L. Wang, A. Walsh, X. G. Gong, S. Wei, Appl. Phys. Lett. 101, 223901 (2012)
[19] J. J. Scragg, P. J. Dale, L. M. Peter, 10 (2008), pp. 639–642
[20] G. Brammertz, Y. Ren, M. Buffière S. Mertens, J. Hendrickx, H. Marko, A. E. Zaghi N. Lenaers, C. Köble, J. Vleugels, M. Meuris, J. Poortmans, 535 (2013), pp. 348–352
[21] G. Brammertz, M. Buffière, Y. Mevel, Y. Ren, A. E. Zaghi, N. Lenaers, Y. Mols, C. Koeble, J. Vleugels, M. Meuris, J. Poortmans, Appl. Phys. Lett. 102, 013902 (2013)
[22] P.S. Battacharya, Semiconductor Optoelectronic Devices, 2nd ed., Prentice- Hall, 1996.
[23] A. Nagaoka, H. Miyake, T. Taniyama, K. Kakimoto, K. Yoshino, Appl. Phys. Lett. 103, 112107 (2013
[24] P. Chelvanathan, M. I. Hossain, N. Amin, Current Applied Physics 10 (2010) S387–S391
[25] S. Ahn, S. Jung, J. Gwak, A. Cho, K. Shin, K. Yoon, D. Park, H. Cheong, J. H. Yun, Appl. Phys. Lett. 97 (2010), p. 021905
[26] H. Katagiri, K. Saitoh, T. Washio, H. Shinohara, T. Kurumadani, S. Miyajima, Solar Energy Materials and Solar Cells, 65 (2001), p. 141
[27] J. L. Boone, G. Cantwell, M. D. Shaw, J. Appl. Phys. 58, 2296 (1985)
[28] G. A. Sullivan, Phys. Rev. 184, 796–805 (1969)
[29] A. Niemegeers, M. Burgelman, R. Herberholz, U. Rau, D. Hariskos, H. W. Schock, Prog. Photovolt. Res. Appl. 6, 407-421 (1998)
[30] M. Patel, A. Ray, Physica B 407 (2012), pp. 4391–4397
[31] T. Kato, H. Hiroi, N. Sakai, S. Muraoka, and H. Sugimoto, 27th European Photovoltaic Solar Energy Conference and Exhibition, Frankfurt (2012)
[32] G. Brammertz, M. Buffière, S. Oueslati, H. ElAnzeery, K. Ben Messaoud, S. Sahayaraj, C. Köble, M. Meuris, J. Poortmans, Appl. Phys. Lett. 103, 163904 (2013)
[33] T. Eisenbarth, T. Unold, R. Caballero, C.A. Kaufmann, D. Abou-Ras, H.-W. Schock, Thin Solid Films 517 (2009) 2244–2247

[34] A. Jasenek, U. Rau, Journal of Applied Physics 90, 650 (2001)
[35] M. Gloeckler, A.L. Fahrenbruch, and J.R. Sites, 3rd World Conference on Photovoltaic Energy Conversion May 11-18.2003 Osaka. Japan.
[36] R. Scheer, Thin Solid Films 519 (2011) 7472–7475
[37] A. Redinger, M. Mousel, M. H. Wolter, N. Valle, S. Siebentritt, Thin Solid Films, 535 (2013), pp. 291-295
[38] C. Persson, J. Appl. Phys. 107, 053710 (2010)
[39] R. Scheer, H. W. Schock, Chalcogenide Photovoltaics, Wiley-VCH, ISBN: 978-3-527-31459-1

Chapter 8

Conclusions & recommendations for further studies

Outline

8.1 Works carried out

The main objective of this PhD thesis was directed toward establishing and explaining the relationships between synthesis conditions of CZTSSe, its physical properties and performance of photovoltaic devices. To tackle this task, the first step is to understand the formation mechanism of the material in relation to the growth conditions. CZTSSe is synthesized by a two-step selenization process, where a first step of precursor deposition by PVD is followed by a second step of annealing. Different precursor stacking orders are studied in order to understand the sequence of reactions that, starting from their deposition, leads to the final CZTSSe layer. This study has required a strong effort on the material characterization at each step of the synthesis. The result demonstrates that in the case of our two-step process, the final material obtained after a selenization annealing at high temperature (570°C) for a long time (30 min) is independent of the precursor stacking order, but that the intermediate steps during the selenization process are strongly influenced by the position of the copper and tin layers in the precursor stack, .

The possible benefits resulting from incorporation of sodium in CZTSSe are also studied. This work is carried out by synthesizing CZTSSe on different sodium-containing substrates: in this way sodium migrates from the substrates to the absorber. After quantification of Na in CZTSSe right after growth, the latter is characterized to evaluate its quality and employed in a full solar cell to check on its photovoltaic properties. Results demonstrate that, as for CIGS technology, sodium is beneficial for CZTSSe allowing increasing the open circuit voltage and efficiency.

Molybdenum is the most used back contact in CZTSSe based solar cells. However, it has been suggested recently that Mo is not stable at the interface with CZTSSe. In addition, to the best of our knowledge, no experimental study has been carried out so far to test whether solar cells built on another back contact could exhibit better photovoltaic properties. For this purpose, various metals (Au, W, Pd, Pt, and Ni) are deposited on top of Mo, and it is demonstrated that it is possible to synthesize device-quality CZTSSe thin films on W, Au, and Pt back contacts. It is shown that that W and Au back contacts allow enhancing the photogenerated current, but that Mo remains the best back contact in terms of power conversion efficiency.

The effects of [S]/([S]+[Se]) ratio tuning on CZTSSe based solar cell performances are studied by solar cell capacitance simulator (SCAPS) to find out the optimum absorber composition. The simulations lead to an efficiency of 16.5% (with open-circuit voltage of 0.56 V, short-circuit current of 37.0 mA/cm^2 and fill factor of 79.0%) when the sulfur content is linearly decreased from the back contact towards the buffer layer. Based on these results, we propose that bandgap engineering based on the control of [S]/([S]+[Se]) ratio in the absorber is a powerful tool which allows increasing the performances of CZTSSe based solar cells without changing the absorber material quality.

8.2 Perspectives

CZTSSe is a complex material. Researchers all over the world have identified several high impact research topics that could accelerate the development of CZTSSe technology in order to take it to the level of other thin film technologies like CIGS and CdTe. To do so, high quality films require a higher degree of understanding and control of the CZTSSe

phase diagram, correlation of device characteristics with processing conditions, and existence of secondary phases.

Since CZTSSe technology is directly derived from chalcopyrites, a deep study of the front and back contacts and interfaces is required to address some of the most urgent solar cell development needs. In this context, a precise control on the chalcogen space distribution in the absorber is mandatory if we want to tackle the problem of band alignment with the other materials composing the solar cell.

Another major issue that needs to be treated is the formation and impact of bulk, interface, and grain boundaries defects. The latter will contribute to decrease the present V_{oc} deficit in the best CZTSSe devices which is at the base of the low efficiency. In this context a deeper study on the Na, or any other element, that could help passivating defects should be addressed.

In the end, a major point needed to be studied is the possibility to really implement bandgap gradient in kesterite solar cells. Simulations demonstrated that this approach should increase CZTSSe solar cell efficiency without playing on the material quality. The combination of this technique coupled with a better understanding of the defect formation will lead to a drastic improvement of the kesterite technology.